

Radio Frequency Probes for Ultra-High Field Magnetic Resonance Imaging

by Daniel Lee, MSci

Thesis submitted to the University of Nottingham for the degree of
Doctor of Philosophy, May 2011

Contents

1	Introduction	4
1.1	An Introduction to Current Magnetic Resonance Imaging	4
1.2	Chapter Summaries	5
2	Theory	7
2.1	Theory of Magnetic Resonance Imaging	7
2.1.1	Quantum Mechanics	7
2.1.2	Generating the Magnetic Resonance Imaging Signal	9
2.1.3	Relaxation of the Magnetic Resonance Imaging Signal	13
2.2	Pulses	16
2.2.1	Excitation Pulses	16
2.2.2	Inversion Pulses	17
2.2.3	Refocusing Pulses	19
2.3	Pulse Sequences	23
2.3.1	Gradient Echo Pulse Sequences	23
2.3.2	Inversion Recovery Pulse Sequences	24
2.3.3	Radio Frequency Spin Echo Sequences	25
2.3.4	Echo Planar Imaging	28

2.3.5	Sa2RAGE	33
2.4	Image Acquisition	35
2.4.1	k-Space and k-Space Trajectories	35
2.4.2	Frequency-Encoding	38
2.4.3	Phase-Encoding	39
2.4.4	Readout Bandwidth and Frequency Bandwidth	42
2.4.5	Noise	43
2.5	Specific Absorption Rate	44
2.6	Sensitivity Encoding	46
2.7	Transmit Sensitivity Encoding	48
2.8	Computational Electromagnetics	52
2.8.1	Finite Difference Time Domain	52
2.8.2	Transmission Line Modeling	53
2.8.3	Method of Moments	55
2.9	Radio Frequency Circuit Theory	59
2.9.1	Quality Factor	59
2.9.2	Smith Charts	59
2.9.3	Matching	62
2.9.4	Coupling	66
2.9.5	Decoupling Theory	68
2.9.6	Decoupling by Overlapping Elements and Using Low-Impedance Preamplifiers	74
2.10	Travelling-wave Magnetic Resonance Imaging	78
2.11	Reciprocity	81

3	Literature Survey	85
3.1	Radio Frequency Shimming	85
3.2	Transmit Sensitivity Encoding	86
3.3	Coupling and Decoupling	90
3.4	Travelling-wave Magnetic Resonance Imaging	91
4	Methods	93
4.1	Magnetic Resonance Imaging Hardware	93
4.2	Imaging with Experimental Coils	96
4.3	Transmit Sensitivity Encoding Coil Construction	98
4.3.1	Single Element Coils	98
4.3.2	Mock-Coil	99
4.3.3	Decoupling	101
4.3.4	The First Dome Coil	104
4.3.5	The Second Dome Coil	106
4.3.6	Coil Stand	107
4.4	Travelling Wave Antennas	112
4.4.1	The Patch Antenna	112
4.4.2	The End-Fire Helix Antenna	112
4.5	Simulations	118
4.6	Calibrating Coils	121
4.6.1	Power	121
4.6.2	Specific Absorption Rates to Magnetic Field Con- version Factors	123
4.6.3	Other Parameters	124

5	Transmit Sensitivity Encoding Results	125
5.1	Pulse Design	125
5.2	Coil Calibration	132
5.3	Results of Specific Absorption Rate Simulations	134
5.4	Imaging	137
6	Travelling Wave Results	142
6.1	Simulation of Travelling Wave Behaviour	142
6.2	Specific Absorption Rate	144
6.3	Simulated Patch Antenna and End-Fire Helix Comparison	149
6.3.1	Simulated Specific Absorption Rate	149
6.3.2	Signal-to-Noise Ratio	149
6.4	Heating Test	155
6.5	Patch Antenna Calibration	156
6.6	Imaging	158
7	Conclusions	161
7.1	Future Work	165
A	MATLAB Code	168

Abstract

This thesis describes the design, construction and testing of a dome coil. The dome coil is hemispherical in shape and is intended to be used within a set of hemispherical gradient coils in a seven tesla magnetic resonance imaging magnet. The dome coil has eight independent elements and is designed to be used for parallel transmission and reception. It is shown that the dome coil produces less specific absorption rate than a conventional birdcage coil and is suitable for head imaging.

A study of travelling wave magnetic resonance imaging is also presented. In this study two different methods of generating a travelling wave (using a patch antenna and an end-fire helix antenna) are compared, and the power requirements and specific absorption rate of the travelling wave approach are considered. It is concluded that travelling wave magnetic resonance imaging is best performed using a local receive coil and with the travelling wave antenna placed at least 50 cm from the subject.

All theory relevant to the design, construction, testing and use of these coils and antennas is also presented.

Acknowledgments

I would like to take this opportunity to acknowledge the support of my parents, Tim and Claire, and of my girlfriend, Nancy, which was very important in getting me into a position where I could begin my postgraduate study. I would like to thank my supervisor, Dr Paul Glover, for all his help and guidance throughout my postgraduate study. The assistance of Ian Thexton, Jeff Smith and Alan Dorkes when building my various coils and antennas was valued greatly. I would also like to thank all my friends at the Sir Peter Mansfield Magnetic Resonance Centre for making it such a wonderful place to work in.

Collaboration with Arthur Magill and his colleagues at the Centre d'Imagerie BioMedicale in Lausanne, Switzerland allowed the dome coil to be tested on a multi-transmit system, and so I would also like to thank them for their help and hard work during my visit.

This work was funded by the medical research council and I was funded by the Sir Peter Mansfield fund.

Abbreviations and Conventions

Abbreviations

AD - analogue to digital

CAD - computer-aided design

CEM - computational electromagnetics

DFT - discrete Fourier transform

EM - electromagnetic

EPI - echo-planar imaging

FDTD - finite-difference time domain

FFE - fast field echo

FID - free-induction decay

FLAIR - fluid attenuated inversion recovery

FOV - field of view

FoX - field of excitation

FT - Fourier transform

GRE - gradient echo

GR-EPI - gradient echo echo-planar imaging

IR - inversion recovery

IR-Prep - inversion recovery preparation

LHS - left-hand side

MP - magnetisation preparation

MR - magnetic resonance

MRI - magnetic resonance imaging

PA - projection acquisition

PO - power optimization

RARE - relaxation enhancement

RF - radio-frequency

RHS - right-hand side

SAR - specific absorption rate

SE - spin echo

SE-EPI - spin echo echo-planar imaging

SENSE - sensitivity encoding

SNR - signal-to-noise ratio

SPECIAL - spectral inversion of lipids

SPMMRC - Sir Peter Mansfield magnetic resonance centre

STIR - short tau inversion recovery

TE - echo time

TI - inversion time

TLM - transmission line modeling

TR - repetition time

TW - travelling wave

Conventions

- $j = \sqrt{-1}$
- i represents an oscillating current
- \mathbf{i} and \mathbf{j} are unit vectors in k-space.

Chapter 1

Introduction

1.1 An Introduction to Current Magnetic Resonance Imaging

Since its development as a medical imaging modality by Sir Peter Mansfield in 1977 [1], MRI has been progressing to higher and higher field strengths as researchers try to achieve better signal-to-noise. The current medical standard is three tesla or lower, while the current highest field for research purposes is seven tesla, with even stronger field strength scanners being planned. With each new field strength come new challenges and problems. In particular at seven tesla the wavelength of the RF signal being used becomes comparable to the size of the human body. This causes B_1 inhomogeneities which create dark regions in the images where very little to no signal is obtained. This has prevented seven tesla imaging from being used for larger regions of the body, particularly the torso; most imaging at seven tesla is restricted

to the head.

The most common method of overcoming B_1 inhomogeneities is to use transmit SENSE, first proposed by Katscher et al. in 2003 [2]. In transmit SENSE multiple transmitters are used so that the B_1 's generated by each element combine to cancel out any B_1 inhomogeneities.

A recent alternative to transmit SENSE is travelling wave (TW) MRI, first proposed by Brunner et al. in 2009 [3]. In this approach to MRI, the transmit coil is replaced by a transmit antenna. This transmits a circularly polarised wave down the bore which then produces, theoretically, an excitation pattern without any B_1 inhomogeneities. TW MRI also has the potential benefit of freeing up space in the bore.

1.2 Chapter Summaries

Chapter one contains an introduction to the current state of magnetic resonance imaging (MRI).

Chapter two provides all the theory relevant to this research. It includes an overview of MRI, pulse sequences and image acquisition. The mathematics of sensitivity encoding (SENSE) is given and transmit SENSE is also introduced. The different methods of simulating electromagnetic (EM) systems are covered as well as radio-frequency (RF) circuit theory. Finally, travelling wave MRI and reciprocity are considered.

Chapter three is a literature survey covering the key publications on SENSE and transmit SENSE, coupling, decoupling and travelling wave MRI.

Chapter four describes the different elements of a MRI scanner. It then details how the various coils and antennas used in this research were constructed. The simulations used in this research are then illustrated and the chapter then ends with information on how the coils and antennas were calibrated.

Chapter five presents the results obtained from using a dome head coil for parallel transmission. Transmit SENSE pulses are given, as well as the images that they produced. Images obtained by the dome coil are shown. Final calibration and specific absorption rate (SAR) values are also quoted.

Chapter six contains the results from investigations into travelling wave MRI. A comparison between a patch antenna and an end-fire helix antenna is given. Images obtained by the patch antenna are shown. Final calibration and SAR values for the patch antenna are also quoted.

Chapter seven provides conclusions for this research, and an appendix includes the MATLAB code used for pulse design in chapter five.

Chapter 2

Theory

2.1 Theory of Magnetic Resonance Imaging

2.1.1 Quantum Mechanics

In quantum mechanics, angular momentum is quantised. An electron orbiting a proton (see Figure 2.1) possesses a set of stable rotational states with total angular momentum L_{tot} ,

$$L_{tot} = [J(J + 1)]^{\frac{1}{2}} \hbar, \quad (2.1)$$

where $\hbar \cong 1.054 \times 10^{-34} Js$, is Planck's constant divided by 2π , and J is a quantum number. Equation 2.1 implies the quantisation of total angular momentum.

Rotational energy is proportional to the square of the total angular momentum and is therefore also quantised. The stable energies of a

two-body system are

$$E_J = BJ(J + 1) \tag{2.2}$$

where B is the rotational constant of the system. B is small for a heavy system and large for a light system.

J provides no information about the axis of rotation. In order to specify the axis a second quantum number, M_J , must be used. M_J can be one of $2J + 1$ integer values, ranging from $-J, -J + 1, \dots + J$. M_J is sometimes referred to as the azimuthal quantum number. If no external field is applied, all M_J values associated with a particular J value are degenerate (i.e. have the same energy). Applying an external magnetic field causes the M_J values to have different energy values. This is called the Zeeman effect. The spread of energies is called the Zeeman splitting.

Spin is also a form of angular momentum, but it is not produced by rotation of the system. Spin is an intrinsic property of the particle itself. The total angular momentum of particles with spin takes values of the form $[S(S + 1)]^{\frac{1}{2}} \hbar$. Each S level consists of $2S + 1$ degenerate energy levels. These energy levels cease to be degenerate in a magnetic field. Every elementary particle has an intrinsic spin quantum number S . Some particles have integer S -values (e.g. 0, 1, 2 ...) and are called bosons. Other particles have half-integer S -values (e.g. $\frac{1}{2}, \frac{3}{2}, \frac{5}{2}$...) and are called fermions.

The angular momentum of a particle is a vector and may point in any direction in space. For a sample of spins in equilibrium in the absence of a magnetic field, the distribution of magnetic moments is

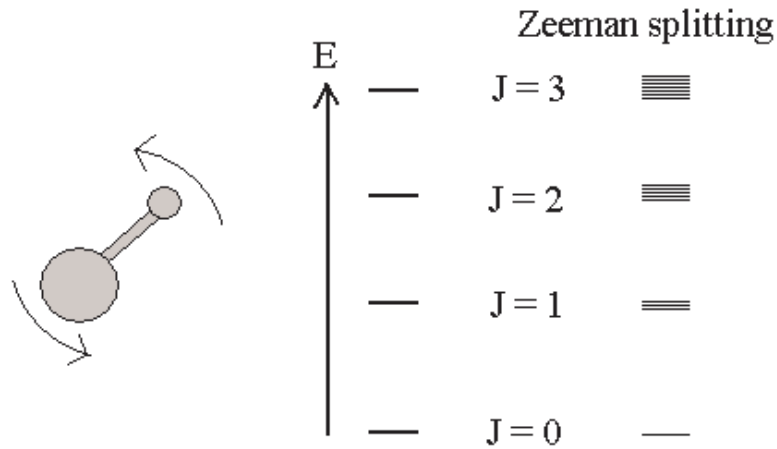


Figure 2.1: The energies of a rotating two-body system, and the Zeeman splitting of those energy levels in a magnetic field.

completely isotropic. If a magnetic field is suddenly applied the spin polarisation moves around the field. The magnetic moment moves on a cone, keeping a constant angle between the spin magnetic moment and the field, as shown in Figure 2.2. This is called precession. Spins precess because they possess angular momentum as well as a magnetic moment. These two moments combine to create the conical path of the spin polarization.

2.1.2 Generating the Magnetic Resonance Imaging Signal

The physical process which makes MRI possible is the interaction of nuclear spins with electromagnetic (EM) radiation. This interaction alters the spin state of the nuclear spins, and when the spins relax back to their original state they emit EM radiation which can be detected

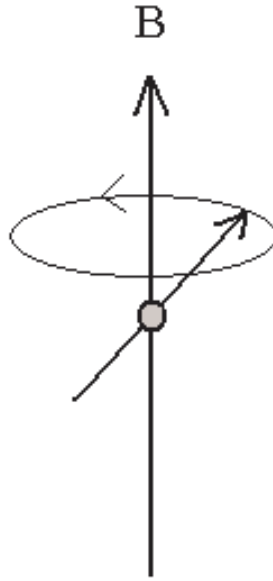


Figure 2.2: A spin in a magnetic field will precess about the field.

and used to create a magnetic resonance (MR) image. This process can be examined by considering the applied EM radiation as an oscillating time-dependent B-field and substituting it into the classical equation of motion,

$$\frac{d\boldsymbol{\mu}}{dt} = \gamma \boldsymbol{\mu} \times \mathbf{B}. \quad (2.3)$$

μ is the magnetic moment of a nucleus, t is time, γ is the gyromagnetic ratio and \mathbf{B} is the magnetic field. The magnetic moment of a nucleus is a measure of a nucleus' ability to interact with a magnetic field. It is a combination of the effects of circulation of electric currents, the magnetic moments of the electrons and the magnetic moments of the atomic nuclei. The atomic nuclei contribution is typically many orders of magnitude smaller than the other two. The magnetic moments of electrons and nuclei are inherent properties of the particles, and are

related to the spin of the particles by

$$\mu = \gamma S. \quad (2.4)$$

The gyromagnetic ratio is positive when the magnetic moment is parallel to the angular momentum of the particle, and negative when the magnetic moment is opposite to the angular momentum.

Now consider the application of a RF EM wave, $\mathbf{B}_1(t)$, to a single nuclear spin in the presence of a static field \mathbf{B} , usually defined as

$$\mathbf{B} = \mathbf{k}B_z. \quad (2.5)$$

The oscillating B-field, $\mathbf{B}_1(t)$, that is usually applied perpendicular to \mathbf{B} , is the most important part of the RF radiation.

$$\mathbf{B}_1(t) = \mathbf{i}2B_1 \cos \omega t \quad (2.6)$$

$\mathbf{B}_1(t)$ can be resolved into two components, one rotating anticlockwise about the z-axis and the other rotating clockwise, as $\mathbf{B}_1(t)$ is linearly polarised along the x-axis.

$$\mathbf{B}_a(t) = B_1(\mathbf{i} \cos \omega t + \mathbf{j} \sin \omega t) \quad (2.7)$$

$$\mathbf{B}_c(t) = B_1(\mathbf{i} \cos \omega t - \mathbf{j} \sin \omega t) \quad (2.8)$$

ω is the angular frequency of rotation, and \mathbf{i} , \mathbf{j} and \mathbf{k} are orthogonal unit vectors. The equation of motion has now become

$$\frac{d\boldsymbol{\mu}}{dt} = \gamma \boldsymbol{\mu} \times (\mathbf{B} + \mathbf{B}_1(t)) = \gamma \boldsymbol{\mu} \times (\mathbf{k}B_z + B_1(\mathbf{i} \cos \omega t - \mathbf{j} \sin \omega t)). \quad (2.9)$$

The anticlockwise component of the magnetic field can be ignored since it has the opposite polarisation to the spin precession and so the two

will not interact significantly compared to the clockwise component. It is now convenient to begin considering the system in the rotating reference frame, that is the frame which rotates about the z-axis at frequency $-\omega$. In this frame \mathbf{B}_1 is stationary,

$$\mathbf{B}_1(t) = B_1 \mathbf{i}', \quad (2.10)$$

where \mathbf{i}' is a new unit vector. This has the effect of removing the time dependence of \mathbf{B}_1 from the equations of motion. Now designate the new axes of this rotating reference frame as (x', y', z) , giving a new magnetic moment vector of

$$\underline{\mu} = \mu_{x'} \mathbf{i}' + \mu_{y'} \mathbf{j}' + \mu_z \mathbf{k}. \quad (2.11)$$

From classical mechanics it is known that if the time derivative of a vector \mathbf{r} in the non-rotating frame is given by $\left(\frac{d\mathbf{r}}{dt}\right)_{x,y,z}$, then the time derivative in the rotating frame is given by the following transformation;

$$\left(\frac{d\mathbf{r}}{dt}\right)_{x,y,z} = \underline{\omega} \times \mathbf{r} + \left(\frac{d\mathbf{r}}{dt}\right)_{x',y',z}, \quad (2.12)$$

where $\underline{\omega} = -\omega \mathbf{k}$ is the angular velocity. If this transformation is applied to the equation of motion the following is obtained:

$$\underline{\omega} \times \underline{\mu} + \left(\frac{d\underline{\mu}}{dt}\right)_{x',y',z} = \gamma \underline{\mu} \times (B_z \mathbf{k} + B_1 \mathbf{i}'). \quad (2.13)$$

This can be rearranged and written in terms of an effective magnetic field \mathbf{B}_{eff} as follows:

$$\left(\frac{d\underline{\mu}}{dt}\right)_{x',y',z} = \underline{\mu} \times \gamma \mathbf{B}_{\text{eff}} \quad (2.14)$$

where

$$\mathbf{B}_{\text{eff}} = B_1 \mathbf{i}' + \left(B_z - \frac{\omega}{\gamma}\right) \mathbf{k}. \quad (2.15)$$

The result of this equation is that the magnetic moment precesses about the axis of \mathbf{B}_{eff} . This induces an oscillating current in the receiver coil which is called a free-induction decay (FID).

Now consider the special case where $\omega = \omega_L$, where ω_L is the Larmor frequency of our spin system, then $B_z = \frac{\omega}{\gamma}$ and therefore $\mathbf{B}_{\text{eff}} = B_1 \mathbf{i}'$. In this case $\underline{\mu}$ precesses about the x' axis and the application of \mathbf{B}_1 has the effect of rotating $\underline{\mu}$ about the x' -axis at angular frequency $\omega = -\gamma B_1$. After a time t_w , the magnetic moment vector will have rotated through an angle $\theta = \gamma B_1 t_w$.

The above mathematics demonstrates how an MR signal is excited. A RF pulse of frequency ω_L is applied for a duration of t_w , polarised in a plane perpendicular to the applied static magnetic field. This has the effect of tipping the magnetic moment vector through an angle θ . This is equivalent to flipping the spin from the up state to the down state, which causes absorption and stimulated emission. It is this stimulated emission which is detected as an MR signal.

2.1.3 Relaxation of the Magnetic Resonance Imaging Signal

The Bloch equations describe the time evolution of a spin-1/2 ensemble. They take into account the effects of relaxation, RF fields and the resonance offset on the spins. The Bloch equations are a set of coupled

differential equations,

$$\frac{d}{dt} \begin{pmatrix} M_x \\ M_y \\ M_z \end{pmatrix} = \begin{pmatrix} 0 & \Omega_0 & \omega_{\text{nut}} \sin \phi \\ \Omega_0 & 0 & -\omega_{\text{nut}} \cos \phi \\ -\omega_{\text{nut}} \sin \phi & \omega_{\text{nut}} \cos \phi & 0 \end{pmatrix} \begin{pmatrix} M_x \\ M_y \\ M_z \end{pmatrix} - \begin{pmatrix} \frac{M_x}{T_2} \\ \frac{M_y}{T_2} \\ \frac{M_z - M_0}{T_1} \end{pmatrix}, \quad (2.16)$$

where Ω_0 is the resonance offset, $\omega_{\text{nut}} = |\gamma B_1|$ is the nutation frequency of the pulse and ϕ is the phase of the RF field. T_1 is the spin-lattice or longitudinal relaxation time constant, which is dependent on the nucleus and its environment, such as viscosity and temperature. T_2 is the transverse relaxation constant and accounts for the homogeneous decay of the precessing macroscopic nuclear magnetisation.

If the resonance offset Ω_0 and the relaxation constants T_1^{-1} and T_2^{-1} are all set to zero the Bloch equations describe stimulated absorption and emission. If the nutation frequency ω_{nut} is set to zero the Bloch equations describe free evolution of the spin with relaxation.

The steady state values of the components of the magnetisation can be found by solving the Bloch equations. If the phase ϕ and resonance offset Ω_0 are both equal to zero, then the time-derivatives become

$$\frac{d}{dt} M_y = -T_2^{-1} M_y - \omega_{\text{nut}} M_z \quad (2.17)$$

and

$$\frac{d}{dt} M_z = \omega_{\text{nut}} M_y - T_1^{-1} (M_z - M_0). \quad (2.18)$$

In the steady-state the time-derivatives vanish and the resulting equa-

tion can be solved for the transverse magnetisation

$$M_y \text{ (steady state)} = \frac{-T_2 \omega_{\text{nut}} M_0}{1 + T_1 T_2 \omega_{\text{nut}}^2}. \quad (2.19)$$

2.2 Pulses

2.2.1 Excitation Pulses

An excitation pulse tips the magnetisation vector away from the direction of \mathbf{B}_0 , allowing an MR signal to be detected. Every MR pulse sequence uses at least one excitation pulse.

An excitation pulse is achieved by pulsing the RF field modulation envelope ($\mathbf{B}_1(t)$) for a short time, typically between 200 μs and 5 ms. This is short enough so that T_1 and T_2 relaxation can usually be ignored for proton MRI.

Excitation pulses are characterised by their flip angle, θ . θ is the angle between the magnetisation vector and the direction of the main magnetic field immediately after the excitation pulse finishes. The flip angle for on-resonance spins can be found using the area under the RF envelope:

$$\theta(t) = \gamma \int_{t'=0}^t B_1(t') dt'. \quad (2.20)$$

For example, in spin echo pulse sequences $\theta = 90^\circ$ is typically used, while in gradient echo pulses flip angles between 5° and 70° are common.

Slice-selective excitation pulses can be used with slice-selective gradients to produce excited sections or slices of magnetisation. Alternatively a hard pulse (a short duration, rectangular pulse) can be used. Hard pulses typically excite all the spins that are coupled to the RF coil.

Excitation pulses can produce a flip angle that varies across a selected slice. The resulting distribution of transverse magnetisation,

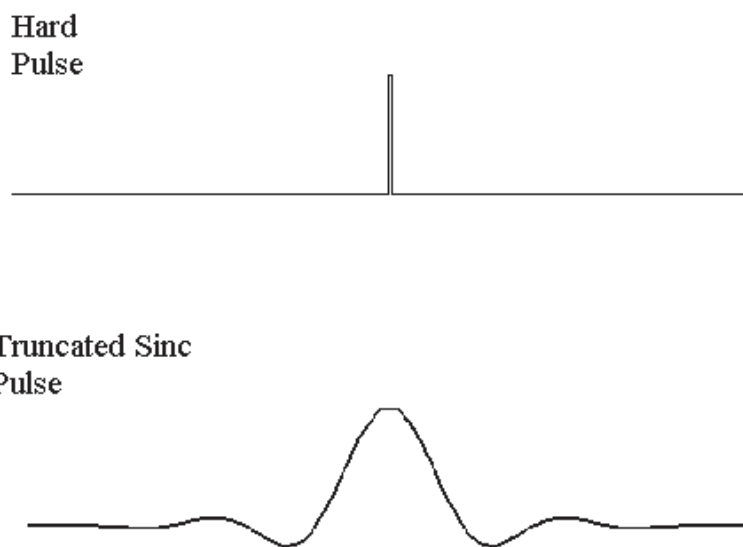


Figure 2.3: Excitation pulses can be hard pulses, but truncated sinc pulses produce very uniform slice profiles.

when plotted against either position or frequency, is called the slice profile.

For small flip angles, the slice profile is approximated by the FT of the RF pulse. An ideal slice profile consists of a uniform flip angle within the desired slice and a flip angle of $\theta = 0^\circ$ outside. Truncated sinc pulses (as shown in Figure 2.3) make very good excitation pulses as the FT of an infinitely long sinc pulse is a perfect rectangular pulse. A truncated sinc pulse therefore produces a very uniform slice profile.

2.2.2 Inversion Pulses

An inversion pulse nutates the magnetisation vector from the main magnetic field direction \mathbf{B}_0 to the negative \mathbf{B}_0 direction. Although an ideal inversion pulse rotates the magnetisation vector through 180° ,

sometimes the angle is not quite 180° , either by design or due to system imperfections (see Figure 2.4). Such pulses still serve as inversion pulses, provided that they still result in a magnetisation vector with a negative z component.

Inversion pulses can be categorised by pulse shape, spatial selectivity, spectral selectivity, and adiabaticity. These are not mutually exclusive, for example a sinc-shaped inversion pulse can be used for spatial or spectral selection. The selectivity of an inversion pulse is determined by both its pulse shape and the pulse width. Inversion pulses with constant RF amplitude (i.e. rectangular or hard pulses) are usually non-selective, while amplitude modulated pulses are usually frequency selective. Using a frequency selective inversion pulse concurrently with a slice-selection gradient results in a spatially selective pulse. Using a frequency selective inversion pulse without a slice-selection gradient allows the pulse to be spectrally selective.

Inversion pulses are similar to refocusing pulses in that they both have nominal flip angle of 180° , however inversion pulses assume that the magnetisation is initially along the $+z$ direction, whereas refocusing pulses do not. Refocusing pulses are typically accompanied by a crusher gradient pair, whereas an inversion pulse is usually followed by a spoiler gradient to dephase any residual transverse magnetisation.

Inversion and excitation pulses share the same initial condition, but an excitation pulse results in significant transverse magnetisation and an inversion pulse does not. A non-selective inversion pulse can be obtained by increasing the flip angle of a non-selective excitation pulse

to 180° , but this is usually not possible with selective pulses.

It is possible to use an inversion pulse to negate the signal from a tissue with a specific T_1 . This is achieved by applying an inversion pulse a time $T_1 \ln 2$ before an excitation pulse, and is used in short tau inversion recovery (STIR, [4] [5]) and spectral inversion at lipids (SPECIAL, [6]) to suppress lipid signals. This is also used to eliminate hyperintense signals from cerebrospinal fluid in fluid attenuated inversion recovery (FLAIR, [7] [8]). Another use of inversion pulses is to alter the T_1 contrast in an image, which is sometimes called inversion recovery preparation (IR-Prep) or magnetisation preparation (MP) [9]. Inversion pulses are also widely used to measure the T_1 relaxation times of tissues and in perfusion imaging.

2.2.3 Refocusing Pulses

The transverse magnetisation excited by an RF pulse will usually consist of contributions from many spin isochromats. Applied imaging gradients, field inhomogeneities, magnetic susceptibility variation and chemical shifts can all affect the precession frequencies of these isochromats differently. This produces isochromats with a range of precession frequencies distributed about the average Larmor frequency. This is known as phase dispersion. A refocusing pulse rotates the dispersing spin isochromats about an axis in the transverse plane. This leads to the magnetisation vectors refocusing at a later time. This refocused magnetisation is known as an RF spin echo, or simply a spin echo.

The optimal flip angle for a refocusing pulse is 180° , as it produces

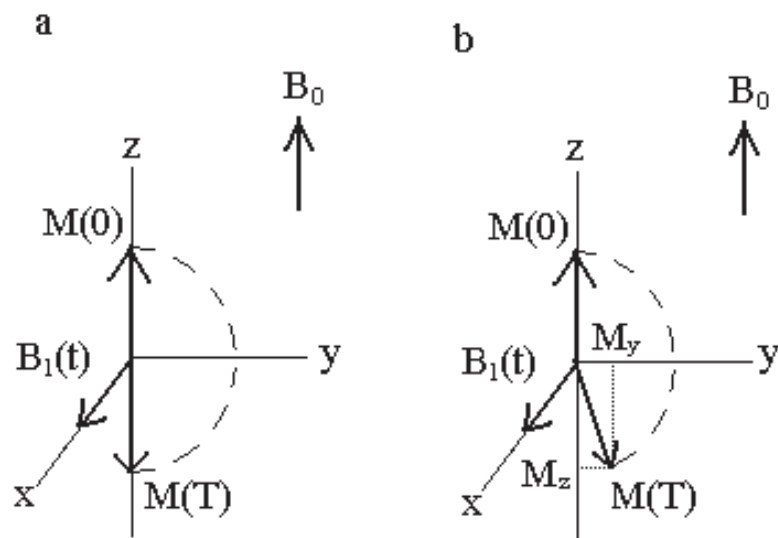


Figure 2.4: a) initially the magnetisation $M(0)$ is aligned with $B(0)$. An RF inversion pulse $B_1(t)$ is applied along the x axis which rotates the magnetisation vector in the yz plane about the x axis. At the end of the pulse (time T) the magnetisation $M(T)$ is along the negative z axis. b) when the flip angle is not 180° the inversion is incomplete and a transverse magnetisation M_y is produced.

the largest spin echo signal. Refocusing pulses can have a flip angle that is not equal to 180° , but the refocusing is only partial for such pulses.

Many types of pulse can be used for refocusing, such as rectangular, SINC [10] [11], composite [12], adiabatic [13], or variable-rate pulses [14] [15]. Refocusing pulses can be spatially selective, spectrally selective, or non-selective. The most common spatially selective pulses include are SINC pulses, whereas non-selective pulses are almost always rectangular. Adiabatic refocusing pulses can provide excellent immunity to

B_1 field variations, but they require longer pulse widths and typically deposit more RF power. They can be used as non-selective refocusing pulses.

To examine how a refocusing pulse works, consider two magnetisation vectors \mathbf{h} and \mathbf{h}' which are precessing at slightly different speeds after the application of a 90° excitation pulse, as shown in Figure 2.5. Initially they are at the same position, but after a time t_1 they will be in different positions due to their differing speeds. A 180° refocusing pulse, \mathbf{B}_1 , is now applied along the y axis. This rotates both \mathbf{h} and \mathbf{h}' about the y axis by 180° and they then continue precessing as before. After another period of time $t_2 = t_1$, both magnetisation vectors will again coincide, producing a spin echo.

Refocusing pulses are widely used in many pulse sequences, e.g. RF spin echo [16], rapid acquisition with relaxation enhancement (RARE) [17] [18], spin echo EPI [19] and navigator echo generation [20]. Spatially selective refocusing pulses are most commonly employed in multi-slice 2D sequences. Single-slice 2D or single-slab 3D spin echo imaging can be performed with a spatially selective excitation pulse and a non-selective refocusing pulse, though using a spatially selective refocusing pulse can help to reduce artifacts. 3D acquisitions often use spatially non-selective refocusing pulses.

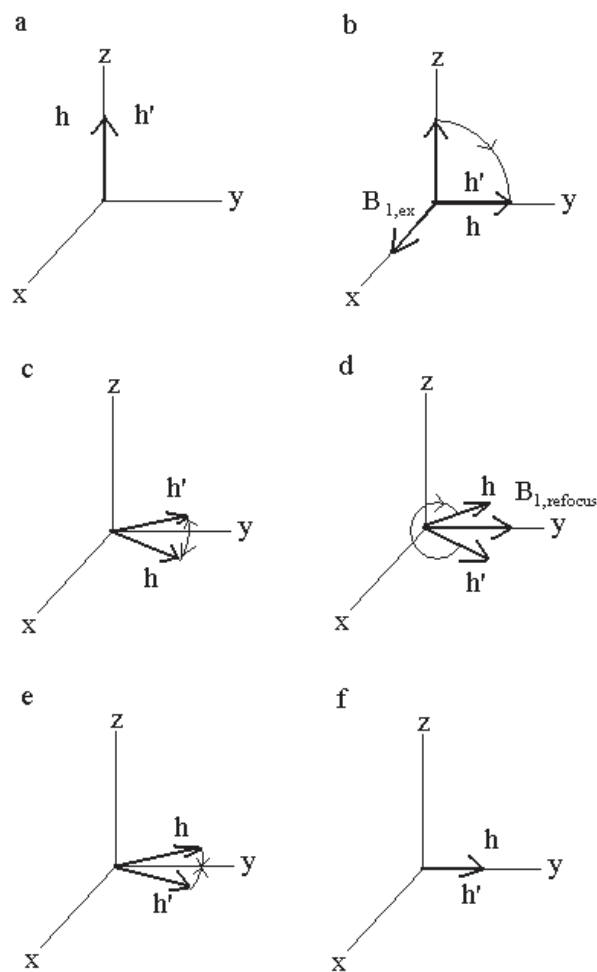


Figure 2.5: a) both spin isochromats are aligned with the z axis. b) after the RF excitation pulse $B_{1,ex}(t)$ is applied along the x axis both magnetisation vectors are rotated onto the y axis. c) due to off-resonance effects the magnetisation vectors precess at different speeds. d) applying the refocusing pulse $B_{1,refocusing}(t)$ flips each magnetisation vector about the y axis by 180° . e) after the refocusing pulse the magnetisation vectors continue to precess as indicated by the arrows. f) after a delay time both magnetisation vectors meet up at the y axis and form a spin echo. T_2 decay has caused the magnetisation vectors to reduce in size.

2.3 Pulse Sequences

When considering sequences of pulses, two important measurements of time frequently occur. These are the repetition time (TR), which is the time between repetitions of the pulse sequence, and the echo time (TE), which is the time between the application of the pulse and the peak in the received echo signal.

2.3.1 Gradient Echo Pulse Sequences

Gradient echo (GRE, see Figure 2.8b) is a class of pulse sequences that is primarily used for fast scanning [21]. This makes GRE particularly useful in 3D volume imaging and other applications that require short acquisition times, such as vascular and cardiac imaging or acquisitions that require breath-holds.

Rather than use a 180° RF refocusing pulse to form an echo, GRE pulse sequences use a gradient reversal on the frequency encoding axis to form an echo. A readout prephasing gradient lobe dephases the spin isochromats, and then a readout gradient that has opposite polarity rephases them. The peak of the GRE occurs when the area under the two gradient lobes is equal. Reducing the gradient area of the readout prephasing lobe allows partial-echo acquisition and reconstruction.

GRE acquisitions can be fast because the flip angle is typically less than 90° . This means that the longitudinal magnetisation component is never inverted by an RF refocusing pulse. This eliminates the need for a lengthy T_1 recovery and thus allows GRE sequences to have a short TR (e.g. 2-50 ms).

Other practical uses of GRE sequences are the production of images with hyperintense blood signal and producing susceptibility-weighted images. Because there is no 180° pulse to refocus the phase evolution caused by local variations in the magnetic fields, the phase of the spin isochromats in the transverse plane continues to accumulate during the entire echo time.

The convention employed by Philips on their Achieva systems is to call GRE sequences fast field echo (FFE) sequences.

2.3.2 Inversion Recovery Pulse Sequences

MRI can produce T_1 -weighted contrast images by exploiting the fact that many biological tissues have distinct T_1 relaxation times. In inversion recovery (IR, see Figure 2.6), an inversion pulse flips the longitudinal magnetisation from the $+z$ axis to the $-z$ axis. There is then a time delay, called the inversion time (TI), to allow the inverted magnetisation to recover toward its equilibrium value. Tissues with different T_1 values recover at different rates. Before the tissues can fully recover, a RF excitation pulse is applied. This pulse then converts the differences in the longitudinal magnetisation into differences in the transverse magnetisation. The resulting signals produce an image with T_1 -weighted contrast.

An IR pulse sequence consists of two parts separated by the TI. The first part consists of the inversion pulse with an optional spoiler gradient, as well as the associated slice-selection gradient. The second part is a self-contained pulse sequence, such as RF spin echo or EPI.

The first part is commonly referred to as an IR module, and the second part is often called the host sequence. Usually there is one IR module for each host sequence, but sometimes multiple IR modules may precede a host sequence, or a single IR module may be followed by many host sequences.

IR pulse sequences require long TR's to allow the T_1 -weighted contrast to fully develop. They therefore are mainly used with fast imaging 2D host sequences, and even then they can still have prohibitively long acquisition times.

IR sequences can benefit from being reconstructed as real images (as opposed to magnitude images) [22] [23]. This is because IR magnetisations range from $-M$ to $+M$ instead of from 0 to M . Reconstructing them as real images preserves this double dynamic range and thus can increase the contrast. This is known as phase-sensitive inversion recovery.

IR sequences are widely used, as they have a broad range of T_1 -weighted contrast and can be used to generate T_1 maps. They can also be used to selectively attenuate signals, e.g. lipid suppression or fluid attenuation.

2.3.3 Radio Frequency Spin Echo Sequences

A RF spin echo (RF SE, see Figure 2.7) is formed by an excitation pulse and one or more refocusing pulses [16]. Usually the excitation pulse is 90° and the refocusing pulse is 180° . SE images are typically obtained in 2D. The main advantage of an SE pulse sequence is its ability to

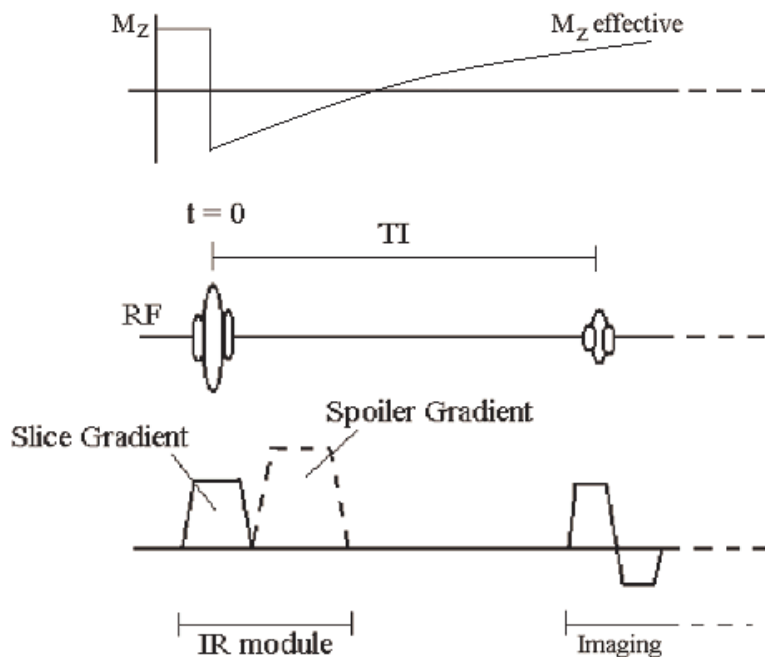


Figure 2.6: A generic IR pulse sequence. The optional spoiler gradient (dotted line) dephases any residual transverse magnetisation created by the inversion pulse.

obtain either T_1 , T_2 , or proton density weighted images. The contrast weighting achieved depends upon the TR and TE values selected. SE sequences are also particularly robust, being less prone to blurring and ghosting than EPI.

The 180° refocusing pulse also refocuses off-resonance effects, resulting in fewer artifacts from things such as main field inhomogeneity and magnetic susceptibility variations.

Gradient echoes are contrast weighted by the factor e^{-TE/T_2^*} and SE's are weighted by the factor e^{-TE/T_2} . As $T_2 \geq T_2^*$ SE's can use longer TE's to produce heavily T_2 -weighted images without excessive signal loss due to T_2^* .

SE images are not prone to chemical shift arising from water and fat signals in the same voxel, but they do suffer from chemical shift artifacts in the slice-selection and readout directions.

SE's only fill k-space one line at a time. This makes SE acquisition times that are much longer than echo-train pulse sequences. Having long acquisition times but high signal-to-noise ratios (SNR) makes SE pulses well suited to parallel imaging. When taking T_1 -weighted images, TR is reduced and hence acquisition times can be shorter, making SE pulses a popular choice when taking T_1 -weighted images.

It is possible to acquire two echoes per TR interval using an SE pulse sequence [24]. Doing so allows you to acquire a T_2 map, in which each pixel value gives you a quantitative measurement of the T_2 for the tissue within that pixel. A long echo train of SE's is acquired, and a fit of signal intensity measured in each pixel can be used to calculate T_2 . There are a few possible systematic errors which can lead to incorrect T_2 measurements however. Contributions from the stimulated echoes can introduce an unwanted T_1 -weighted variation into the echo train signal, which can make it hard to fit the decay to an exponential. Using magnitude reconstruction introduces a non-zero positive mean noise value. This can increase the measured T_2 and is a particular problem when measuring short T_2 's. Both of these problems can be overcome using more complicated fitting parameters, such as $S(TE) = N + Ae^{-TE/T_2} + \dots$

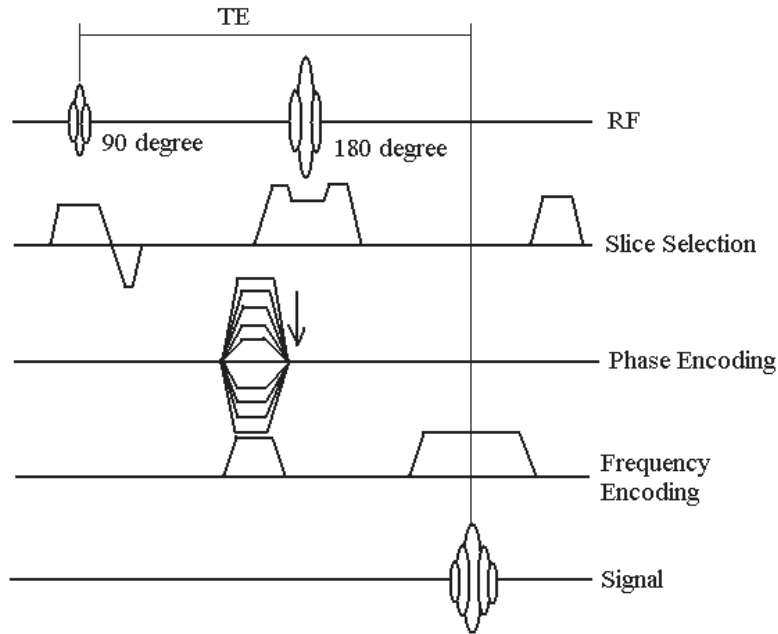


Figure 2.7: A generic RF SE pulse sequence.

2.3.4 Echo Planar Imaging

Echo planar imaging (EPI) is one of the fastest MRI pulse sequences, being able to produce a 2D image in a few tens of milliseconds [1]. EPI varies from conventional pulse sequences in the way the readout and phase-encoding gradients are applied. In EPI, a series of bipolar readout gradients are used to generate a train of gradient echoes. By applying a phase-encoding gradient, each gradient echo becomes distinctively spatially encoded so that multiple k-space lines can be sampled under the envelope of a FID or an RF spin echo. As gradient echoes can be produced so quickly, EPI generates images very rapidly. It is quite common for an EPI sequence to produce around 100 gradient echoes to generate a low-resolution 2D image from a single RF excitation. Such a sequence is called single shot EPI.

Although EPI can be used for both 2D and 3D imaging, most EPI applications are 2D to take advantage of its very short acquisition times. Typical EPI 2D sequences use orthogonal readout, phase-encoding, and slice-selection gradient waveforms. The slice-selection gradients are no different from the slice-selection gradients used in any other MRI pulse sequence. The readout and phase-encoding gradients are different from most other pulse sequences and need additional processing prior to image reconstruction. See Figure 2.8 for a comparison of an EPI acquisition to an RF pulse and a conventional GRE acquisition.

EPI is prone to a number of artifacts. The most common is ghosting along the phase-encoding direction. This can be caused by eddy currents, concomitant magnetic fields, and other system imperfections and physical phenomena. These ghosting artifacts are called Nyquist ghosts and can often be reduced or eliminated by calibration, reconstruction, or postprocessing. Chemical shift artifacts in EPI can be very severe along the phase-encoded direction, so some form of lipid suppression is usually necessary. Off-resonance effects (from susceptibility variations, B_0 inhomogeneities, eddy currents, etc.) can also severely distort EPI images. T_2^* decay during the formation of the gradient echo can also blur an EPI image.

Gradient-echo Echo Planar Imaging

A gradient-echo EPI (GR-EPI, see Figure 2.9) sequence begins with a selective excitation pulse to create an FID signal. A series of spatially encoded gradient echoes are then produced under the envelope of the

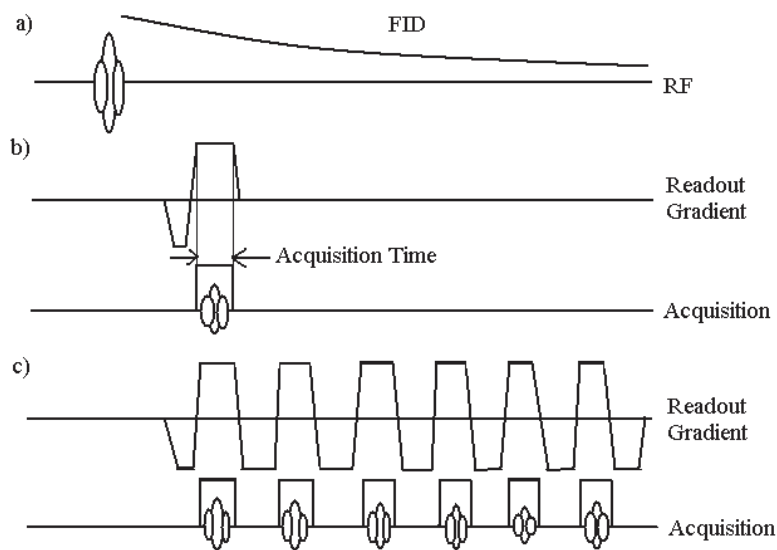


Figure 2.8: a) an RF excitation pulse, b) a conventional GRE acquisition, and c) an EPI acquisition.

FID using a combination of readout and phase-encoding gradients. As the TR of EPI is usually much longer than conventional gradient-echo pulse sequences, the flip angle of the excitation pulse can be set high (e.g. 90°) to maximise SNR. The excitation pulse is often designed as a spatial-spectral pulse to reduce lipid signals, or a spectrally selective pulse can be used to saturate the lipid signals. A spoiler gradient is often employed at the end of the pulse sequence to dephase any remaining transverse magnetisation.

Spin-echo Echo Planar Imaging

A 2D spin-echo EPI (SE-EPI, see Figure 2.10) pulse sequence is comprised of a 90° excitation pulse and a 180° refocusing pulse. The excitation pulse can be a spatial-spectral pulse or a pulse with linear or

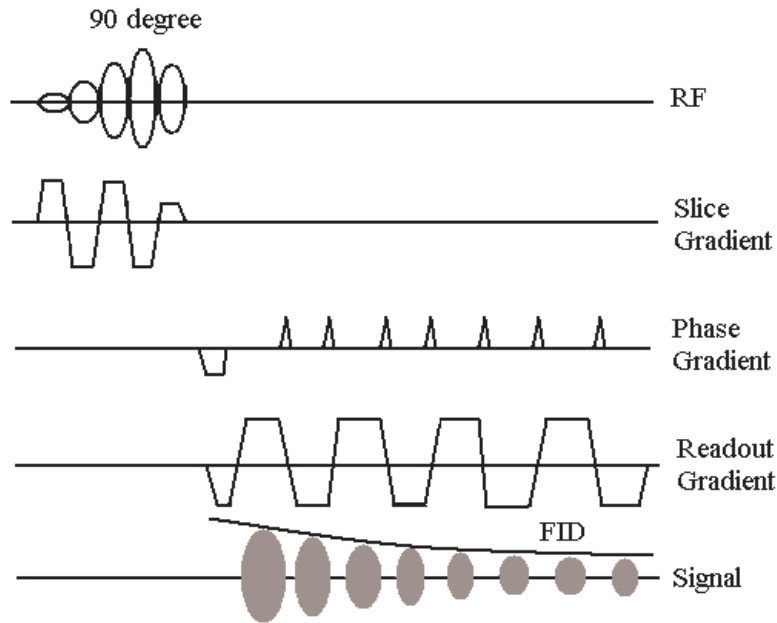


Figure 2.9: An example of a gradient-echo EPI sequence.

minimum phase preceded by a spectrally selective pulse to suppress lipid signals. A SINC pulse is typically used as the refocusing pulse. These two pulses generate a spin echo, and around the peak of this spin echo EPI readout and phase-encoding waveforms are played. These produce a series of spatially encoded gradient echoes. SE-EPI uses gradient echoes formed under the envelope of a spin echo to sample k-space lines, rather than under a FID, as gradient-echo EPI does. The slice-selection gradient waveform used in SE-EPI is the same as any other used in a spin-echo pulse sequence.

The effective TE of the sequence, TE_{eff} , is defined as the TE when the central k-space line is acquired. When TE_{eff} is the same as the TE of the spin echo, TE_{SE} , the sensitivity of the sequence to off-resonance effects drops considerably. This makes the image primarily T_2 weighted,

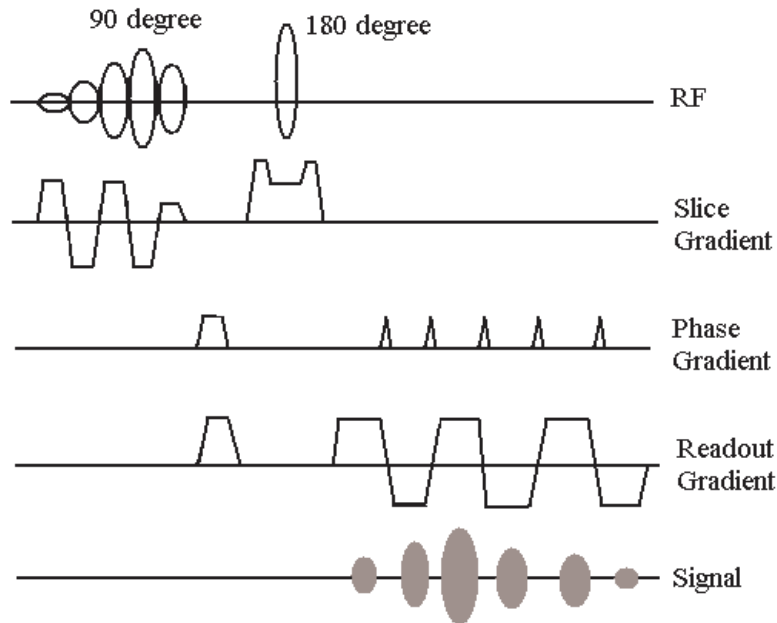


Figure 2.10: An example of a spin-echo EPI sequence.

rather than T_2^* weighted. This can be used to increase EPI image quality and to reduce the number of artifacts caused by off-resonance effects. The main drawback of SE-EPI is its reduced sensitivity to BOLD contrast.

T_2^* Mapping

It is possible to modify a gradient-echo EPI pulse sequence to produce a T_2^* map [24]. The EPI phase-encoding waveform is replaced by a conventional phase-encoding waveform that gives the same k_y for the entire echo train. After obtaining data for all the required phase-encoding steps, a stack of images are generated corresponding to a gradient echo. As each gradient echo has its own TE value under the FID envelope, a pixel-by-pixel plot of image intensity versus TE reveals the T_2^* decay

curve.

2.3.5 Sa2RAGE

The Sa2RAGE (saturation prepared by two rapid gradient echoes) sequence [25] has been developed to rapidly produce accurate 3D B_1 maps at high field strength. It consists of a 90° preparation pulse followed by two gradient echoes, and the entire pulse sequence has a short repetition time. The delay between the preparation pulse and the first GRE is kept very short and the delay between the preparation pulse and the second GRE is kept relatively long, which helps to make the sequence insensitive to T_1 -relaxation (see Figure 2.11 for a pulse sequence diagram). The ratio of the signals generated in the two GRE acquisition pulses can then be compared to a look-up table to determine the B_1 value for each voxel. The look-up table was established by numerically solving the Bloch equations taking into account the steady state condition.

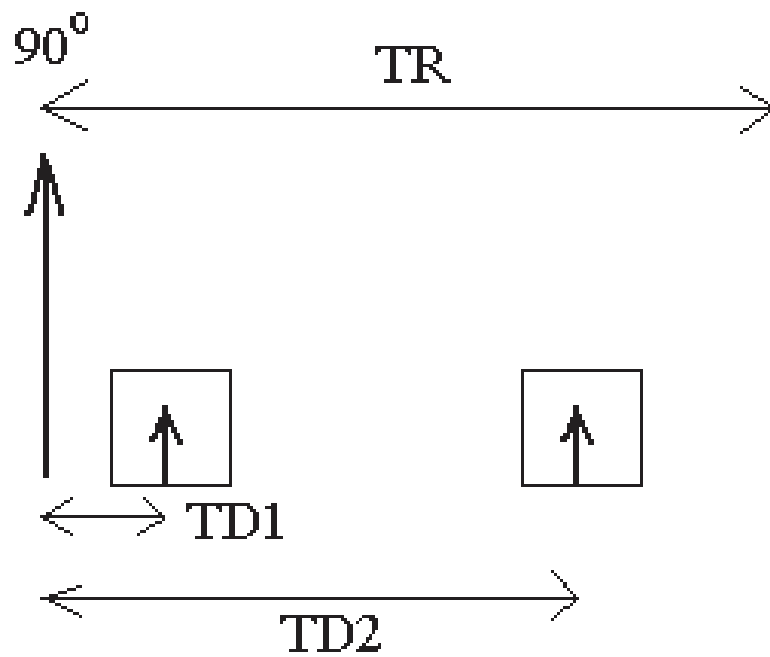


Figure 2.11: The Sa2RAGE sequence consists of an initial hard 90° pulse, followed by two GRE blocks. The first block occurs after time TD1 and the second occurs after a time TD2. The GRE blocks themselves have very short TR times.

2.4 Image Acquisition

The Handbook of MRI Pulse Sequences by Bernstein et al. [26] provides a very good summary of the image acquisition process. MRI data is acquired at different k-space points and a Fourier transform (FT) is used to obtain the final image.

2.4.1 k-Space and k-Space Trajectories

The Fourier conjugate to the spatial domain is k-space. The concept of k-space greatly simplifies the understanding of many pulse sequences, such as echo-planar imaging (EPI) or spiral scans.

The time-domain signal created by a transverse magnetisation is

$$S(t) = \int \mathbf{M}_\perp(\mathbf{r})\mathbf{B}_\perp(\mathbf{r}) \exp^{-j\phi(\mathbf{r},t)} d^3r \quad (2.21)$$

where $\mathbf{M}_\perp(\mathbf{r})$ is the transverse magnetisation, $\mathbf{B}_\perp(\mathbf{r})$ is the component of the receive coil B_1 field that lies in the transverse plane, \mathbf{r} is a spatial variable, $d^3r = dxdydz$, and the accumulated phase (in radians) is:

$$\phi(\mathbf{r}, t) = \gamma \int_0^t \mathbf{r} \cdot \mathbf{G}(t') dt', \quad (2.22)$$

where \mathbf{M}_\perp and \mathbf{B}_\perp are both complex quantities and \mathbf{G} is the gradient waveform

$$\mathbf{G} = \frac{\partial B_z}{\partial x} \hat{x} + \frac{\partial B_z}{\partial y} \hat{y} + \frac{\partial B_z}{\partial z} \hat{z} \equiv G_x \hat{x} + G_y \hat{y} + G_z \hat{z}. \quad (2.23)$$

Relaxation and diffusion have been neglected, and the integral is taken over the entire excited portion of the sample.

Now define

$$\mathbf{k}(t) = \frac{\gamma}{2\pi} \int_0^t \mathbf{G}(t') dt'. \quad (2.24)$$

The space that $\mathbf{k}(t)$ resides in is known as k-space, and $\mathbf{k}(t)$ has units of inverse distance. Equation 2.21 now becomes

$$S(t) = \int \mathbf{M}_\perp(\mathbf{r})\mathbf{B}_\perp(\mathbf{r}) \exp^{j2\pi\mathbf{k}(t)\cdot\mathbf{r}} d^3r. \quad (2.25)$$

The signal $S(t)$ is just the FT of the weighted transverse magnetisation $\mathbf{M}_\perp(\mathbf{r})\mathbf{B}_\perp(\mathbf{r})$. As time evolves, $S(t)$ traces a path $\mathbf{k}(t)$ in k-space. The speed of k-space traversal is

$$\left\| \frac{d\mathbf{k}}{dt} \right\| = \frac{\|\gamma\mathbf{G}\|}{2\pi}. \quad (2.26)$$

The total distance covered in k-space during any time interval is determined by the area under the gradient waveform $\mathbf{G}(t)$ during that time interval.

The k-space trajectory is the path traced out by $\mathbf{k}(t)$. It influences which types of artifacts will be present in the final images, determines which image reconstruction algorithm is required and also illustrates the acquisition strategy. The centre of k-space contains the signal to noise and contrast information of an image, while the outer regions of k-space contain the high resolution information.

A Cartesian raster trajectory (see Figure 2.12A) is where each line of k-space corresponds to the frequency-encoded readout at each value of the phase-encoding gradient. All lines in the raster are parallel and separated by equal distance in k-space. Typical Cartesian rasters use between 128 and 512 phase-encoded views. Cartesian rasters have fewer resonance offset, eddy current and other imperfection artifacts compared to non-Cartesian k-space trajectories.

A projection acquisition (PA) k-space trajectory (see Figure 2.12B)

consists of spokes that radiate out from the origin. PA's are less efficient than Cartesian rasters because of their non-uniform sampling density. This can lead to long scan times if the Nyquist criterion is satisfied for the edge of k-space. PA's can have streak artifacts caused by undersampling in the azimuthal direction. If these streaks are not a problem, it is possible to use a PA to achieve shorter scans than a Cartesian raster would produce without sacrificing spatial resolution. Their higher sampling density in the centre of k-space can also give them a better SNR.

The EPI k-space trajectory (see Figure 2.12C) is an improved version of the Cartesian raster. Only a single (or a few) RF pulses are needed. This greatly decreases the scan time. The number of excitation pulses required to cover k-space is referred to as the number of shots. A series of gradient echoes allows each RF pulse to cover several k-space lines, with the directions of the k-space lines alternating for each traversal of k-space. The main disadvantages of EPI are geometric distortion caused by off-resonant spins and Nyquist ghosts caused by the alternating k-space trajectory reversals.

The spiral trajectory (see Figure 2.12D) is efficient at covering k-space and has a fast scan time compared to a Cartesian trajectory. In a spiral trajectory the number of shots is also called the number of interleaves. The spiral trajectories efficiency comes from the fact that only a few interleaves (approximately 16) are required to cover all of k-space. Spiral trajectories produce blurred images when the spins are off-resonance. Spirals are often used with small FOV's that are near

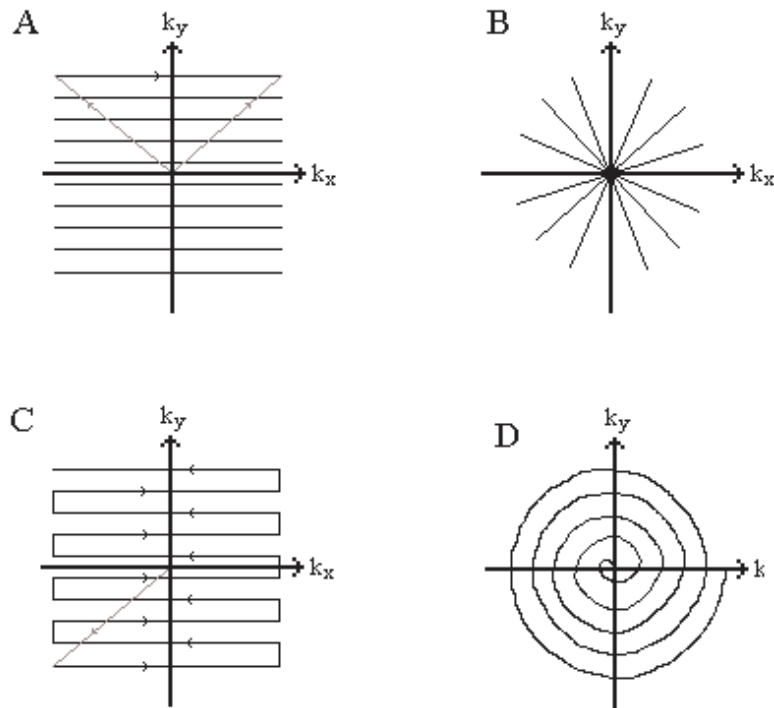


Figure 2.12: A: A Cartesian raster trajectory. B: A projection acquisition trajectory. C: An echo-planar imaging trajectory. D: A spiral trajectory.

the center of the magnet, such as in cardiac imaging and fMRI, where blurring is likely to be dominated by other factors.

2.4.2 Frequency-Encoding

In order to acquire the data from k -space either frequency or phase-encoding can be used. In frequency-encoding the precession frequency is varied linearly in a direction, e.g. x , by applying a gradient G_x in that direction. The full bandwidth in the x direction would then be $(\gamma/2\pi)G_xD$, where D is the object length. If a FOV L_x is required,

where $L_x < D$, w must be reduced by applying a band limiting filter prior to sampling. This gives

$$\Delta\nu = \frac{1}{2} \frac{\gamma}{2\pi} G_x L_x. \quad (2.27)$$

The AD converter then samples the signal at intervals of

$$\Delta t = \frac{1}{2\Delta\nu} \quad (2.28)$$

and

$$\Delta k_x = \frac{\gamma}{2\pi} G_x \Delta t. \quad (2.29)$$

This leads to the k-space Nyquist requirement:

$$\Delta k_x = \frac{1}{L_x} \quad (2.30)$$

If N_x readout points are acquired, the maximum extent of k-space is

$$N_x \Delta k_x = \frac{N_x}{L_x} = \frac{1}{\Delta x} \quad (2.31)$$

where Δx is the image resolution.

2.4.3 Phase-Encoding

Phase-encoding is used with Cartesian k-space sampling and is typically used to spatially encode information orthogonal to the frequency-encoded direction. Phase-encoding is achieved by creating a linear spatial variation of the phase of the magnetisation. This is done by applying a gradient while the magnetisation is in the transverse plane but before the readout. Varying the area under the phase-encoding gradient changes the amount of linear phase variation introduced. The resulting

signals can be reconstructed using FT's to recover spatial information about the object being scanned.

For a y phase-encoding gradient G_y , the angular frequency of precession in the B_0 rotating reference frame is

$$\omega = \gamma G_y y. \quad (2.32)$$

The phase ϕ (in radians) of the transverse magnetisation at the end of the phase-encoding is:

$$\phi(y) = y\gamma \int_0^T G_y(t') dt' = 2\pi k_y y \quad (2.33)$$

where T is the duration of G_y .

The signal detected is the vector sum of the magnetisation of all the nuclear spins in the object. The magnetisations can be represented as a complex sum of the x and y terms,

$$\mathbf{M}_\perp = \mathbf{M}_x + j\mathbf{M}_y, \quad (2.34)$$

and the signal detected from a one-dimensional object is

$$S(k_y) = \int \mathbf{M}_\perp(y) \exp^{-j\phi(y)} dy. \quad (2.35)$$

This must then be discretised and turned into a sum so that

$$S(k_y) = \sum_{n=0}^{N-1} \mathbf{M}_\perp(n\Delta y) \exp^{-2\pi j(n\Delta y)k_y}, \quad (2.36)$$

where $y = n\Delta y$, Δy is the pixel size and N is the number of pixels.

Repeating phase-encoding N times for N values of G_y produces N sets of phase-encoding twists, or k_y values. This provides sufficient information for $\mathbf{M}_\perp(n\Delta y)$ to be reconstructed. N phase-encoding lines

will cover a maximum k-space area of $(N - 1)\Delta k_y$, where Δk_y is the k-space phase-encoding step size. Usually an even number of phase-encoding lines are used that straddle the $k_y = 0$ line. For N phase-encoded steps that are acquired sequentially starting at the top edge of k-space

$$k_y(m) = k_{y,\max} - m\Delta k_y, \quad m = 0, 1, \dots, N - 1 \quad (2.37)$$

where $k_{y,\max}$ is the starting (top-edge) phase-encoding location given by

$$k_{y,\max} = \frac{1}{2} (N - 1) \Delta k_y. \quad (2.38)$$

The resulting phase-encoding locations are

$$k_y(m) = \left(\frac{N - 1}{2} - m \right) \Delta k_y \quad (2.39)$$

which produce the following signal

$$S(m) = \sum_{n=0}^{N-1} \mathbf{M}_\perp(n\Delta y) \exp^{-2\pi j(n\Delta y)((N-1)/2-m)\Delta k_y}. \quad (2.40)$$

In order to satisfy the Nyquist criterion

$$\Delta k_y = \frac{1}{L_y} = \frac{1}{N\Delta y} \quad (2.41)$$

where $L_y = N\Delta y$ is the FOV in the y direction. This implies that the maximum k-space sampling extent is

$$N\Delta k_y = \frac{1}{\Delta y} \quad (2.42)$$

and hence

$$S(m) = \sum_{n=0}^{N-1} \mathbf{M}_\perp(n\Delta y) \exp^{-\pi j n(N-1)/N} \exp^{2\pi j m n/N}. \quad (2.43)$$

The $\exp^{-\pi j n(N-1)/N}$ factor can be thought of as part of the phase of \mathbf{M}_\perp and can be ignored when reconstructing a magnitude image (but not when reconstructing a phase image).

Phase-encoded images are reconstructed using a discrete inverse FT,

$$\mathbf{M}_\perp(n\Delta y) \exp^{-\pi j n(N-1)/N} = \frac{1}{N} \sum_{m=0}^{N-1} S(m) \exp^{2\pi j m n/N}. \quad (2.44)$$

If the phase-encoding step size is chosen to be larger than $\Delta k_y = 1/N\Delta y$ aliasing will occur, in which replicates of the image overlap or wrap around in the phase-encoding direction. It is not possible to eliminate this aliasing using an anti-aliasing band-pass filter, as is the case in frequency-encoding.

It is possible to speed up phase encoding by using SENSE [27]. This is where you have multiple receive elements in your coil, each of which samples a subset of k-space to reduce the total acquisition time. See section 2.6 which describes SENSE later in this thesis for more details.

2.4.4 Readout Bandwidth and Frequency Bandwidth

The readout bandwidth is defined as the range of spin precession frequencies across the field-of-view (FOV) in the readout direction. This can be specified as either the full-bandwidth or the half-bandwidth. When specified as the half-bandwidth it is given the symbol $\Delta\nu$. The sampling time per complex point Δt (also known as the dwell time) is the inverse of the full readout bandwidth.

The data in k-space is sampled discretely using an analogue to digital (AD) converter. If the frequency bandwidth, w , of the spectrum

is greater than the reciprocal of the dwell time, replicated FT signals are produced which overlap. This produces aliasing in the final image and must be eliminated by windowing the spectrum so that $w \leq 1/\Delta t$ before performing the FT.

2.4.5 Noise

Generally speaking, the noise in an image is generated by random fluctuations in the receive coil electronics and the sample.

$$\text{noise} \propto \sqrt{4k_B T \cdot BW \cdot R_{\text{eff}}}, \quad (2.45)$$

where k_B is Boltzman's constant ($1.38 \times 10^{-23} JK^{-1}$), T is the temperature of the coil, BW is the bandwidth of the receive coil and R_{eff} is effective resistance of the coil loaded by the body. The effective resistance is a combination of the resistance of the sample, the resistance of the coil and the resistance of the electronics,

$$R_{\text{eff}} = R_{\text{sample}} + R_{\text{coil}} + R_{\text{electronics}}. \quad (2.46)$$

In most modern systems the resistance of the electronics and the coil become negligible compared to the resistance of the sample, which is proportional to the volume that the coil is sensitive to;

$$R_{\text{eff}} \approx R_{\text{sample}} \propto V_{\text{sensitive}}. \quad (2.47)$$

2.5 Specific Absorption Rate

The specific absorption rate (SAR) is the amount of RF energy deposited in the subject being scanned and is measured in watts per kilogram. It is defined as

$$\text{SAR} = C_P \frac{\Delta T}{\Delta t}, \quad (2.48)$$

where C_P is the specific heat capacity of the tissue in question, ΔT is the change in temperature and Δt is the time taken for the temperature rise to occur. To ensure scans are safe SAR limits [28] are imposed based upon the anatomy being scanned (e.g. the SAR limits for the head are lower than the SAR limits for the extremities, as the head has much more delicate and important anatomical structures than the hand or foot). These limits are average SAR over a six minute period. If a scan would exceed these limits it will fail to run.

SAR can be theoretically calculated using the following equation:

$$\text{SAR} = \int_{\text{sample}} \frac{\sigma(r) \|E(r)\|^2}{\rho(r)} dr, \quad (2.49)$$

where $\sigma(r)$ is the conductivity of the sample, $E(r)$ is the electric field and $\rho(r)$ is the sample density. In practice SAR is often measured or simulated rather than theoretically calculated.

SAR values not only depend upon the coil being used, but also on the position of the subject relative to the coil and the amount of power being used for the pulse. The power requirements of the pulse are more of an issue for the scanner operator than the coil designer, and can vary from scan to scan. The SAR inherent in the coil design is evaluated during the coil's planning and construction and is then fixed for all

scans. Simulations must be performed to determine the SAR generated by the coil with subjects positioned as intended for the coil's use. This information is then given to the scanner along with information about the pulse sequence being used to determine if a particular scan will exceed the SAR limits.

Sometimes, when SAR simulations are being performed, it is found that SAR is too high with the subject in a certain position relative to the coil. If this is the case then the coil must be altered so that the subject cannot get into that position (e.g. a spacer is added to prevent the subject from getting too close) or strict scanning protocols are introduced (e.g. scans are only permitted if the subject has their arms above their heads rather than by their sides).

2.6 Sensitivity Encoding

SENSE [29] is a parallel imaging technique which can be used in MRI to accelerate image acquisition. To utilise SENSE, RF coils must be designed with multiple reception elements. Each coil element takes an image which is weighted by that element's spatial sensitivity pattern. Knowledge of each element's spatial sensitivity pattern can then be used to combine the individual images to get a complete image in a fraction of the time taken to take a complete image using a single element.

By increasing the distance of sampling positions in k-space while maintaining the maximum number of k-values it is possible to reduce the number of Fourier encoding steps. This allows for a reduced scan time without sacrificing spatial resolution. The factor by which the number of k-space samples is reduced is called the reduction factor R .

The first step in SENSE reconstruction is to create an aliased image for each array using a discrete Fourier transform (DFT). The second step is to use these aliased images to create a full-FOV image. For each pixel in the reduced FOV the signal contributions from a number of positions in the full FOV need to be separated. This is possible because each single-coil image signal superposition occurs with different weights according to local coil sensitivities. Let n_P denote the number of pixels superimposed and n_C the number of coils used. The vector \mathbf{a} is then constructed from the complex image values that a chosen pixel has in the intermediate images. The $n_C \times n_P$ sensitivity matrix S is formed from the complex coil sensitivities at the n_P superimposed positions:

$$S_{\gamma,\rho} = s_{\gamma}(\mathbf{r}_{\rho}), \quad (2.50)$$

where γ counts the coils and ρ counts the superimposed pixels, \mathbf{r}_ρ denotes the location of pixel ρ , and s_γ is the spatial sensitivity of the coil γ . The sensitivity matrix is then used to calculate the unfolding matrix U :

$$U = \left(S^H \Psi^{-1} S \right)^{-1} S^H \Psi^{-1}, \quad (2.51)$$

where H indicates the transposed complex conjugate, and Ψ is the $n_C \times n_C$ receiver noise matrix. The receiver noise matrix describes the levels and correlation of noise in the receiver channels. Signal separation is then performed by

$$\mathbf{v} = U \mathbf{a}. \quad (2.52)$$

The resulting vector \mathbf{v} has the length n_P and lists separated pixel values for the originally superimposed positions. This procedure is repeated for each pixel so that the entire FOV can be obtained.

When considering the signal-to-noise ratio (SNR) of a SENSE image a geometry factor (g-factor) must also be considered. The g-factor is simply the ratio of the SNR for an optimal, unaccelerated image and the SNR of the accelerated image with an additional factor of the acceleration factor R which accounts for the SNR loss due to averaging fewer required signals [30],

$$\text{g-factor} = \frac{SNR_{optimal,unaccelerated}}{SNR_{accelerated} \sqrt{R}}. \quad (2.53)$$

2.7 Transmit Sensitivity Encoding

Transmit-SENSE [31] uses similar principles to do the opposite, i.e. multiple transmission elements with different spatial sensitivity patterns and different RF waveforms can be used to excite the entire image volume with short duration RF pulses without sacrificing spatial definition. Transmit-SENSE also has the potential to produce less SAR by fine-tuning the pulses delivered to lower the total energy deposited, and can be used to overcome B_1 inhomogeneities at ultra-high field strengths (such as seven tesla).

The main hardware of transmit-SENSE is a multielement transmit array. Each individual transmit element excites a specific magnetisation pattern which may show inhomogeneities. However, when all the excitation patterns are combined these inhomogeneities should disappear. The elements combine to transmit a signal that has a large B_1^+ (i.e. in the positive rotating frame) and receive signal with strong B_1^- (i.e. in the negative rotating frame) [32].

When designing a transmit-SENSE system, the spatial patterns $P_n(\mathbf{r})$ that need to be excited by each of the N transmit coils, which each have a sensitivity profile $S_n(\mathbf{r})$, must be determined in order to obtain the desired excitation pattern $P_{\text{des}}(\mathbf{r})$. This can be written mathematically as

$$P_{\text{des}}(\mathbf{r}) = \sum_{n=1}^N S_n(\mathbf{r})P_n(\mathbf{r}). \quad (2.54)$$

The $S_n(\mathbf{r})$ are found using B_1 mapping techniques. Equation 2.54 is linear, which is an important part of transmit-SENSE. This allowed transmit-SENSE to be tested experimentally before suitable multichan-

nel hardware was available by performing subexperiments and then combining the images from each subexperiment at the end to obtain the final image [2].

To derive the waveforms, $B_{1n}(t)$, that each of the N elements must be driven by, the following steps need to be followed. First, the $P_n(\mathbf{r})$ must be Fourier transformed to bring it into k-space. This is because the B_1 waveform that is used to excite the desired magnetisation pattern is just its Fourier transform multiplied by trajectory dependent weighting coefficients sampled along a k-space trajectory. Equation 2.54 has now become

$$P_{\text{des}}(\mathbf{r}) = \sum_{n=1}^N S_n(\mathbf{r})A(\mathbf{r}, \mathbf{k})p_n(\mathbf{k}) \quad (2.55)$$

where $A(\mathbf{r}, \mathbf{k}) \sim \exp(j\mathbf{r}\mathbf{k})$ is the Fourier encoding matrix.

The next step is to invert equation 2.55. To make this inversion easier, the k-space coil sensitivities $S_n(\mathbf{k})$ are grouped into a single matrix s_{full} . Similarly p_{full} is formed from the individual $p_n(\mathbf{k})$. Both of these new matrices are invertible. Now

$$p_{\text{des}}(\mathbf{k}) = s_{\text{full}}(\mathbf{k})p_{\text{full}}(\mathbf{k}) \quad (2.56)$$

and the pseudoinverse (regularised with the free parameter λ) is found:

$$p_{\text{full}} = s_{\text{full}}^H \left(s_{\text{full}} s_{\text{full}}^H + \lambda \right)^{-1} p_{\text{des}}, \quad (2.57)$$

where H denotes the transposed complex conjugate.

Now the special case of a Cartesian, echo-planar-like k-space trajectory is considered. This case can be solved in the spatial domain, leading to a small part of the sensitivity matrix being inverted. The

solution for the $p_n(\mathbf{k})$, written as an integral over the field of excitation (FoX), is

$$p_n(\mathbf{k}) = \int_{\text{FoX}} h_n(\mathbf{r}) P_{\text{des}}(\mathbf{r}) \exp^{j2\pi\mathbf{k}\mathbf{r}} d\mathbf{r}. \quad (2.58)$$

Here the h_n have been obtained from the inversion of the sensitivity matrix $C(S_1(\mathbf{r}), S_2(\mathbf{r}), \dots, S_N(\mathbf{r}))$. Once the $p_n(\mathbf{k})$ have been calculated from either equation 2.57 or equation 2.58, the mapping between \mathbf{k} and t is performed according to the chosen k-space trajectory. The desired waveforms for each individual transmission element can be calculated via

$$B_{1n}(t) = W(t)p_n(\mathbf{k}(t)), \quad (2.59)$$

where $W(t)$ is the Jacobian that maps from k-space to t-space for the chosen k-space trajectory.

Using multiple transmission elements can result in several benefits: firstly is a reduction of the pulse duration by a reduction factor R . Secondly is to increase the spatial definition of the excitation pattern without having to increase the pulse duration. Thirdly, system imperfections, such as B_0 inhomogeneities, k-space trajectory imperfections and concomitant gradient effects can be compensated for. Finally, the use of multiple transmission coils can reduce the required RF power, thus reducing the SAR.

Pinkerton et al. [33] have proposed a parameter E which can be used to rate a transmit-SENSE coil's performance under simulated or experimental conditions. The definition of E begins with the spatial noise amplification g -factor (g)[29].

$$g_\rho = \sqrt{\left[(S^H \Psi^{-1} S)^{-1} \right]_{\rho, \rho} (S^H \Psi^{-1} S)_{\rho, \rho}} \geq 1, \quad (2.60)$$

where Ψ is the receiver noise matrix, and ρ is the index of the voxel under consideration. The g -factor is used to find the ratio of temporal noise in SENSE ($\sigma_{t,\text{SENSE}}$) to that of a fully acquired image ($\sigma_{t,\text{full}}$),

$$\frac{\sigma_{t,\text{SENSE}}}{\sigma_{t,\text{full}}} = \sqrt{1 + (g^2 R - 1) * \left(\frac{\sigma_{n,\text{full}}^2}{\sigma_{n,\text{full}}^2 + \sigma_{\text{ph}}^2} \right)}, \quad (2.61)$$

where $\sigma_{n,\text{full}}$ is the intrinsic noise and σ_{ph} is the physiological noise. From this ratio, E can be defined.

$$E = \frac{\sigma_{t,\text{full}} \text{SNR} \sqrt{R}}{\sigma_{t,\text{SENSE}}} \quad (2.62)$$

Note that E approaches the conventional measure of performance, SNR/g , in the intrinsic noise-dominated regime. A high E value indicates a coil design with a better performance under the given conditions than a coil with a lower E value.

2.8 Computational Electromagnetics

Computational electromagnetics (CEM) is the process of modeling electromagnetic systems using a computer. Most CEM methods can be classified as either differential equation or integral equation methods, as well as into either time domain or Fourier domain methods [34]. Thus there are four main types of CEM. Several CEM methods are introduced here. The method used for this research was the finite difference time domain method (FDTD) [35].

2.8.1 Finite Difference Time Domain

Finite Difference Time Domain (FDTD) is a method of simulating 3D EM wave problems. It performs its calculations in the time domain, using Maxwell's equations in a differential form. It works by dividing the system being modeled into many cubes that typically have a maximum dimension of one-tenth of the wavelength of the EM radiation being modeled. These cubes are called Yee cells.

The simulation models the propagation of EM radiation through the system by breaking the propagation into finite time steps (the time taken for the radiation to pass through one Yee cell), and then propagating the EM radiation through each Yee cell using Maxwell's equations (working in the time domain). In a Yee cell, the electric fields are sampled along the edges of the cell and the magnetic fields are sampled on the faces (see Figure 2.13). The Yee cells can be set to represent different materials by altering the boundary conditions used for the Maxwell's equations in each one, e.g. setting $E = 0$ inside a Yee cell

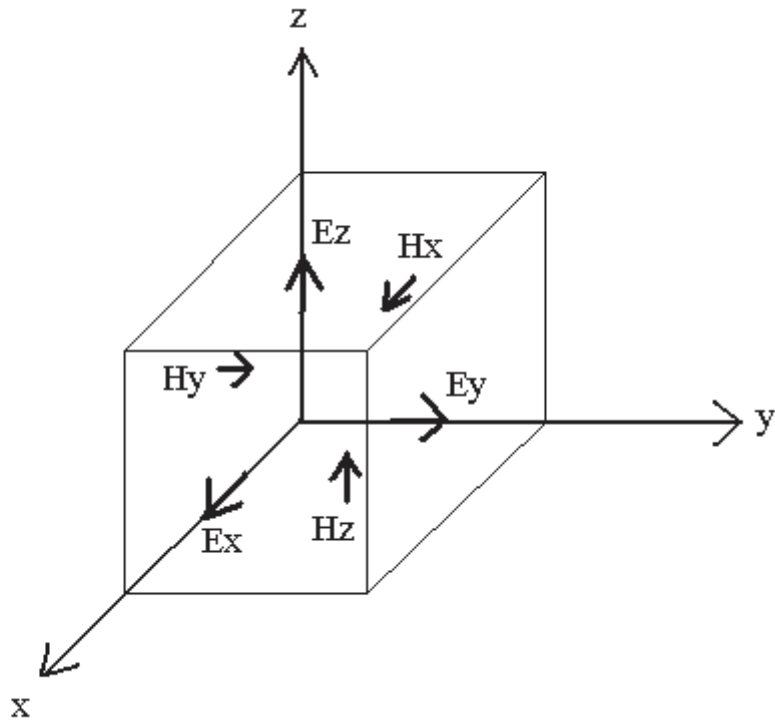


Figure 2.13: A Yee Cell. The electric fields are placed on the edges while the magnetic fields are placed on the faces.

makes that cell behave as if it were a perfect conductor.

In order to properly take account of the effect of the outside world on the simulated system, the sample-space is surrounded by several layers of Yee cells which lead to pre-set boundary conditions, ensuring a smooth transition from the sample to the 'outside' of the simulation and therefore making the simulation stable.

2.8.2 Transmission Line Modeling

Transmission line modeling (TLM) is a time domain method of simulating EM systems [36]. It is founded upon the analogy between electrical

circuits and physical systems. In one dimension, we can divide an EM system into discrete circuit elements, each with a capacitance and inductance, as shown in Figure 2.14. The system is also discretised in time and knowledge of the behavior of circuits can be used to determine the evolution of the physical system. For example, derivative terms in the expressions for the physical system can be represented by voltages across inductors, and integral terms can be represented by voltages across capacitors.

As a demonstration, consider the propagation of an EM field in 1D. In such a physical system, the current density i is given by:

$$\frac{\partial^2 i}{\partial x^2} = \mu\epsilon \frac{\partial^2 i}{\partial t^2} + \mu\sigma \frac{\partial i}{\partial t}, \quad (2.63)$$

where μ is the magnetic permeability, ϵ is the electrical permittivity and σ is the electrical conductivity. A circuit that is analogous to this system can be set up as shown in Figure 2.15. The 1D space is split up into a sequence of circuits, each separated by a distance Δx . Both the voltage V and the current i are functions of time. Kirchoff's voltage and current laws can be applied to the circuit to give the following equations (provided that $\Delta x \rightarrow 0$):

$$-\frac{\partial V}{\partial x} \Delta x = L \frac{\partial i}{\partial t} \quad (2.64)$$

$$-\frac{\partial i}{\partial x} \Delta x = C \frac{\partial V}{\partial t} + \frac{V}{R} \quad (2.65)$$

$$\Rightarrow \frac{\partial^2 i}{\partial x^2} = \frac{LC}{(\Delta x^2)} \frac{\partial^2 i}{\partial t^2} + \frac{L}{(\Delta x^2)R} \frac{\partial i}{\partial t} \quad (2.66)$$

Equation 2.63 can be compared to equation 2.66 to see that the physical system and the circuit are indeed analogous; only the numerical factors before the differential terms are different in each equation.

The same system can also be considered with a harmonic input, i.e. $i(x, t) = i_0 \cos(\omega t - \beta x)$. Now the first term of the right-hand-side (RHS) of equation 2.63 describes wavelike behavior, and given that $\partial i / \partial t \sim \omega i$ and $\partial^2 i / \partial t^2 \sim \omega^2 i$, we can see that

$$|\text{wave term}| \sim \mu \epsilon \omega^2. \quad (2.67)$$

The second term on the RHS describes diffusion-like behavior:

$$|\text{diffusion term}| \sim \mu \sigma \omega. \quad (2.68)$$

We can take the ratio of these two terms to obtain a parameter, $\omega \epsilon / \sigma$, which we can use to determine which type of behavior dominates. If $\omega \epsilon \gg \sigma$ then wave behavior dominates, such as EM waves propagating through air or in low-loss dielectrics at high frequencies. If $\omega \epsilon < \sigma$ diffusion through the medium prevails, such as in propagation at low frequencies through lossy media. This is a quasi-static regime.

These basic principles of TLM can be expanded to 2D and 3D by simply using 2D and 3D circuits. The circuit used for modeling EM wave propagation in 2D is given in Figure 2.16.

2.8.3 Method of Moments

The method of moments is a general procedure for solving linear equations. If an EM system can be represented by a linear equation (i.e. a sum of impedance terms for each element in the system), then the method of moments can be used to solve it.

Consider the inhomogeneous equation

$$L(f) = g, \quad (2.69)$$

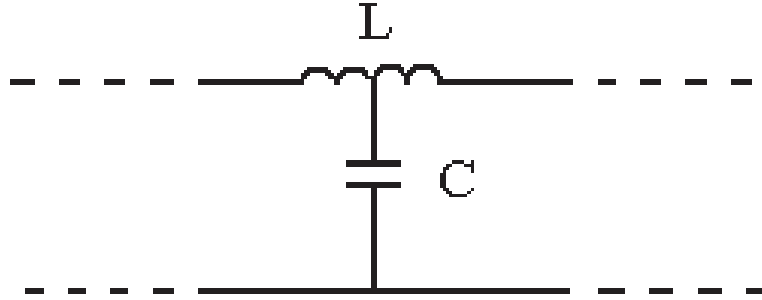


Figure 2.14: The circuit element used in TLM that is equivalent to a 1D region of a wire.

where L is a linear operator, g is known and f is to be determined. Expansion (or basis) functions, f_n are then used to expand f in the domain of L so that

$$f = \sum_n \alpha_n f_n, \quad (2.70)$$

where α_n are constants. This gives

$$\sum_n \alpha_n L(f_n) = g. \quad (2.71)$$

Now define a set of weighting functions $w_1, w_2, w_3 \dots$ in the range of L , and take the inner product of 2.71 with each w_m so that

$$\sum_n \alpha_n \langle w_m, Lf_n \rangle = \langle w_m, g \rangle, \quad (2.72)$$

or, in matrix form

$$[l_{mn}] = \begin{bmatrix} \langle w_1, Lf_1 \rangle & \langle w_1, Lf_2 \rangle & \dots \\ \langle w_2, Lf_1 \rangle & \langle w_2, Lf_2 \rangle & \dots \\ \dots & \dots & \dots \end{bmatrix} \quad (2.73)$$

$$[\alpha_n] = \begin{bmatrix} \alpha_1 \\ \alpha_2 \\ \vdots \end{bmatrix} \quad (2.74)$$

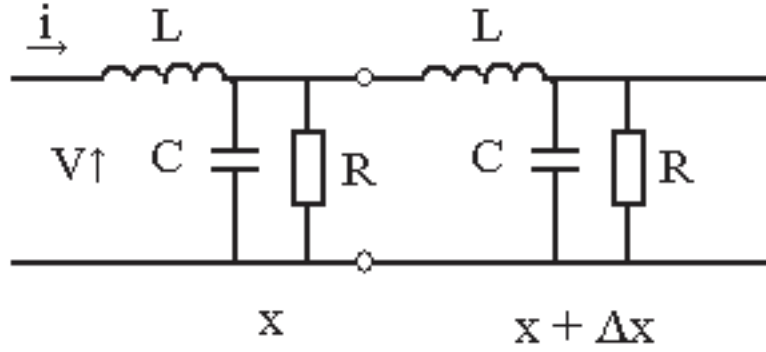


Figure 2.15: The circuit equivalent for the derivation of a transmission line in 1D.

$$[g_m] = \begin{bmatrix} \langle w_1, g \rangle \\ \langle w_2, g \rangle \\ \vdots \end{bmatrix} \quad (2.75)$$

If $[L]$ is non-singular then its inverse $[L^{-1}]$ exists and therefore

$$[\alpha_n] = [L_{nm}^{-1}] [g_m], \quad (2.76)$$

thus

$$f = \sum_n \alpha_n f_n. \quad (2.77)$$

To get a concise expression for the result, define a matrix of functions

$$[\tilde{f}_n] = \begin{bmatrix} f_1 & f_2 & f_3 & \dots \end{bmatrix} \quad (2.78)$$

and hence write

$$f = [\tilde{f}_n] [\alpha_n] = [\tilde{f}_n] [L_{mn}^{-1}] [g_m]. \quad (2.79)$$

The solution obtained from the method of moments is either approximate or exact, depending on whether we have an infinite or finite number of f_n and w_n . In order for a suitable solution to be obtained,

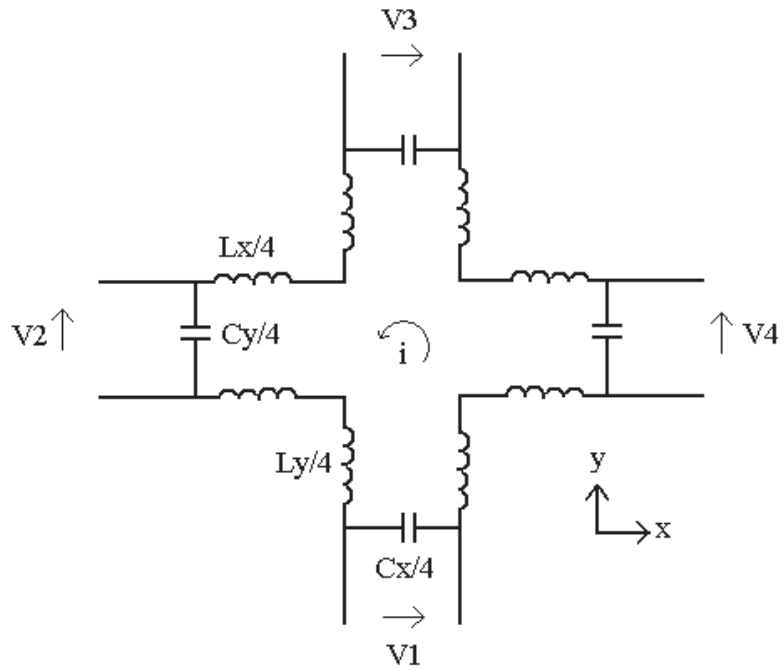


Figure 2.16: The circuit equivalent for the derivation of a transmission line in 2D.

the expansion functions should be chosen such that they are linearly independent and that a superposition of all the expansion functions approximate f reasonable well. The weighting functions should also be linearly independent and chosen so that the products $\langle w_n, g \rangle$ depend on relatively independent properties of g . Other factors that affect the choice of the expansion functions and weighting functions are the desired accuracy of the solution, the ease with which the matrix elements are to be evaluated, the size of the matrix that can be inverted and the realization of a well-conditioned matrix $[L]$.

2.9 Radio Frequency Circuit Theory

The use of RF circuit theory is essential when constructing RF coils and antennas, as such circuits are often needed to ensure good matching between the various components of the RF system and for decoupling the elements within a coil. Much of the information presented in this section originates from Ludwig and Bogdanov [37].

2.9.1 Quality Factor

Quality factor, usually denoted Q , is an inverse measure of the bandwidth of a coil or element and is defined as the resonant frequency divided by the full-width at half-maximum,

$$Q = \frac{f_0}{\Delta f}. \quad (2.80)$$

A high quality factor indicates a low bandwidth and *vice versa*. A high quality factor is necessary to isolate off-resonance signals and hence have good resolution. Although a good quality factor may be achieved on the bench, quality factor almost always drops when the coil is loaded for imaging as the coil and sample begin to couple together. This coupling dissipates energy from the coil into the sample and lowers the quality factor.

2.9.2 Smith Charts

The Smith chart is a convenient way to visually represent impedances and admittances in a single figure. It can be used to analyze and design

RF circuits since the behavior of the circuit as more components are added can be clearly seen.

To establish exactly what a Smith chart is, we begin with the reflection coefficient Γ , which is defined as the ratio of reflected voltage wave to incident voltage wave at a certain fixed location along a transmission line. Where a load connects to a transmission line ($d = 0$), the reflection coefficient Γ_0 describes the mismatch in impedance between the load (Z_L) and the transmission line's characteristic impedance (Z_0). As we move away from the load and d increases we must multiply Γ_0 by the exponential factor $\exp(-j2\beta d)$ to obtain the reflection coefficient at point d . The transformation from Γ_0 to $\Gamma(d)$ is a key ingredient in the construction of the Smith chart.

We now express the reflection coefficient in complex notation:

$$\Gamma_0 = \frac{Z_L - Z_0}{Z_L + Z_0} = \Gamma_{0r} + j\Gamma_{0i} = |\Gamma_0| \exp^{j\theta_L} \quad (2.81)$$

where $\theta_L = \text{atan2}(\Gamma_{0i}, \Gamma_{0r})$.

The input impedance is given by the expression

$$Z_{in}(d) = Z_0 \frac{1 + \Gamma(d)}{1 - \Gamma(d)}. \quad (2.82)$$

Substituting the reflection coefficient

$$\Gamma(d) = |\Gamma_0| \exp^{j\theta_L} \exp^{-j2\beta d} = \Gamma_r + j\Gamma_i \quad (2.83)$$

into this equation for general input impedance results in

$$Z_{in}(d) = Z_0 \frac{1 + \Gamma_r + j\Gamma_i}{1 - \Gamma_r - j\Gamma_i}. \quad (2.84)$$

By normalizing equation 2.84 with respect to the characteristic line impedance we can generalise all of our subsequent derivations.

$$\frac{Z_{in}(d)}{Z_0} = z_{in} = r + jx = \frac{1 + \Gamma(d)}{1 - \Gamma(d)} = \frac{1 + \Gamma_r + j\Gamma_i}{1 - \Gamma_r - j\Gamma_i} \quad (2.85)$$

Multiplying numerator and denominator of equation 2.84 by the complex conjugate of the denominator isolates the real and imaginary parts of z_{in} in terms of the reflection coefficient.

$$z_{in} = r + jx = \frac{1 - \Gamma_r^2 - \Gamma_i^2 + 2j\Gamma_i}{(1 - \Gamma_r)^2 + \Gamma_i^2} \quad (2.86)$$

is now separated into

$$r = \frac{1 - \Gamma_r^2 - \Gamma_i^2}{(1 - \Gamma_r)^2 + \Gamma_i^2} \quad (2.87)$$

and

$$x = \frac{2\Gamma_i}{(1 - \Gamma_r)^2 + \Gamma_i^2}. \quad (2.88)$$

Equations 2.87 and 2.88 are transformation rules for finding z_{in} if the reflection coefficient is specified in terms of Γ_r and Γ_i . They allow us to map from the Γ -plane to the z_{in} -plane. In order to draw a Smith chart we must do the opposite, i.e. map from the z_{in} -plane to the Γ -plane. This can be achieved by inverting equations 2.87 and 2.88.

Inverting 2.87:

$$r[(1 - \Gamma_r)^2 + \Gamma_i^2] = 1 - \Gamma_r^2 - \Gamma_i^2 \quad (2.89)$$

$$\Gamma_r^2(r + 1) - 2r\Gamma_r + \Gamma_i^2(r + 1) = 1 - r \quad (2.90)$$

$$\Gamma_r^2 - \frac{2r}{r + 1}\Gamma_r + \Gamma_i^2 = \frac{1 - r}{r + 1} \quad (2.91)$$

We now progress by completing the square.

$$\left(\Gamma_r - \frac{r}{r + 1}\right)^2 - \frac{r^2}{(r + 1)^2} + \Gamma_i^2 = \frac{1 - r}{r + 1} \quad (2.92)$$

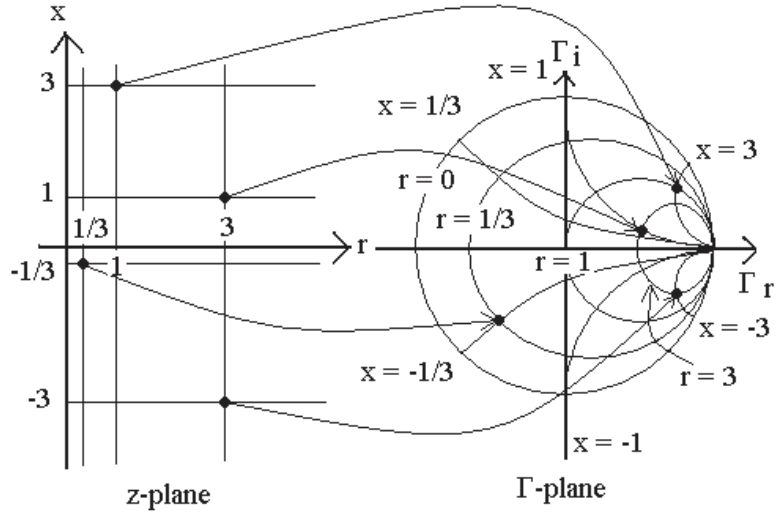


Figure 2.17: Mapping from xr space onto a Smith chart.

$$\left(\Gamma_r - \frac{r}{r+1}\right)^2 + \Gamma_i^2 = \left(\frac{1}{r+1}\right)^2 \quad (2.93)$$

Similarly we can invert equation 2.88 to get

$$(\Gamma_r - 1)^2 + \left(\Gamma_i - \frac{1}{x}\right)^2 = \left(\frac{1}{x}\right)^2. \quad (2.94)$$

Equations 2.93 and 2.94 are equations of circles in the complex Γ -plane that can be written in the generic form $(\Gamma_r - a)^2 + (\Gamma_i - b)^2 = c^2$, where a and b denote the center of the circle and c is the radius in the complex Γ -plane. Plotting impedances using these circles forms a Smith chart. The centre of the Smith chart usually corresponds to the 50Ω (matched) point. The far left of the Smith chart is zero impedance (closed) and the far right is infinite impedance (open).

2.9.3 Matching

A matching circuit can be defined as a circuit which transforms one source or load impedance to another over a given frequency range.

They are therefore used to minimise power loss when driving a coil or antenna. By minimizing the power lost it is possible to ensure more power is delivered from the amplifier to the FoX of transmitter coils, thus reducing the amount of power required to achieve a given B_1 , and also increase the amount of power reaching the detector from receiver coils, thus increasing SNR.

The most intuitive way to design any matching circuit is to use a Smith chart, as the procedure is the same regardless of the number of components in the circuit and the individual effects of adding each component can be seen directly on the Smith chart. Using the following rules the behavior of a matching circuit can be predicted and hence a suitable matching circuit can be designed.

1. Adding a reactive component in series results in motion along a constant-resistance circle.
2. Adding a reactive component as a shunt connection results in motion along a constant-conductance circle.
3. Inductors rotate the impedance toward the upper half of the Smith chart.
4. Capacitors rotate the impedance toward the lower half of the Smith chart.

These rules are summarised in Figure 2.18.

It is possible to consider matching circuits as resonant circuits characterised by a loaded quality factor, Q_L , which is equal to the ratio of

the resonance frequency and the 3 dB bandwidth,

$$Q_L = \frac{f_0}{BW}. \quad (2.95)$$

(Note that neither the loaded quality factor, nor the nodal quality factor mentioned below, are actual physical quality factors associated with a particular piece of equipment, such as a probe. They are simply convenient concepts to use when comparing different circuits on a Smith Chart.) The bandwidth can be approximated by converting the matching circuit into an equivalent bandpass filter and then measuring its bandwidth as normal, however this can be a very complicated approach to take. A more commonly used method is to use the nodal quality factor Q_n . When observing a matching circuit on a Smith chart, each node has an impedance which can be expressed in terms of an equivalent series impedance $Z_S = R_S + jX_S$ or admittance $Y_P = G_P + jB_P$. We can therefore find Q_n as the ratio of the absolute value of the reactance X_S to the corresponding resistance R_S ,

$$Q_n = \frac{|X_S|}{R_S}, \quad (2.96)$$

or as the ratio of the absolute value of susceptance B_P to the conductance G_P ,

$$Q_n = \frac{|B_P|}{G_P}. \quad (2.97)$$

The loaded quality factor is usually estimated as the maximum nodal quality factor. This does not yield a very accurate value of the bandwidth, but it does allow us to compare matching circuits to each other in terms of relative bandwidth. It is also possible to draw constant Q_n contours directly onto a Smith chart, as shown in Figure 2.19.

The simplest form of matching circuit is the two-component network, also known as the L-circuit due to the arrangement of its components. Two reactive components are used to transform a load impedance Z_L into the desired input impedance Z_{in} . One component is in series and the other is parallel. L-circuits are the easiest and cheapest to produce, but they grant no control over the quality factor of the circuit. For any given load and input impedances there are at least two possible L-circuits that can accomplish the required match. Some possibilities will be high-pass filters, while others may be low-pass or bandpass filters.

In order to gain control over the quality factor of the matching circuit it is necessary to add a third component. Three-component matching circuits are either T- or Pi-circuits, depending upon where the third component goes. T-circuits are narrowband and Pi-circuits are broadband. As we are only concerned with a single, well defined frequency in MRI, high nodal quality factor T-circuits are best used for our matching needs. To design such a circuit to match our coil or antenna of impedance Z_L to our input impedance Z_{in} we need to perform the following steps.

1. Plot Z_L and Z_{in} on a Smith chart.
2. Starting at Z_L add a series component and follow a constant-resistance circle until a desired nodal quality factor is achieved.
3. Now add a shunt component to move the inductance along a constant-conductance circle until the $r = 1$ constant-resistance circle is reached.

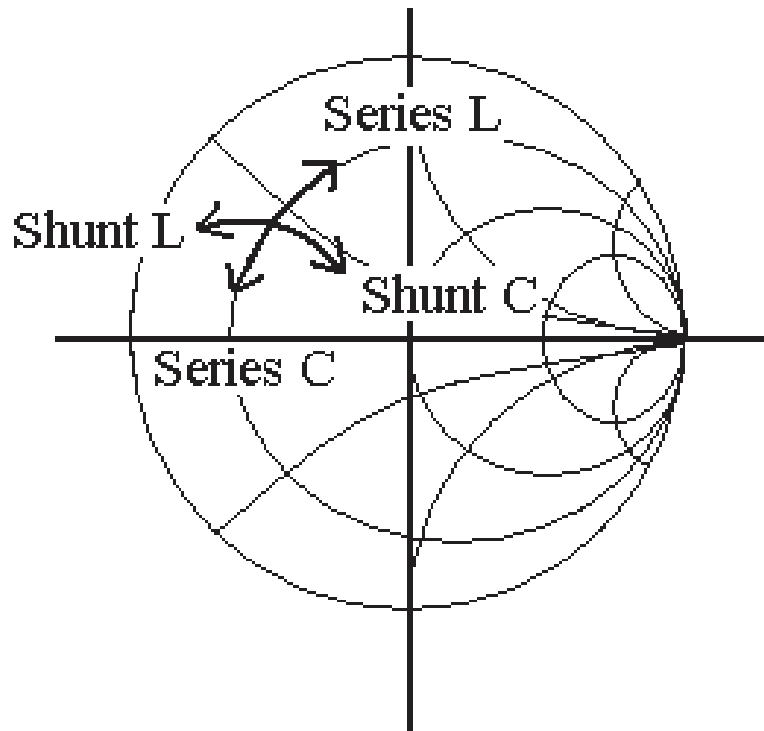


Figure 2.18: Moving around the Smith chart.

4. The final component is added so that the inductance follows the $r = 1$ constant-resistance circle until it reaches Z_{in} .

All that remains now is to calculate the actual values of the components. For each given component we calculate either the change in admittance b if it is a shunt component or the change in reactance x if it is a series component. We then use these changes to calculate the component values using the equations given in table 2.1.

2.9.4 Coupling

When a transmission element is driven by an EM waveform in proximity to a second element, the second element receives the EM signal emit-

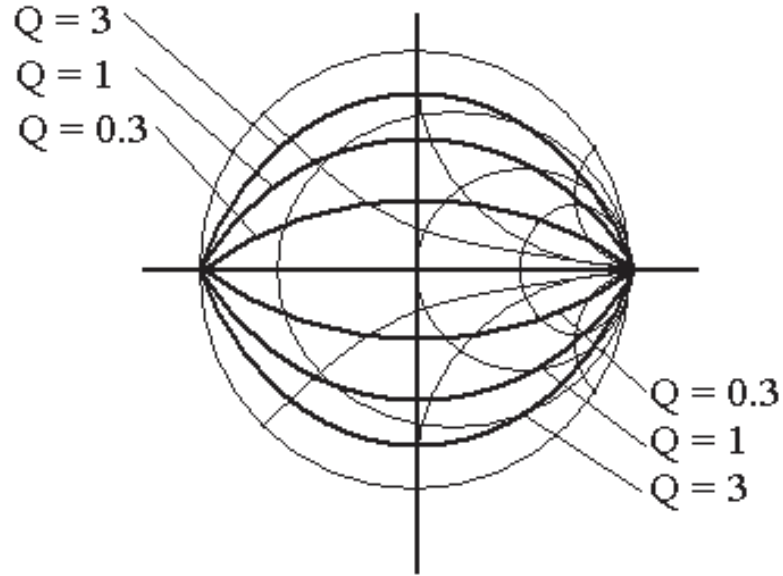


Figure 2.19: Lines of constant nodal quality factor.

ted by the driven element, becomes excited, and then begins emitting its own signal. This process is known as coupling. It can be particularly strong when making transmit-SENSE coils as each element will be tuned and matched to the same frequency, thus making each element a good receiver to EM radiation emitted by any of the other elements. This coupling can be very disruptive as it interferes with the control of the EM radiation being produced by each transmission element.

Coupling between elements can be observed as a splitting of the resonance peak of each element. This splitting can then be used to quantify coupling by calculating the coupling constant K ,

$$\pm K = \frac{f_0^2}{f_{1,2}^2} - 1, \quad (2.98)$$

where f_0 is the resonant frequency before coupling occurred and $f_{1,2}^2$ is the frequency of either the first or second new peak. The plus/minus is

	Capacitor	Inductor
Shunt	$C = \frac{b_C}{\omega Z_0}$	$L = -\frac{Z_0}{b_L \omega}$
Series	$C = -\frac{1}{x_C \omega Z_0}$	$L = \frac{x_L Z_0}{\omega}$

Table 2.1: Equations for determining component values from a Smith chart.

there to ensure K is always positive. Thus a coupling is characterised by two K values between zero (no coupling) and one (very strong coupling). If the two K values are similar in value then the coupling is weak, and if they are very different in value the coupling is strong. It is also possible to take an average of the two K values to allow for easy comparison between different coupled systems.

2.9.5 Decoupling Theory

Before a transmit-SENSE coil can be used, all of its elements must be decoupled. Coupled elements in a transmit-SENSE coil will interfere with each other and therefore make it difficult to drive each element independently of the others. There are several effective methods of decoupling. Passive methods involve connecting the elements together with capacitors or inductors so that the coupling between any two elements is negated by the signal that passes through the capacitor or inductor. Active methods involve using complex circuits to modify the signals being fed into the transmission elements. The mathematical description of coupling can be formulated in any of three ways. The method used in this research project is based upon the impedance ma-

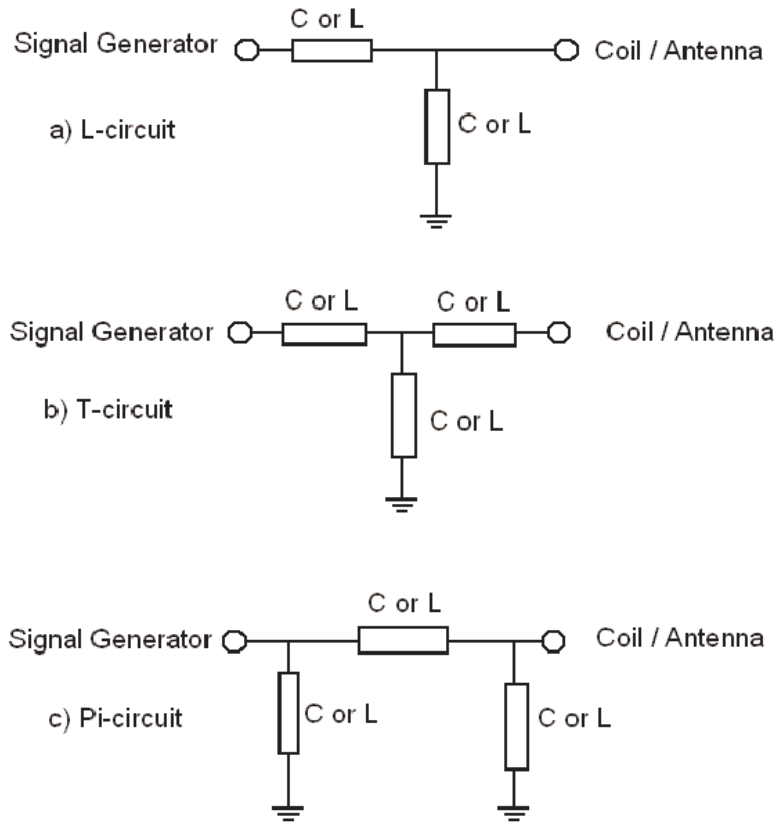


Figure 2.20: a) An L-circuit, b) a T-circuit, and c) a Pi-circuit.

trix Z . The second method is based upon the admittance matrix Y (essentially the inverse of Z), and the third method uses hybrid parameter matrices [38].

A transmit-SENSE coil consisting of n -elements can be treated as a n -port network system, which in turn can be characterised by its open-circuit impedance matrix. The self- and mutual-impedances of the network can either be theoretically calculated or experimentally derived [39]. Let V and I be the vectors of the voltages and currents measured at the networks ports (see Figure 2.21). Z is the open-circuit

impedance matrix of the n -port system.

$$V = \begin{pmatrix} V_1 \\ \vdots \\ V_n \end{pmatrix}, I = \begin{pmatrix} I_1 \\ \vdots \\ I_n \end{pmatrix}, Z = \begin{pmatrix} Z_{11} & \cdots & Z_{1n} \\ \vdots & \ddots & \vdots \\ Z_{n1} & \cdots & Z_{nn} \end{pmatrix}. \quad (2.99)$$

The diagonal elements of Z are the self-impedances of the elements (i.e. Z_{ii} is the self impedance of the i^{th} element) when all other ports are open-circuited. All other components of Z are the mutual impedances between the i^{th} and j^{th} elements. The equation of the n -port system is

$$V = ZI. \quad (2.100)$$

The uncoupled system can be thought of as a special case of the coupled system (when all mutual coupling components of Z have gone to zero). Let V^u and I^u be the voltage and currents of the uncoupled system, while Z^u is the uncoupled system's impedance matrix.

$$V^u = \begin{pmatrix} V_1^u \\ \vdots \\ V_n^u \end{pmatrix}, I^u = \begin{pmatrix} I_1^u \\ \vdots \\ I_n^u \end{pmatrix}, Z^u = \begin{pmatrix} Z_{11}^u & 0 & \cdots & 0 \\ 0 & Z_{22}^u & \cdots & 0 \\ \vdots & & \ddots & \vdots \\ 0 & 0 & \cdots & Z_{nn}^u \end{pmatrix}. \quad (2.101)$$

The equation of the uncoupled n -port system is

$$V^u = Z^u I^u. \quad (2.102)$$

If the closed circuit is now considered we have the generator voltages,

$$V^g = \begin{pmatrix} V_1^g \\ V_2^g \\ \vdots \\ V_n^g \end{pmatrix}, \quad (2.103)$$

and the generator impedance is,

$$Z^g = \begin{pmatrix} Z_1^g & 0 & \cdots & 0 \\ 0 & Z_2^g & & 0 \\ \vdots & & \ddots & \vdots \\ 0 & 0 & \cdots & Z_n^g \end{pmatrix}. \quad (2.104)$$

Kirchoff's law can be used to describe the complete coupled system shown in Figure 2.21.

$$V^g = V + Z^g I \quad (2.105)$$

Also, the uncoupled system can be described by

$$V^g = V^u + Z^g I^u. \quad (2.106)$$

Equations 2.100, 2.102, 2.105 and 2.106 can be used to derive a relationship between the coupled and uncoupled systems,

$$V^g = (Z + Z^g) I = (Z^u + Z^g) I^u. \quad (2.107)$$

Now define C_I as the transform matrix from uncoupled currents to coupled currents, and D_I is the transform matrix that takes coupled currents to uncoupled currents (the inverse of C_I). Now equation 2.107 becomes either

$$I = C_I I^u, \text{ or } I^u = D_I I, \quad (2.108)$$

hence,

$$C_I = (Z + Z^g)^{-1} (Z^u + Z^g) \quad (2.109)$$

and

$$D_I = (Z^u + Z^g)^{-1} (Z + Z^g). \quad (2.110)$$

C_I is called the current coupling matrix and D_I is called the current decoupling matrix. The coupling of an n -port system can be fully characterised by the current coupling matrix, where each eigenvalue of C_I represents one coupled mode. Since C_I is an $n \times n$ matrix there will be n coupled modes (assuming no degeneracy), which would cause the system's resonance frequency to split into n different frequencies. A possible way to overcome such degeneracy is introduce decoupling so that the modes degenerate into a single mode.

It is theoretically possible to decouple an n -port array using a $2n$ -port decoupling network which has impedance matrix Z' ,

$$Z' = \begin{pmatrix} Z'_{11} & \cdots & Z'_{1n} & Z'_{1(n+1)} & \cdots & Z'_{1(2n)} \\ \vdots & \ddots & \vdots & \vdots & \ddots & \vdots \\ Z'_{n1} & \cdots & Z'_{nn} & Z'_{n(n+1)} & \cdots & Z'_{n(2n)} \\ Z'_{(n+1)1} & \cdots & Z'_{(n+1)n} & Z'_{(n+1)(n+1)} & \cdots & Z'_{(n+1)(2n)} \\ \vdots & \ddots & \vdots & \vdots & \ddots & \vdots \\ Z'_{(2n)1} & \cdots & Z'_{(2n)n} & Z'_{(2n)(n+1)} & \cdots & Z'_{(2n)(2n)} \end{pmatrix}. \quad (2.111)$$

Z' can be divided into four $n \times n$ submatrices,

$$\hat{Z}'_{11} = \begin{pmatrix} Z'_{11} & \cdots & Z'_{1n} \\ \vdots & \ddots & \vdots \\ Z'_{n1} & \cdots & Z'_{nn} \end{pmatrix}, \quad (2.112)$$

$$\hat{Z}'_{12} = \begin{pmatrix} Z'_{1(n+1)} & \cdots & Z'_{1(2n)} \\ \vdots & \ddots & \vdots \\ Z'_{n(n+1)} & \cdots & Z'_{n(2n)} \end{pmatrix}, \quad (2.113)$$

$$\hat{Z}'_{21} = \begin{pmatrix} Z'_{(n+1)1} & \cdots & Z'_{(n+1)n} \\ \vdots & \ddots & \vdots \\ Z'_{(2n)1} & \cdots & Z'_{(2n)n} \end{pmatrix}, \quad (2.114)$$

$$\hat{Z}'_{22} = \begin{pmatrix} Z'_{(n+1)(n+1)} & \cdots & Z'_{(n+1)(2n)} \\ \vdots & \ddots & \vdots \\ Z'_{(2n)(n+1)} & \cdots & Z'_{(2n)(2n)} \end{pmatrix}. \quad (2.115)$$

The equation of the $2n$ port system is

$$\begin{pmatrix} V' \\ V'' \end{pmatrix} = \begin{pmatrix} \hat{Z}'_{11} & \hat{Z}'_{12} \\ \hat{Z}'_{21} & \hat{Z}'_{22} \end{pmatrix} \begin{pmatrix} I' \\ I'' \end{pmatrix}, \quad (2.116)$$

where

$$V' = \begin{pmatrix} V'_1 \\ \vdots \\ V'_n \end{pmatrix}, \quad V'' = \begin{pmatrix} V'_{n+1} \\ \vdots \\ V'_{2n} \end{pmatrix}, \quad I' = \begin{pmatrix} I'_1 \\ \vdots \\ I'_n \end{pmatrix}, \quad I'' = \begin{pmatrix} I'_{n+1} \\ \vdots \\ I'_{2n} \end{pmatrix}. \quad (2.117)$$

At the interconnections between the n -port system and the $2n$ -port interface,

$$V'' = V, \quad I'' = -I. \quad (2.118)$$

From equations 2.100, 2.116 and 2.118 the output impedance matrix of the interface can be derived:

$$Z_{\text{out}} = \frac{V'}{I'} = \hat{Z}'_{11} - \hat{Z}'_{12} (\hat{Z}'_{22} + Z)^{-1} \hat{Z}'_{21}. \quad (2.119)$$

When the output impedance matrix is equal to the impedance matrix of the uncoupled system, $Z_{\text{out}} = Z^u$, and equation 2.119 becomes the decoupling equation,

$$\hat{Z}'_{11} - \hat{Z}'_{12} (\hat{Z}'_{22} + Z)^{-1} \hat{Z}'_{21} = Z^u. \quad (2.120)$$

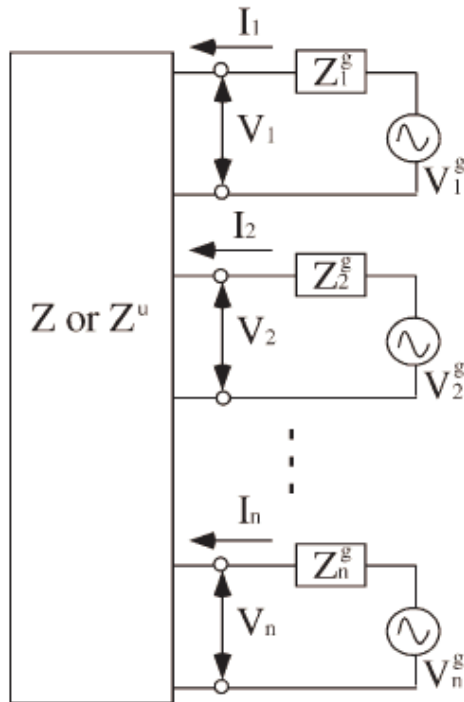


Figure 2.21: n -port network system. The signal generators are represented by voltage sources and the system is represented by the impedance matrix Z if the system is coupled and by Z^u if it is uncoupled. Figure adapted from Lee et al. [38].

In order to decouple any n -port system, a $2n$ -port interface must be constructed that satisfies equation 2.120.

2.9.6 Decoupling by Overlapping Elements and Using Low-Impedance Preamplifiers

It is possible to eliminate nearest-neighbour coupling of elements in an array by overlapping adjacent elements[40], as shown in Figure 2.23. All that remains is a small but significant coupling between next nearest-

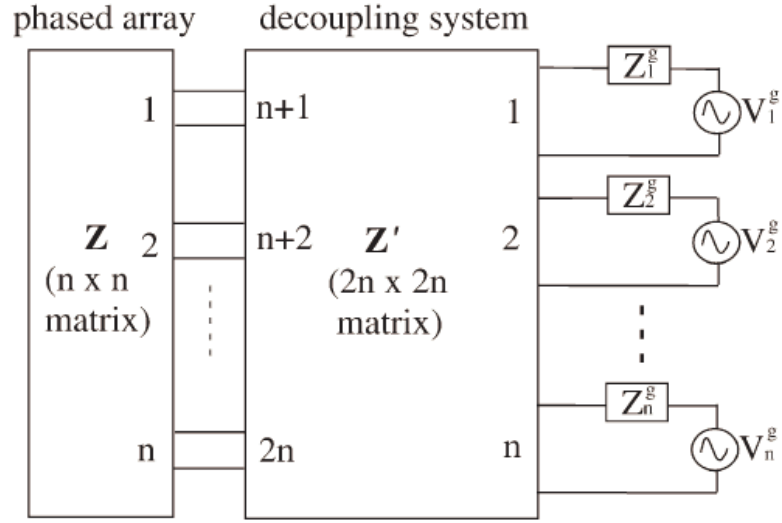


Figure 2.22: $2n$ -port decoupling system used to decouple an n -port array. Figure from Lee et al. [38].

neighbours and farther coils.

To see how this works first treat the two coils as a transformer (see Figure 2.24). Consider coil 1 in isolation and at the resonant frequency. The impedance of the coil as viewed at the preamplifier is

$$Z_b = \frac{X_{C2b}^2}{R_1} + j(X_{L2b} - X_{C2b}). \quad (2.121)$$

In order to transform the series resistance R_1 to 50Ω we must choose X_{C2b} and X_{L2b} such that

$$X_{L2b} = X_{C2b} = \sqrt{50R_1} \equiv X_2. \quad (2.122)$$

Now consider the circuit formed by X_{C2b} , X_{L2b} and the preamplifier; the input impedance of the preamplifier is truly zero, X_{C2b} and X_{L2b} form a parallel resonant circuit which blocks current from flowing in the surface coil even though the coil is receiving and transferring an

NMR signal to the preamplifier. If, during reception, there is very little current flowing in the surface coil, no noise or signal is coupled to other coils and therefore all coils receive independently.

The decoupling performance of using a low impedance preamplifier can be proven by considering the circuit in Figure 2.24 where both coils are independently tuned to the same resonant frequency ($X_L - X_{C2a} - X_{C2b} = 0$ and $X_L - X_{C1} = 0$). If the second coil is removed, the series impedance of the primary loop is given by R_1 . If the second coil is present and connected to a preamplifier of impedance R_P the impedance (as viewed from the terminals of the primary coil) is given by

$$Z_A = R_1 + \frac{\omega^2 L^2 k^2}{R_1 + \left(\frac{X_2^2}{R_P}\right)}. \quad (2.123)$$

If either the mutual inductance coupling constant k or R_P are zero, the resulting noise resistance is R_1 , the same as for a single isolated coil. Similarly, the amount of signal transferred between coils can be evaluated by looking at the open circuit voltage as viewed at terminal A, which is

$$V_A = V_1 - V_2 \frac{j\omega Lk}{R_1 + \left(\frac{X_2^2}{R_P}\right)}. \quad (2.124)$$

If either k or R_p are zero, we obtain the NMR signal of the isolated coil.

It should be noted that although the preamplifier is low impedance, it is still optimised for low noise at 50Ω since the coils themselves are still the equivalent of 50Ω loads.

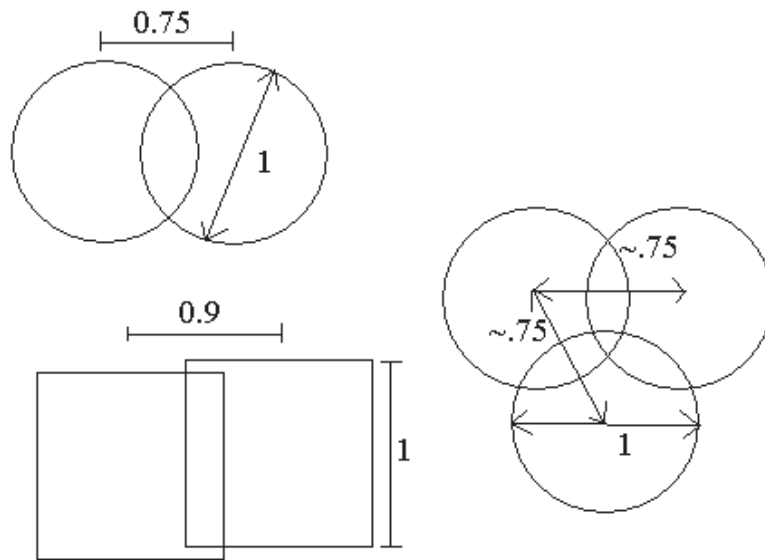


Figure 2.23: Overlapping immediately adjacent coils can reduce coupling. The exact overlap depends on coil details and is determined empirically.

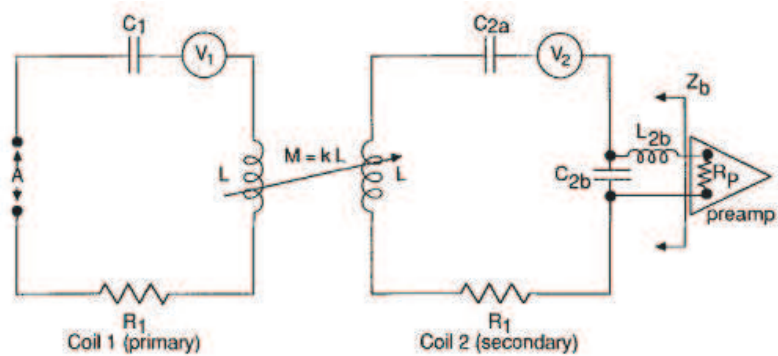


Figure 2.24: Interacting surface coils represented as a transformer.[40].

2.10 Travelling-wave Magnetic Resonance Imaging

TW MRI is a relatively new variant of MRI, proposed by Brunner et al. [3]. In this method, the transmission coil is replaced by an antenna either outside or at the end of the magnet bore. This antenna then generates a transverse EM TW which passes through the bore and excites the spins in the object being imaged. This is contrary to the traditional method of exciting the spins, which uses an element placed within the bore and close to the object to create a near field, non-travelling wave [41]. Using a TW, which has a perfectly uniform magnitude at any wavelength, allows much greater homogeneity than is achievable using a contemporary transmit coil.

The TW is guided through the bore using a waveguide. With a 58 cm diameter waveguide, corresponding to the RF screen already built into the Philips seven tesla magnet, an unloaded lower cut-off frequency for the transverse electric mode of 303 MHz is achieved. Fortunately, by placing sufficient dielectric within the waveguide, such as containers of water or a human body, it is possible to lower this cut-off frequency down to 298 MHz, the frequency necessary for exciting protons at seven tesla. TW MRI is thus well suited to use at seven tesla for two reasons. Firstly, because it only works with a sufficiently strong magnetic field. And secondly, because it provides more uniform coverage of objects of similar size to the RF wavelength, which improves B_1 homogeneity; a particular problem at high field.

When working with TW MRI it is necessary to consider the polarisation of the TW as it travels down the bore, as well as the polarisation of the returning TW that the antenna detects. Most TW antenna designs have a preferred polarisation, and if this preferred polarisation does not match the polarisation of the spins the result will be a significant SNR drop. Fortunately the polarisation of the signal returning from the spins always matches the polarisation of the transmitted wave from the antenna, so if this polarisation is correct a good SNR is obtained, whereas if it is incorrect a very low SNR is obtained. An antenna that works well when transmitting in the foot-head direction will need to have its polarity reversed when used in the head-foot direction, and *vice versa*.

TW MRI promises several benefits to imaging at seven tesla. The removal of the transmit coil from within the bore frees up space within the magnet, allowing patients to feel more comfortable or providing more room for stimulus equipment. The imaging volume is no longer limited by the volume within the transmit coil. Brunner et al. [3] were able to image 50 cm of a human leg with very good homogeneity, the only limiting factor to the geometry of the image being the range of the gradient coils. This may improve studies where small animals or objects can be imaged in parallel. Using a TW also prevents the probe from being loaded by losses in the sample, should be more robust than using a transmit coil, and avoids exposure to strong, short range electric fields emanating from the transmit coil.

Possible problems associated with a TW approach include the cut-

off frequency already mentioned. Signal attenuation through the bore will impair imaging, particularly in tall and/or larger subjects. Some means of absorbing the TW is required at the far end of the bore, and there is a phase delay resulting from the signal propagation which must be accounted for. Pronounced dielectric interfaces (such as the shoulders) are also expected to cause significant imaging artifacts. The relatively long distance between the antenna and the resonant nuclei being imaged can lead to a phase delay. This could become a significant problem for larger samples, where different parts of the sample will have very different phase delays. If the same antenna is used for both transmission and reception, the phase delay will be linear. This will not be a problem in imaging, but in spectroscopy delay-related dephasing could be. This problem can be overcome by using two antennas, one for transmission and one for reception, designed and placed in such a way that the total phase is the same across the volume of interest.

2.11 Reciprocity

The principal of reciprocity states that the current \mathbf{J}_1 induced in antenna 1 as a result of the electric field \mathbf{E}_2 generated by antenna 2, is the same as the current \mathbf{J}_2 induced in antenna 2 as a result of the electric field \mathbf{E}_1 generated by antenna 1. This can be expressed mathematically as

$$\int (\mathbf{E}_1 \cdot \mathbf{J}_1) dv_1 = \int (\mathbf{E}_2 \cdot \mathbf{J}_2) dv_2. \quad (2.125)$$

It should be noted that reciprocity does not hold in the case of TW MRI. Only one antenna is in use, and the second body has a magnetisation and relative permittivity which must be taken into account. We first start from Maxwell's equations, giving each body both a magnetisation and a relative permittivity (see Figure 2.25). In this case we can write the following for Maxwell's equations:

$$\nabla \times \mathbf{E}_1 = -\frac{\partial \mathbf{B}_1}{\partial t} = -j\omega (\mathbf{B}_1 - \mu_0 \mathbf{M}_1) \quad (2.126)$$

$$\nabla \times \mathbf{E}_2 = -\frac{\partial \mathbf{B}_2}{\partial t} = -j\omega (\mathbf{B}_2 - \mu_0 \mathbf{M}_2) \quad (2.127)$$

$$\nabla \times \mathbf{B}_1 = \mu_0 \mathbf{J}_1 + \mu_0 \epsilon_0 \epsilon_1 \frac{\partial \mathbf{E}_1}{\partial t} = \mu_0 \mathbf{J}_1 + j\omega \mu_0 \epsilon_0 \epsilon_1 \mathbf{E}_1 \quad (2.128)$$

$$\nabla \times \mathbf{B}_2 = \mu_0 \mathbf{J}_2 + \mu_0 \epsilon_0 \epsilon_1 \frac{\partial \mathbf{E}_2}{\partial t} = \mu_0 \mathbf{J}_2 + j\omega \mu_0 \epsilon_0 \epsilon_2 \mathbf{E}_2 \quad (2.129)$$

We then take the dot products of equations 2.127 and 2.129 with \mathbf{B}_1 and \mathbf{E}_1 respectively.

$$\mathbf{B}_1 \cdot (\nabla \times \mathbf{E}_2) = -j\omega \mathbf{B}_1 \cdot \mathbf{B}_2 + j\omega \mu_0 \mathbf{B}_1 \cdot \mathbf{M}_2 \quad (2.130)$$

$$\mathbf{E}_1 \cdot (\nabla \times \mathbf{B}_2) = \mu_0 \mathbf{E}_1 \cdot \mathbf{J}_2 + j\omega \epsilon_0 \epsilon_1 \mathbf{E}_1 \cdot \mathbf{E}_2 \quad (2.131)$$

Now subtract equation 2.130 from equation 2.131.

$$\begin{aligned}
\mathbf{E}_1 \cdot (\nabla \times \mathbf{B}_2) - \mathbf{B}_1 \cdot (\nabla \times \mathbf{E}_2) &= \nabla \cdot (\mathbf{E}_1 \times \mathbf{B}_2) & (2.132) \\
&= \mu_0 \mathbf{E}_1 \cdot \mathbf{J}_2 + j\omega\epsilon_0\epsilon_1\mu_0 \mathbf{E}_1 \cdot \mathbf{E}_2 \\
&\quad + j\omega \mathbf{B}_1 \cdot \mathbf{B}_2 - j\omega\mu_0 \mathbf{B}_1 \cdot \mathbf{M}_2
\end{aligned}$$

Similarly, taking the dot products of equations 2.126 and 2.128 with \mathbf{B}_2 and \mathbf{E}_2 , we obtain

$$\begin{aligned}
\mathbf{E}_2 \cdot (\nabla \times \mathbf{B}_1) - \mathbf{B}_2 \cdot (\nabla \times \mathbf{E}_1) &= \nabla \cdot (\mathbf{E}_2 \times \mathbf{B}_1) & (2.133) \\
&= \mu_0 \mathbf{E}_2 \cdot \mathbf{J}_1 + j\omega\epsilon_0\epsilon_2\mu_0 \mathbf{E}_2 \cdot \mathbf{E}_1 \\
&\quad + j\omega \mathbf{B}_2 \cdot \mathbf{B}_1 - j\omega\mu_0 \mathbf{B}_2 \cdot \mathbf{M}_1.
\end{aligned}$$

Subtract equation 2.133 from equation 2.132.

$$\begin{aligned}
\nabla \cdot (\mathbf{E}_1 \times \mathbf{B}_2) - \nabla \cdot (\mathbf{E}_2 \times \mathbf{B}_1) &= \mu_0 (\mathbf{E}_1 \cdot \mathbf{J}_2 - \mathbf{E}_2 \cdot \mathbf{J}_1) & (2.134) \\
&\quad + j\omega\epsilon_0\mu_0 (\epsilon_1 - \epsilon_2) \mathbf{E}_1 \cdot \mathbf{E}_2 \\
&\quad + j\omega\mu_0 (\mathbf{B}_2 \cdot \mathbf{M}_1 - \mathbf{B}_1 \cdot \mathbf{M}_2)
\end{aligned}$$

This is then integrated over a volume enclosing the sources. Using the divergence theorem it can be shown that:

$$\begin{aligned}
&\int \mu_0 (\mathbf{E}_1 \cdot \mathbf{J}_2 - \mathbf{E}_2 \cdot \mathbf{J}_1) + j\omega\epsilon_0\mu_0 \mathbf{E}_1 \cdot \mathbf{E}_2 (\epsilon_1 - \epsilon_2) \\
&\quad + j\omega\mu_0 (\mathbf{B}_2 \cdot \mathbf{M}_1 - \mathbf{B}_1 \cdot \mathbf{M}_2) dv \\
&= \int \nabla \cdot (\mathbf{E}_1 \times \mathbf{B}_2) - \nabla \cdot (\mathbf{E}_2 \times \mathbf{B}_1) dv \\
&= \int \nabla \cdot (\mathbf{E}_1 \times \mathbf{B}_2 - \mathbf{E}_2 \times \mathbf{B}_1) dv \\
&= \oint (\mathbf{E}_1 \times \mathbf{B}_2 - \mathbf{E}_2 \times \mathbf{B}_1) \cdot d\mathbf{S} & (2.135)
\end{aligned}$$

We can now take the surface to be a sphere of large radius R . We also define \mathbf{a} as the unit radial vector, and note that \mathbf{E}_1 and \mathbf{E}_2 are

both perpendicular to \mathbf{a} . We can therefore state that

$$\mathbf{H}_1 = \frac{\mathbf{B}_1}{\mu_0} - \mathbf{M}_1 = \sqrt{\frac{\epsilon_0 \epsilon_1}{\mu_0}} (\mathbf{a} \times \mathbf{E}_1) \quad (2.136)$$

and therefore

$$\mathbf{B}_1 = \sqrt{\epsilon_0 \epsilon_1 \mu_0} (\mathbf{a} \times \mathbf{E}_1) + \mathbf{M}_1, \quad (2.137)$$

and similarly

$$\mathbf{B}_2 = \sqrt{\epsilon_0 \epsilon_2 \mu_0} (\mathbf{a} \times \mathbf{E}_2) + \mathbf{M}_2. \quad (2.138)$$

Now substitute equation 2.137 and equation 2.138 into $\mathbf{E}_1 \times \mathbf{B}_2$ and $\mathbf{E}_2 \times \mathbf{B}_1$.

$$\begin{aligned} \mathbf{E}_1 \times \mathbf{B}_2 &= \mathbf{E}_1 (\sqrt{\epsilon_0 \epsilon_2 \mu_0} (\mathbf{a} \times \mathbf{E}_2) + \mathbf{M}_2) \\ &= \sqrt{\epsilon_0 \epsilon_2 \epsilon_0} (\mathbf{a} (\mathbf{E}_1 \times \mathbf{E}_2) - \mathbf{E}_2 (\mathbf{E}_1 \times \mathbf{a})) + \mathbf{E}_1 \times \mathbf{M}_2 \end{aligned} \quad (2.139)$$

and

$$\begin{aligned} \mathbf{E}_2 \times \mathbf{B}_1 &= \mathbf{E}_2 (\sqrt{\epsilon_0 \epsilon_1 \mu_0} (\mathbf{a} \times \mathbf{E}_1) + \mathbf{M}_1) \\ &= \sqrt{\epsilon_0 \epsilon_1 \epsilon_0} (\mathbf{a} (\mathbf{E}_2 \times \mathbf{E}_1) - \mathbf{E}_1 (\mathbf{E}_2 \times \mathbf{a})) + \mathbf{E}_2 \times \mathbf{M}_1 \end{aligned} \quad (2.140)$$

and we therefore find that $\mathbf{E}_1 \times \mathbf{B}_2 \neq \mathbf{E}_2 \times \mathbf{B}_1$. If we were considering two antennas, i.e. $\mathbf{M}_1 = \mathbf{M}_2 = 0$ and $\epsilon_1 = \epsilon_2 = 0$, and therefore $\mathbf{E}_1 \times \mathbf{B}_2 = \mathbf{E}_2 \times \mathbf{B}_1$. This would make equation 2.135 simplify as follows;

$$\int (\mathbf{E}_1 \cdot \mathbf{J}_2 - \mathbf{E}_2 \cdot \mathbf{J}_1) dv = \oint (\mathbf{E}_1 \times \mathbf{B}_2 - \mathbf{E}_2 \times \mathbf{B}_1) \cdot d\mathbf{S} = 0 \quad (2.141)$$

and therefore we obtain the reciprocity condition, equation 2.125.

If, as in our case, we have introduced magnetisation and relative permittivity into either body, this final step is not possible and therefore reciprocity does not hold true.

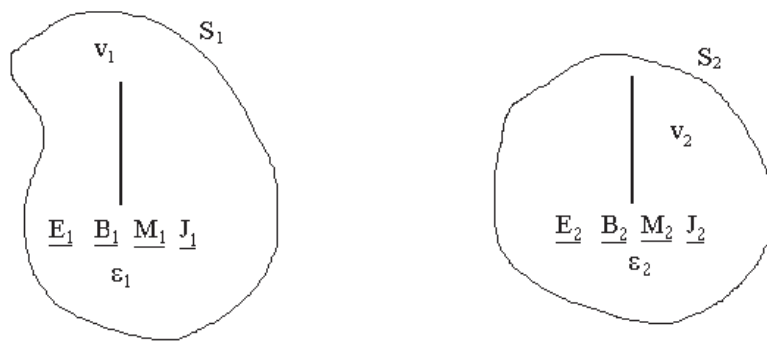


Figure 2.25: The two bodies in the reciprocity derivation.

Chapter 3

Literature Survey

3.1 Radio Frequency Shimming

In 2001 Ibrahim et al. [42] demonstrated the potential benefits of RF shimming. In this paper they simulated driving a 24 element coil with various different phases and magnitudes in each element and observed the B_1 homogeneity achieved in a human head model. They also then verified their simulation results with an actual MRI experiment.

Mao et al. [43] explored the limits of RF shimming by performing a wide range of numerical simulations. They investigated between 16 and 80 element coils as well as differing imaging volumes and the frequency dependence of RF shimming. They were able to conclude that RF shimming is more effective when a coil has more elements, when employed at lower frequencies, and over smaller imaging volumes.

A paper by Vaughan et al. [44] describes in great detail the first 9.4 tesla human MRI system. They also describe their attempts at using RF shimming for human head imaging. In this paper they only varied

the phase of the RF waveform in each element while the magnitude was kept constant. They manually varied the phases after each scan (having started with a 45^0 phase shift between elements), reporting that after four iterations good B_1 homogeneity is achieved. Each iteration took approximately one minute to implement.

3.2 Transmit Sensitivity Encoding

In 1990 Roemer et al. [40] published a paper which first proposed using multiple elements to detect an NMR signal. The original idea was to obtain the good SNR of a small surface coil but to also cover a large volume. This formed an important first step towards developing SENSE. The paper itself provides a good description of decoupling coils by overlapping neighbouring loops, and of low impedance preamplifier decoupling.

The theoretical procedure of SENSE was first published in 1999 by Pruessmann et al. [29]. This paper details the mathematics of SENSE reconstruction, and also demonstrates the idea with some phantom images.

The first paper to propose the concept of transmit-SENSE was published in 2003 by Katscher et al. [2]. In this paper Katscher demonstrates mathematically how the excitation patterns and sensitivity profiles of multiple coils combine linearly, thus making transmit-SENSE feasible. He then goes on to verify his proof experimentally by performing two sub-experiments. In each experiment a single coil is used to image a phantom, and then after both experiments had been per-

formed their images were combined to obtain a full image. This was necessary as the hardware required for simultaneous transmission from multiple coils was not yet available.

Lin et al. [45] have built a birdcage coil for transmit-SENSE on the human head. This coil is only capable of $R=2$, which is not particularly high (though anything above $R=1$ provides some benefit). Lin's paper briefly describes the construction of the coil and also shows some brain images taken with the coil. Little mathematics or detailed analysis of the coils performance is given.

In 2004 Katscher et al. published a second paper [46]. This paper details the mathematical proof of transmit-SENSE again, and also presents the results of numerical simulations which confirm the feasibility of transmit-SENSE. These were simulations of two transmit coils, with sensitivity profiles measured from a volunteer and with some desired 2D pulse profiles. In one study, each coil has a pulse profile which covers columns of k-space. The first coil covers every first column and the second coil covers every second column. In the second study spiral k-space trajectories are used. Both studies were able to reconstruct the desired final image when the images taken by each coil were combined, thus providing more evidence that transmit-SENSE was feasible.

An early paper to detail the development of a transmit-SENSE coil for use at seven tesla is Adriany et al. [47]. Adriany describes the design of both a four-element and an eight-element coil. Having described the designs, Adriany then goes on to study the performance of both coils in great detail. The decoupling of the individual transmission elements

is investigated, as well as B_1 homogeneity and SNR. This paper provides a good overview of the steps that are necessary when designing a transmit-SENSE coil, and also describes the various measurements and tests that should be made once the coil has been built that allow the coil's performance to be analyzed.

Another paper published in 2006 [48] reported on simulations into the impact of different geometries on RF pulse performance. The findings of the paper were that RF pulse performance was stable, and thus transmit-SENSE coils can be designed with a wide selection of geometries. The paper also provides a brief summary of the progress made in developing true transmit-SENSE systems. Both an eight and a three channel system are mentioned. These systems were reported to have achieved reduction factors of between $R = 2$ and $R = 4$, while accuracy was kept above 90%.

Pinkerton et al. [33] details the design of another transmit-SENSE coil, this time for use at four tesla. This paper uses FDTD simulations to predict the coil's properties. Pinkerton also proposes a new parameter, E , which can be used to quantify the performance of a transmit-SENSE coil. This parameter incorporates the signal intensity, as well as physiological and intrinsic noise, thus allowing it to be used to optimise transmit-SENSE coil design.

A very good comparison between parallel imaging and parallel transmission (i.e. transmit-SENSE) can be found in Katscher and Bornert's 2007 paper [31]. This paper details the basic theory of both procedures, as well as providing a detailed comparison between the two at

the end of the paper. The potential benefits of transmit-SENSE on the SNR and specific absorption rate (SAR) are also mentioned. Possible applications of transmit-SENSE are also listed. These included compensation of patient induced RF inhomogeneities, volume-selective excitation, and curved-slice imaging.

In 2007 Alagappan et al. [49] published a paper regarding the adaptation of the birdcage coil design for use in transmit-SENSE. This paper provides a good description of the process required to decouple the eight individual transmission elements. This paper also investigates the different possible excitation modes of the birdcage coil. The resulting extra degree of freedom from the use of these modes is shown to increase the overall flexibility of the transmit-SENSE system. Alagappan describes the pulse design process in this paper, which should prove useful once the pulse design phase of this research project is reached.

The development of a transceive coil for use with SENSE at three tesla is detailed in Vernickel et al. [50]. This paper serves as a very good introduction to decoupling, as it briefly describes the basic types of decoupling methods. This paper also has a section on Π -networks (circuits which can be analogous to two mutually coupled transmission elements). The rest of the paper details the development and subsequent testing of Vernickel's body coil, which provides an overview of the coil design and testing process.

A paper by Seifert et al. [51] highlights a potential safety concern that arises while using transmit-SENSE. Seifert found that a four-element transmit-SENSE coil had a SAR that varied by a factor of up

to 15 as the same power was applied to the coil while the phase of each element was varied. This indicates that it is possible to have a much higher SAR than one would normally expect if a multichannel transmit-SENSE coil is being used. This was proved both by simulation and by experiment.

In 2008 Robson et al. [30] published a paper which detailed how to determine the SNR and g-factor of a parallel imaging reconstruction. This is useful as looking at the g-factor allows us to compare different parallel imaging methods. The paper also proposes a Monte Carlo based method for determining SNR and g-factor.

3.3 Coupling and Decoupling

Parfitt et al. [39] authored a paper which theoretically and experimentally studies the coupling between two and three element metal strip antennas. The mathematics within this paper is specific to two and three element systems, but it still serves as a good introduction to the impedance matrix decoupling method. With some thought it is possible to adapt this paper to apply to a transmit coil with any number of transmit elements.

A proceedings abstract by Jevtic [52] introduces a decoupling method which he refers to as a capacitive ladder network. This method involves the use of rings of capacitors connecting transmission elements, with each ring removing nearest neighbour, next-nearest neighbour, etc., interactions. This decoupling method is limited to arrays of identical transmission elements (such as the coil being developed in this research

project) and cannot eliminate resistive coupling, but is still potentially useful.

The paper by Lee et al. [38] provides a very detailed mathematical treatment of the impedance matrix decoupling method for a n -element transmission coil. It also touches upon the admittance matrix method and describes the circuit model (where coupled elements can be modeled as electrical circuits). Finally, it demonstrates how a four-element array can be decoupled using a circuit composed of six four-port Π -networks. This paper has proved very useful when attempting to decouple coil elements.

3.4 Travelling-wave Magnetic Resonance Imaging

TW MRI was first proposed by Brunner et al. [3]. In this letter the authors first introduce the concept of TW MRI, then show the results from experiments conducted using a patch antenna. They provide some very promising images of a human leg, which show considerable improvement in B_1 homogeneity when using the travelling-wave approach. A list of TW phenomena which may also occur in TW MRI is given, which provides a good starting point for investigations into TW MRI.

Webb et al. [53] have developed a small 8 cm diameter loop coil for use in imaging and spectroscopy of the human leg. They found that they could freely move the coil around and change its orientation and still get good results. This paper is the first paper to be published on

TW MRI after Brunner et al. [3] first proposed the TW method. It demonstrates the strengths of the TW method well, i.e. the versatility of being able to move the antenna and the large FOV.

Chapter 4

Methods

4.1 Magnetic Resonance Imaging Hardware

The main pieces of hardware in a MRI scanner are the magnet, the shims, the gradient coils, the RF coils and finally the computer system used to control all of the other components (see Figure 4.1). The magnet produces a highly homogeneous, strong magnetic field using either electrical current flow or the presence of magnetic material. The shims are designed to create weak spatially varying magnetic fields which cancel out external magnetic fields and other distortions to the magnet's magnetic field, allowing the magnetic field from the magnet to be truly homogeneous in the centre of the bore. The shims are either coils with electrical currents passing through them or pieces of magnetic material placed within the magnet bore, or both. The gradient coils usually consist of three separate coils, each designed to produce magnetic field

gradients in one of the three orthogonal directions within the magnet. These gradients allow different slices within the imaging volume to be selected for imaging.

RF coils can either consist of a transmitter and a receiver coil, or a single coil which both transmits and receives (a so-called ‘transceive’ coil). Both RF coils are tuned to the Larmor frequency (at the current field strength) of the spin system being imaged. The transmit coil generates a linearly or circularly polarised RF field which is orthogonal to the main magnetic field direction. This is the oscillating time-dependent B-field, mentioned in the previous section, which is absorbed and creates the stimulated emission that is the MR signal. The receiver coil detects the MR signal. RF coils are designed with imaging particular regions of a subject’s anatomy in mind, e.g. coils can be designed to image the entire body, the calf, the liver or the head. Within these anatomical regions it is desirable for the coil sensitivity and the oscillating B-field to be homogeneous so that a clear and undistorted image can be obtained. It is often very difficult to achieve this in practice. Both coils also need to be efficient and have a good signal-to-noise ratio (SNR).

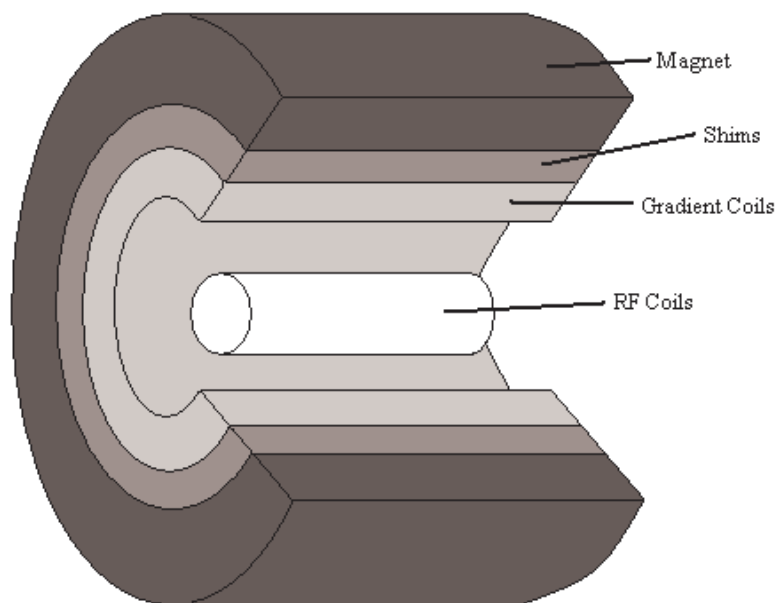


Figure 4.1: A MRI System

4.2 Imaging with Experimental Coils

When imaging with experimental coils there is a danger of overloading the coil due to a poor power setup, and also of injuring any patients being imaged through incorrect SAR settings. Once a coil has been constructed and properly tuned and matched, a coil data file must be compiled with correct power and SAR settings so that the scanner knows how to use the coil safely. This requires accurate simulations of the B_1 generated by the coil at the desired imaging location, as well as the SAR in the head, whole body, extremities and locally (measured in $W/Kg/\mu T^2$).

The simulated B_1 value is fed into the coil data file and is then used, in conjunction with the scale reference value, as a starting point for the scanner's power optimization. The scale reference value must be determined experimentally. A series of spectroscopy sequences must be run with a range of flip angles. If the scale reference value is set correctly, the spectrum with the largest signal will occur for the 90° sequence. If the spectrum with the largest signal is not the 90° sequence, the scale reference value is adjusted until the 90° sequence does produce the largest signal.

The simulated SAR values are also stored in the coil data file. Whenever a scan is run the scanner compares these values to pre-defined SAR limits (in W/Kg) and will not allow the scan if the threshold is exceeded. The SAR limits used by the Philips seven T Achieva system are given in table 4.1.

SAR parameter	SAR limit (W/Kg)
Whole body	4.0
Head	3.2
Local	10
Extremities	20

Table 4.1: SAR limits used by Philips seven tesla Achieva system

4.3 Transmit Sensitivity Encoding Coil Construction

4.3.1 Single Element Coils

In order to investigate preliminary construction ideas and methods, two single element coils were constructed. The first was a simple flat stripline measuring 25 cm long. It was constructed from 25 mm copper tape and supported on a corrugated cardboard frame. A single tuning capacitor was soldered across one end of the stripline. This coil is shown in Figures 4.2a and 4.3a. This stripline was used to try out different values of tuning capacitor, as well as for practice using the network analyzer and pick-up loops. The stripline was a very useful first step as it was completed in about an hour and thus allowed testing to be performed quickly.

After the straight stripline had been completed a second stripline was built. This stripline was curved through 90° but retained a length of 25 cm. Two capacitors were incorporated into the design, one for tuning and the other for matching. The capacitors were placed at either end of the stripline. The stripline can be seen in Figures 4.2b and 4.3b. This stripline was built so that the difference between a straight and a curved stripline could be investigated. The choice of simple materials (corrugated cardboard and copper tape) allowed it to be constructed rapidly.

Comparing the two striplines it was possible to conclude that the resonant frequency of the curved stripline was just below that of the

straight stripline, presumably due to the increased inductance created by curving the element.

A second curved stripline was then constructed (identical to the first) so that the coupling between two elements could be investigated. The quality factors of the two elements were measured individually, and then again with the elements close together in various configurations. The quality factors were measured using two pick-up loops. The first loop was coupled to the element in question to drive it, and then the second loop was coupled loosely to observe the element's resonance frequency. The quality factors of the two elements were found to be 316 and 328, which was deemed to be suitably close given their relatively crude construction.

With both elements touching at right-angles coupling was observed with coupling constants of $K = 4.22 \times 10^{-3}$ and $K = 1.04 \times 10^{-2}$. With the elements touching in a co-planar arrangement (so that the two elements formed a 'C' shape) no coupling was observed. From this it was concluded that coupling between elements could be a problem for the element interactions where the elements were close, but for other interactions there would be little or no coupling.

4.3.2 Mock-Coil

A mock coil was constructed to allow the coupling between elements to be investigated in greater detail. This coil consisted of eight curved elements arranged radially to form a hemisphere. These were 10 mm copper tape supported on a corrugated cardboard frame. A thin card-

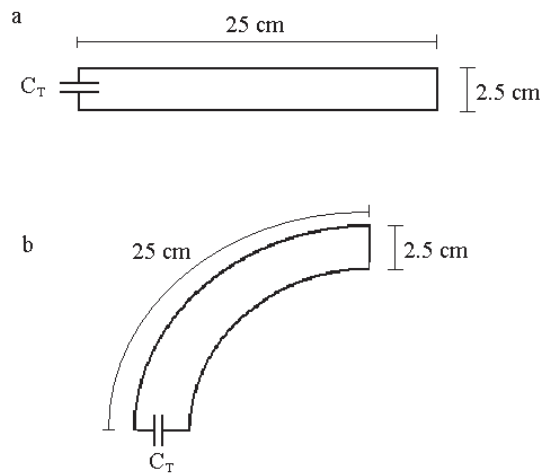


Figure 4.2: a) Diagram of a simple flat quarter wave stripline. b) Diagram of a curved quarter wave stripline.

board dome was constructed and lined with copper sheet to create a screen for the elements. The frame and screen were held together by loops of string passing through the screen and around the frame. Tuning and matching capacitors were added in the same way as for the single curved element. The $50\ \Omega$ points for the elements were found (approximately 3 cm from the top of each element) and BNC connectors were soldered into place at them. This coil is shown in Figure 4.4.

Each element was tuned and matched individually, with all other elements broken (i.e. their tuning capacitors had been removed to break the circuit). The coupling between elements could be observed by driving one element directly (i.e. plugged in via its BNC port) using the network analyzer and monitoring the second element directly



Figure 4.3: a) Picture of a simple flat quarter wave stripline. b) Picture of a curved quarter wave stripline.

on the network analyzer. The strength of the different coupling interactions, referred to as coupling cases A, B, C and D, where A is nearest-neighbour coupling, B is next nearest-neighbour, etc, were measured. From these results, see table 4.3.2, it was determined that the case A coupling was the strongest and therefore had to be eliminated first.

4.3.3 Decoupling

The first attempt at decoupling used with the mock coil was a simple T-circuit placed directly between two nearest-neighbour elements as shown in 4.5a. A range of capacitances and inductances were tried. Eventually it was decided that the T-circuit was not providing any decoupling and so it was removed.

The next method for decoupling to be tried was a simple wire connecting the two elements. A thin piece of copper tape was placed across the gap between the two elements and was moved up the elements in 1 cm increments while the coupling was observed using a search coil

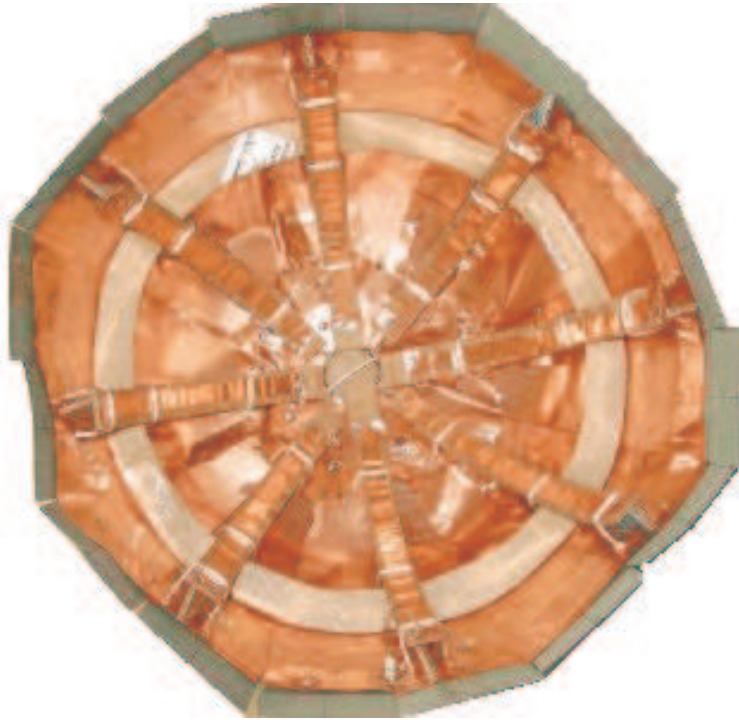


Figure 4.4: The mock coil, which was constructed from cardboard and copper sheet.

on the network analyzer (see Figure 4.5b). It was found that with the copper tape approximately 5 cm from the end of the elements decoupling was achieved, and placing the copper tape at a higher position introduced another resonant frequency into the system which was undesirable. A second piece of copper tape was then used to decouple a third element. Although this method had achieved decoupling, it was also found that it was shifting the resonant frequency of the elements by approximately 5 MHz. This decoupling method was implemented incrementally, decoupling an additional element each iteration until all eight elements were decoupled. However, driving one element and ob-

Case	K_1	K_2	K_{AV}
A	6.7×10^{-3}	5.1×10^{-2}	2.9×10^{-2}
B	2.0×10^{-2}	6.6×10^{-3}	1.3×10^{-2}
C	0	3.4×10^{-2}	1.7×10^{-2}
D	3.4×10^{-2}	6.6×10^{-3}	2.0×10^{-2}

Table 4.2: The average two coupling constants for each coupling case, and their average.

serving another by connecting it directly into the network analyzer (as opposed to using a search coil), revealed that the second element was also transmitting. This indicated that this form of decoupling was not actually decoupling the elements; it was turning them into a birdcage coil.

The third method of decoupling was an extension of the second, where a tunable capacitor was placed between the centre of the copper strip used in the second method and the coil screen as shown in Figure 4.5c. This method is detailed in an abstract by Wang [54]. Various different size capacitors were investigated, as were different copper strip positions. Changing either the position of the strip or the value of the capacitance affected which frequency was being effectively decoupled. After much experimentation it was decided that this method of decoupling was also going to be inadequate.

A form of inductive decoupling was then employed. First a simple loop of wire was suspended between the two elements, close to the matching capacitors. It was found that this helped decrease the coupling, but only by a small amount. The loop was then bent into a

‘figure of eight’ shape. This increased the decoupling even further, but it still did not amount to much. These methods are shown in Figure 4.5d.

The most effective form of passive decoupling was found to be the addition of a 1 cm tall curved screen. The screen was soldered onto the coil’s RF screen in the middle between the elements to be decoupled, and is shown in Figure 4.5e. This managed to achieve decoupling of approximately 9 dB, where all previous methods had only achieved 1 to 3 dB.

The best decoupling was achieved when a decoupling circuit was constructed and inserted between the two driving ports for the elements. This circuit was a T-circuit as shown in Figure 4.5f. With the correct selection of inductor and capacitors decoupling as good as 20 dB could be achieved.

4.3.4 The First Dome Coil

The first dome coil (see Figures 4.6 and 4.7) was constructed from two fiberglass hemispheres, one with a radius of 155 mm and the other with a radius of 175 mm. The smaller hemisphere was used to support eight transmission elements made from 1 cm wide copper tape. The larger hemisphere supported an RF screen. The two hemispheres were held together by eight plastic bolts, which allowed the hemispheres to be separated when necessary. The coil was also mounted on a stand which held it in position in the scanner and which could also support a phantom in the centre of the coil. High power capacitors were placed at

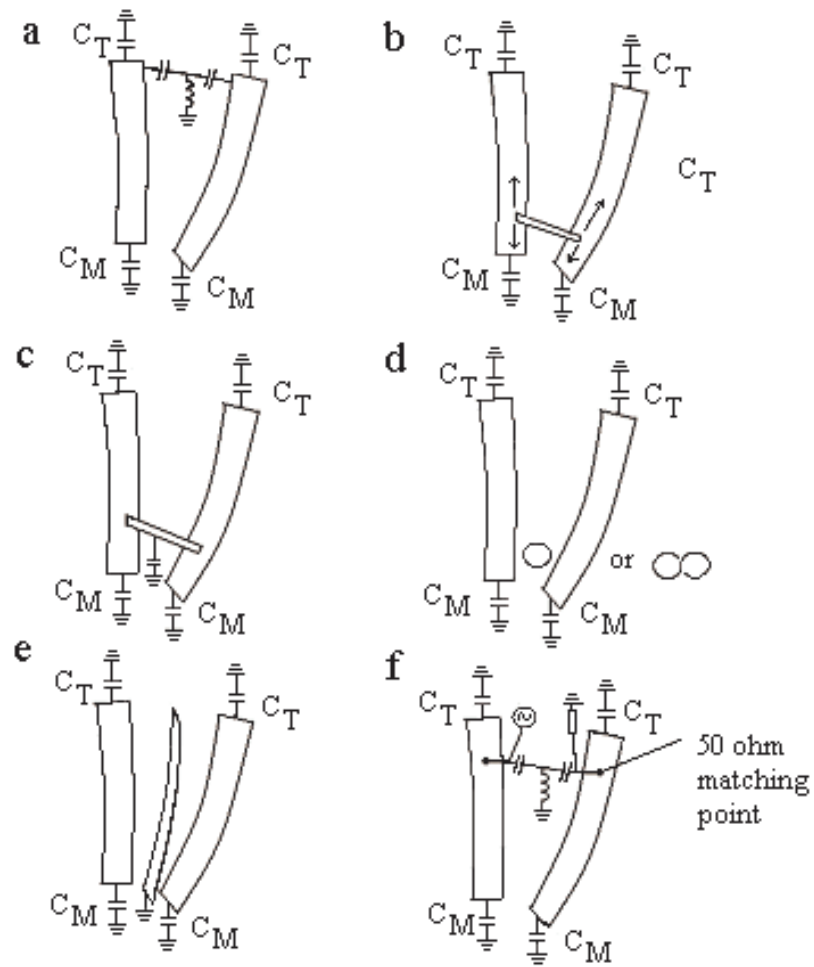


Figure 4.5: Different attempts at decoupling the mock coil. a) a T-circuit at the apex of the elements. b) A direct connection between elements. c) A direct connection with a capacitor to ground. d) Inductive decoupling using a loop and a ‘figure of eight’. e) A screen between the elements. f) A T-circuit between the driving ports.

either end of each transmission element for tuning and matching. BNC connectors were placed in the larger hemisphere so that they earthed the RF screen and fed through to the 50 Ω points on the transmission elements.

The RF screen was constructed from three layers as shown in Figure 4.8. The first layer consisted of tapered copper strips which were arranged radially so as to cover the entire hemisphere, leaving only a 3 mm gap between strips. The second layer was a dielectric which covered the entire hemisphere. The third layer was another layer of tapered copper strips, but with the strips placed so that they covered the gaps in the first layer. This screen structure allows current to travel up and down each element, but not from one element to another as there is no direct path of conductor connecting any of the elements. This design of RF screen also limits Eddy currents and blocks RF signals from reaching the transmission elements from outside the coil.

It was found that with an accurately constructed RF screen the coupling between elements dropped significantly compared to the mock coil. With such a reduction in coupling, it was no longer necessary to employ any further decoupling techniques, such as a screen between the elements or a T-circuit across the driving ports.

4.3.5 The Second Dome Coil

The second dome coil (see Figures 4.9 and 4.10) to be constructed was slightly smaller than the first so that it could fit inside a set of hemispherical gradients. The radii of the two fiberglass hemispheres were 130 mm and 150 mm. The transmission elements were formed from 1 cm wide copper sheet, rather than copper tape, as it is more rigid. The RF screen was the same, but with the addition of a 3 mm gap (cut through all three layers of the screen) in the middle between

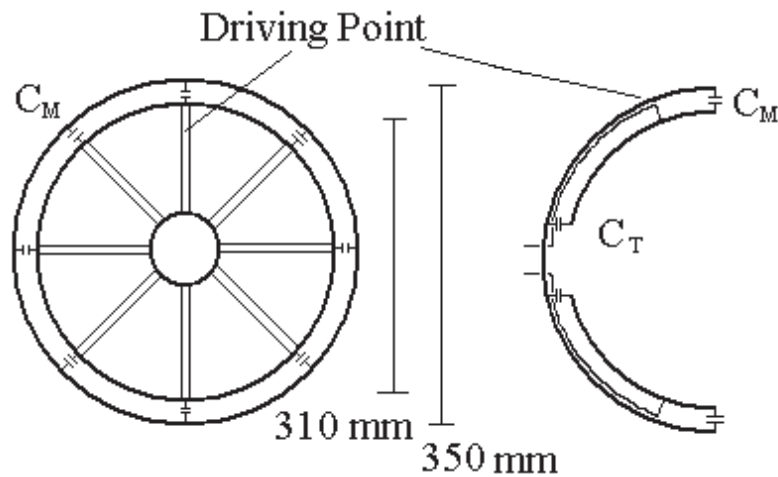


Figure 4.6: Schematics of the first dome coil.

each transmission element. This gap helped to isolate the transmission elements from each other further. High power variable capacitors were placed at the apex of each element, and fixed capacitors were placed at the tops. Each element was fed directly by a coaxial cable which entered the coil at the apex and was tack-soldered to the RF screen up to the feed point. This provided the ability to adjust the feed point slightly in order to alter the matching.

4.3.6 Coil Stand

A coil stand was designed and constructed that can hold either the first or second dome coil in the seven T Achieva scanner. The stand sits in the same position that the head coil would normally occupy and also incorporates a removable phantom holder. The stand was constructed entirely from plastic to make it MRI compatible. See Figure 4.11 for schematics and a picture of the stand.

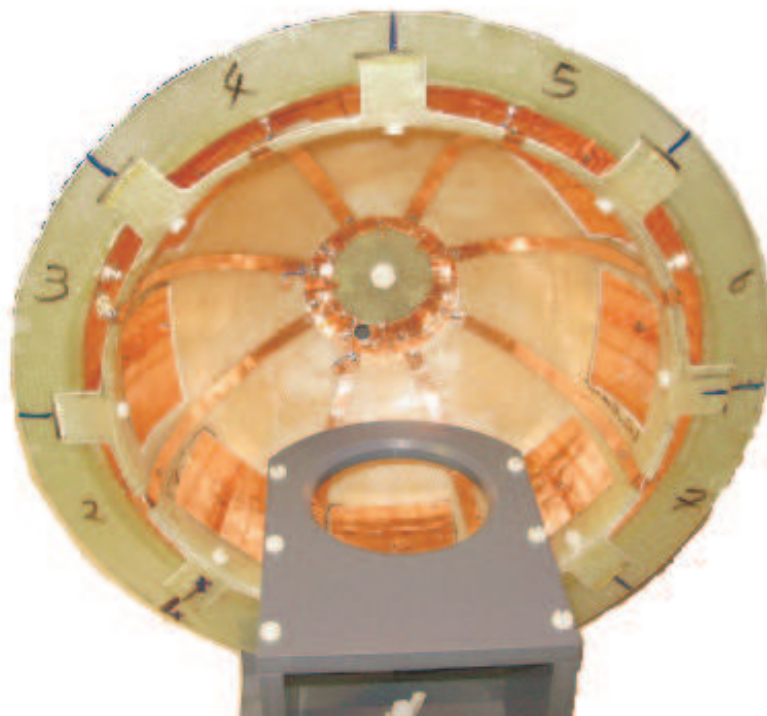


Figure 4.7: The first dome coil, with a grey phantom holder visible in the bottom of the image.

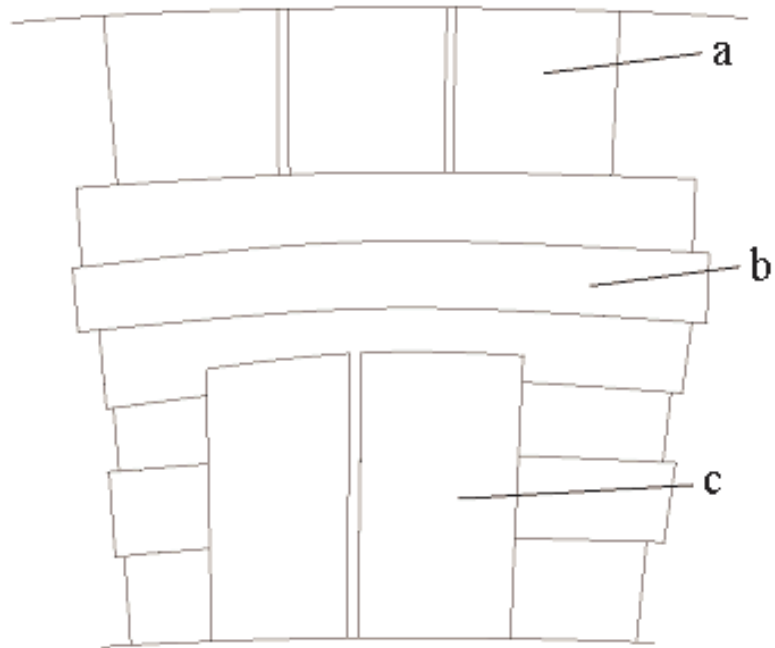


Figure 4.8: A peeled-back schematic of the RF screen. a) the first layer consisted of vertical copper strips, each separated by 3 mm from the neighbouring strip. b) the second layer consisted of horizontal strips of dielectric tape. c) the third layer was another layer of vertical copper strips, but staggered relative to the first layer so that the centre of each strip covered the gaps in the first layer.

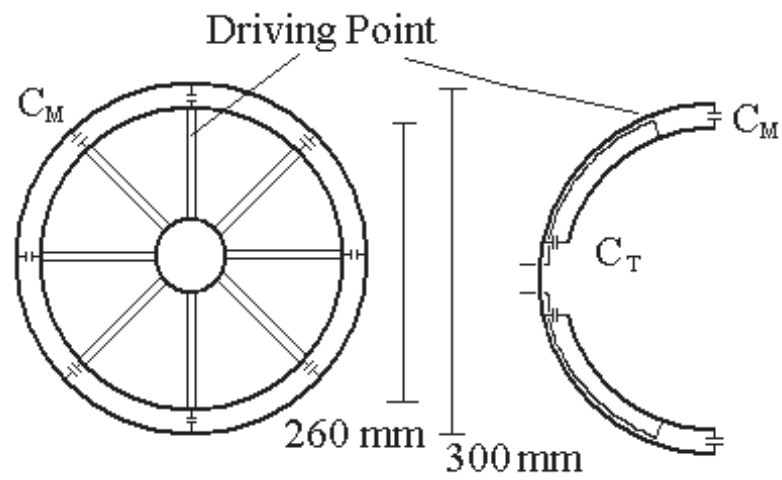


Figure 4.9: Schematics of the second dome coil.



Figure 4.10: The second dome coil, with a grey phantom holder visible at the bottom of the image and the eight BNC cables for driving the elements visible in the bottom left.

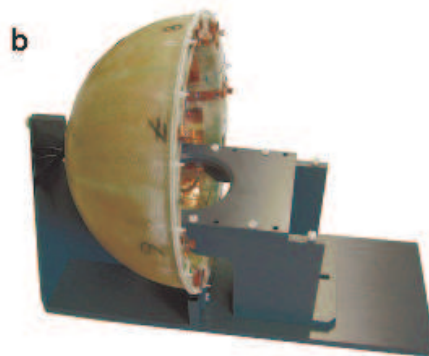
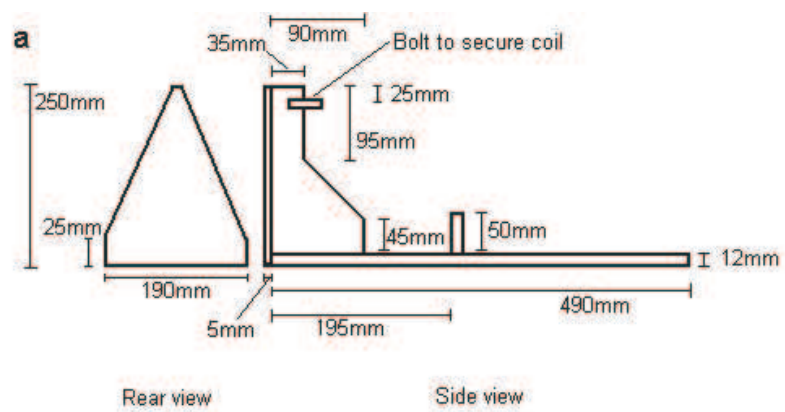


Figure 4.11: a) coil stand schematics. b) the coil stand with a coil and the phantom holder in place.

4.4 Travelling Wave Antennas

4.4.1 The Patch Antenna

The patch antenna was formed from three layers. The first layer was a 230 mm radius ground plate (circuit board). The second layer was 11 mm thick dielectric (perspex), with a radius of 200 mm. The third layer was a 188 mm radius transmission plate, made from 1 mm thick copper sheet. Two N-type connectors allowed the antenna to be driven in quadrature. These were placed 100 mm from the centre of the antenna, 90° apart. The layers were held together by four bolts, which allowed the layers to be separated and adjusted as necessary. The antenna was mounted on a plastic stand which allowed it to be placed inside the magnet where the head coil would normally be situated. See Figures 4.12 and 4.13.

Once constructed the antenna was used for imaging twice. The second set of images were obtained with the phase of the connectors reversed. By comparing these two sets of images it was possible to determine which connectors should be connected to the 0° and 90° phase signals in order to achieve maximum SNR.

4.4.2 The End-Fire Helix Antenna

The helix (see Figures 4.14 and 4.15) was wound from 2 mm radius copper wire. The helix consisted of three right-handed turns, with a 65 mm radius and a 180 mm pitch. The helix was supported on a perspex cylinder, the radius of which had been increased to the desired value

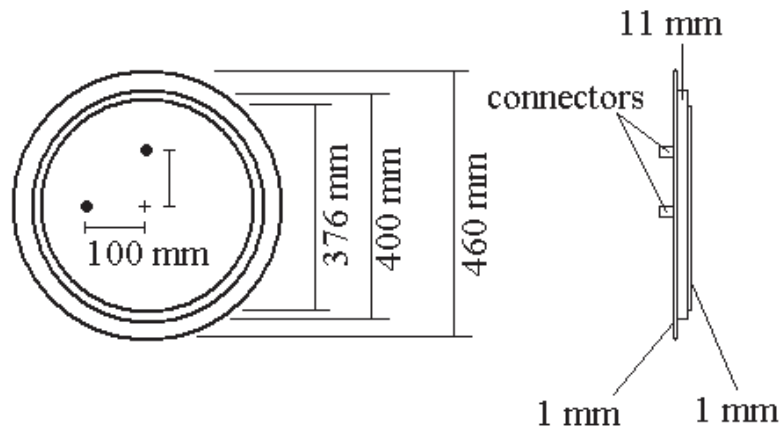


Figure 4.12: Schematics of the patch antenna.

by adding small plastic strips along the length of the tube. At the end of the helix the copper wire was bent into the centre of the helix, where it passed through a 300 mm square ground plate (circuit board). The copper wire then connected to a tuning and matching circuit. See Figure 4.16. In this circuit L_1 consists of 9 turns of diameter 5 mm and is 16 mm long. L_2 consists of 13 turns with a diameter of 5 mm and a length of 25 mm. The variable capacitor is 1 to 10 pF.

An identical left-handed antenna was also constructed. This antenna had much worse SNR than the right-handed antenna, indicating that the right-handed antenna had the correct polarity.



Figure 4.13: The patch antenna.

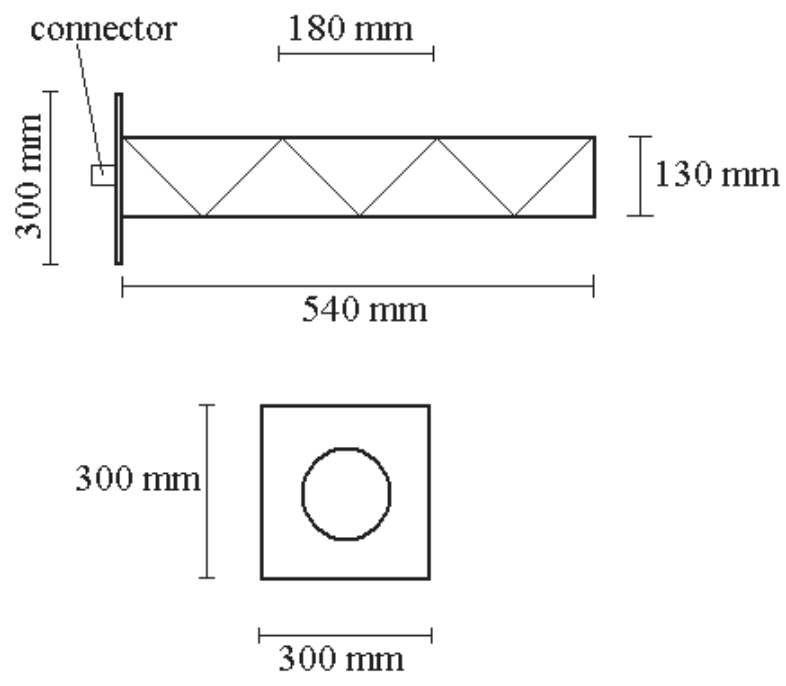


Figure 4.14: Schematic of the end-fire helix antenna.

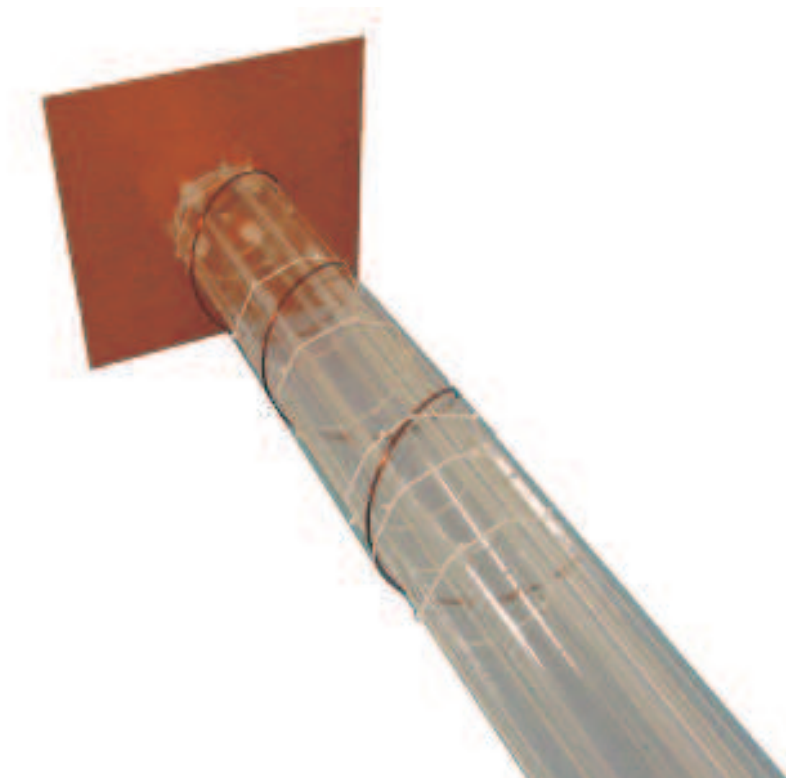


Figure 4.15: The end-fire helix antenna.

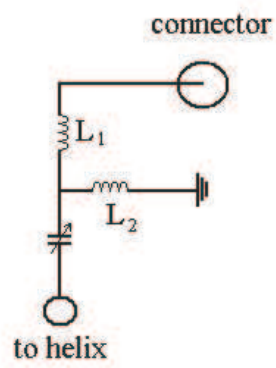
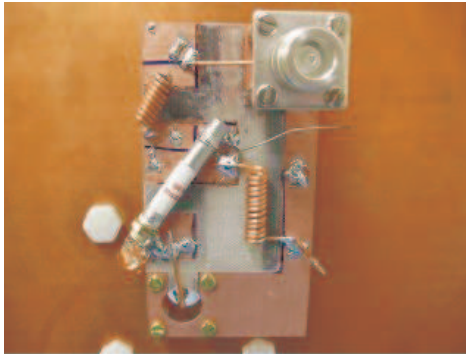


Figure 4.16: Top: a picture of the tuning circuit used for the end-fire helix. Bottom: corresponding circuit diagram.

4.5 Simulations

Simulations were performed using a software package called XFDTD Bio-pro version 6.3.8.3, produced by Remcom Incorporated. XFDTD uses the FDTD approach to model EM systems. A screen shot of XFDTD is shown in Figure 4.17.

The software contains a computer-aided design (CAD) element which can be used to design the physical aspects of a coil or antenna, and then electrical components, such as capacitors and inductors, can be added. This also allows the importing of a standard body model (either of a full body or a head and shoulders) into the simulation.

The coil can be driven in a number of ways, but in this project the coils were always driven by a direct current stimulation at the coil's feed points. The current was equal to 1 A and the feed point had a resistance of 50Ω . For initial simulations that were designed to determine the resonance frequency of system, the input was a Gaussian pulse. For subsequent simulations the input was a sinusoid at the resonant frequency of the system (298 MHz).

Simulations can be set to end after a certain time period or set number of phase cycles of excitation have elapsed, or after the simulation converges. Convergence occurs in one of two ways depending upon the excitation being used. If the excitation is an impulse the simulation will converge once the EM energy of the simulation has decayed below a pre-established threshold (typically -30 to -50 dB of the initial EM energy). If the excitation is a continuous sinusoid the simulation will converge when the average electric field of the simulation (monitored

at a number of positions throughout the simulation) does not deviate from a true sinusoidal oscillation (again, typically -30 to -50 dB from a pure sine wave). If a simulation does not converge then any SAR data extracted from it cannot be considered reliable, if extracting the data is even possible.

XFDTD can be instructed to produce various types of data from a simulation. The raw data extracted in this project were voltage and current at the driving ports as a function of time, the H_x , H_y and H_z values at given points, as well as SAR and 10 g averaged SAR values throughout body models. Field snapshots and movies could also be recorded in the different planes of the simulation.

Finally, XFDTD has a number of built in post-processing functions. XFDTD can perform fast Fourier Transforms on the voltage and current data from the driving ports and display the resulting spectra. This was used to determine the resonant frequency of the system after it had been driven by a Gaussian pulse. H values from a point can also be plotted, and their peak values can then be read from the graph and combined in quadrature to determine the B_1 at a point.

SAR values can be calculated for different sub-regions of the body model and can be scaled to different input power values. Any SAR values used in this project were scaled to the calculated input power of the simulation, as this was the power that generated the B_1 that we measured in the simulation. The software reports the maximum SAR and its position within the specified sub region, as well as the 1 g and 10 g averages with their positions. These values can be restricted to

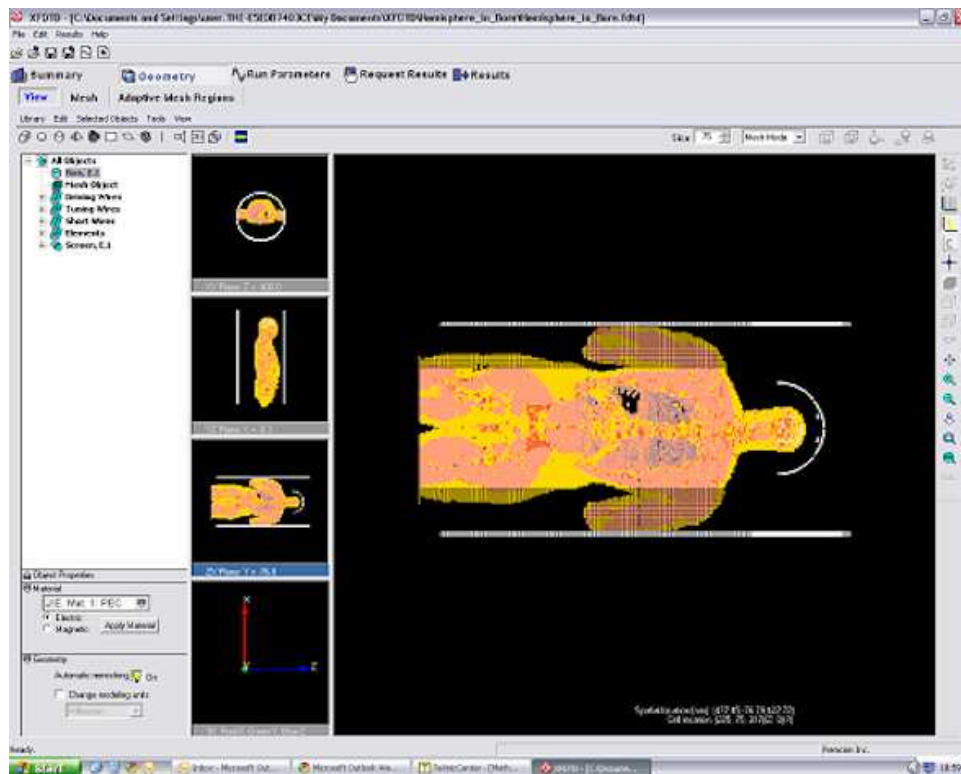


Figure 4.17: A screen shot of an XFdtd simulation that is ready to run. This simulation contains a hugo body model, a dome coil and a magnet bore.

individual tissue types from the body model, but in this project only SAR values for all tissue types were used.

Typical results from an XFdtd simulation can be seen in Figures 5.6 and 5.7 in chapter five.

4.6 Calibrating Coils

4.6.1 Power

The process of calibrating a coil involves determining a number of values which must then be written into a coil parameter file which the MRI scanner can then refer to when using the calibrated coil. The most important values are associated with the coil's power use; if these values are not correct then the scanner cannot produce the correct flip angles. The other important set of values are SAR to magnetic field conversion factors. These are important if the scanner is to correctly determine safety limits for each scan.

In order to calibrate the coil's power settings the settings which produce the best SNR must be identified, which will correspond to a 90° flip angle. To do this the coil's 'Ref. B1' and 'Maximum B1 Available' parameters must be set to an initial value, typically 15. The coil's 'Ref. Scale' value must also be set low, typically 0.1. The actual values for a coil's power parameters do not matter as they are only ever considered in ratio. With the scanner's automatic power optimization turned off, a series of images or spectra with different flip angles must be obtained. If the correct range of flip angles is covered, a plot of SNR versus flip angle should have a peak value. If not, a different range of flip angles must be used. Note that the flip angles requested at this stage are not the actual flip angles that the coil generates; that is why the coil must be calibrated. See Figure 4.18 for a screen shot of an example of the sequence of spectra obtained.

In the example shown in Figure 4.18 the seventh spectrum clearly has a much stronger signal than the others, indicating that it is the sequence that generated a 90° flip angle. 'Ref. Scale' is then modified to compensate according to equation 4.1.

$$\text{New Ref Scale} = \text{Old Ref Scale} * \frac{\text{FA that produced maximum signal}}{90} \quad (4.1)$$

Once this has been done the process is repeated with a smaller difference between requested flip angles, so that the desired 'Ref. Scale' value can be refined until a suitable accuracy is achieved. Once this has been done and the coil's parameter file has been updated accordingly, when a certain flip angle is requested with the calibrated coil, that is the flip angle obtained.

It is possible, once calibration has been achieved, that the scanner will no longer perform scans with these values, even though it is known that they would produce the correct flip angles were they to be run. This is probably due to the coil now needing too much power. The scanner can be told to reduce the power used by lowering the value of 'Maximum B1 Available'. This forces the scanner to use lower amplitude pulses with longer pulse durations to achieve the correct flip angles.

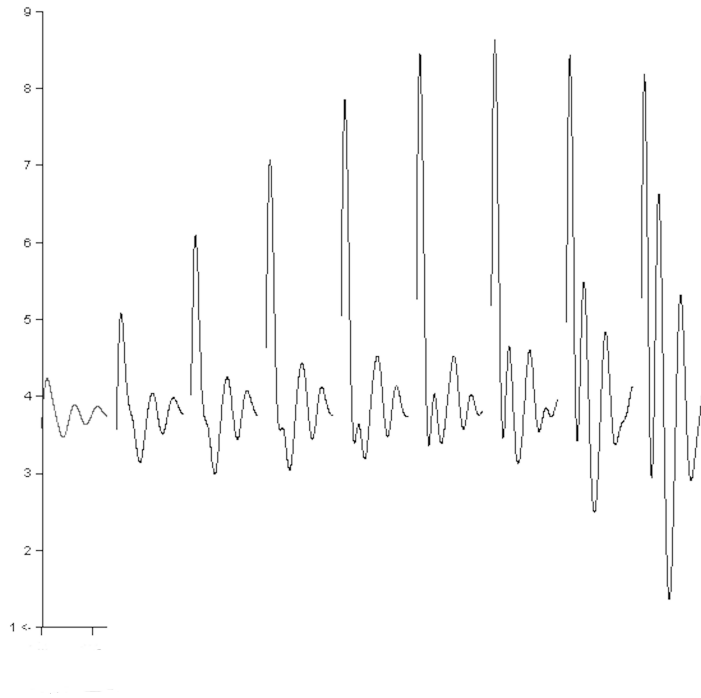


Figure 4.18: A sequence of spectra used for power calibration of a coil.

4.6.2 Specific Absorption Rates to Magnetic Field Conversion Factors

To calculate the SAR values relative to the magnetic field B_1^+ detailed simulations of the coil must be performed. The coil and subject must be simulated in XFDTD, being driven by a sinusoidal excitation at the resonant frequency, with the body model placed in a worst-case-scenario position (i.e. being as close to the transmitting elements as will be possible in the scanner). The simulation must be set up so that the B_1 generated by the coil in the target FOV, as well as the local and maximum SAR values throughout the body, are recorded. Once the simulation has converged, the maximum SAR from the head, the body,

and the extremities, as well as the maximum local SAR are taken and divided by the square of the B_1 in the FOV (measured in micro-tesla squared). These values, in Watts per kilogram per micro-tesla squared, are then copied into the coil's parameter file. The scanner uses these values to determine the SAR that the coil will produce for a given pulse sequence, and hence if a particular scan is safe or not.

If it is not clear what constitutes a worst-case-scenario for this simulation, then a whole series of simulations to cover all the possible situations must be performed, and then the most conservative results must be taken.

4.6.3 Other Parameters

Other parameters that can be set for a coil include 'Max. Avg. Power'. This tells the scanner the maximum power that the coil can handle before it breaks. It can be estimated by taking the maximum power of the components used. Similarly, 'Breakdown B1' tells the scanner the maximum B_1 that the coil can be exposed to before it breaks.

Chapter 5

Transmit Sensitivity

Encoding Results

5.1 Pulse Design

Using the theory on multiple transmit pulse design presented in chapter two a program was written in MATLAB (see appendix) which could generate unique RF pulses to drive R elements which would then excite a defined excitation pattern. In the case of the dome coil $R = 8$. The sensitivity patterns of the eight elements were obtained by using each element individually to image a 16 cm diameter phantom, and are given in Figure 5.1. These sensitivity patterns have been combined linearly in Figure 5.2 and show an almost uniform sensitivity over the phantom. These are then fed into the program along with the desired excitation, which was chosen to be the University of Nottingham castle logo (see Figure 5.3), and the gradients (a 2D spiral). The program then processes this information as shown in the theory chapter and

produces eight RF pulses, which are presented in Figure 5.4.

Note that the pulses produced are relatively coarse due to the low matrix size used in this run of the program. Using higher resolution sensitivity maps and excitation patterns (or re-sampling the current ones) would allow a bigger matrix value to be used and thus increase the accuracy of the RF pulse. This would also increase the calculation time, and so will not be implemented until the program's RF pulses have been tested.

Unfortunately it has not been possible to validate the accuracy of these pulses by implementation on a multiple transmit scanner, as the scanners currently being used by our collaborators are not yet capable of implementing independent RF pulses in each channel.

In order to test these pulses in a computer simulation, a two-dimensional Bloch simulator program would have to be developed. Such a program would take the R RF pulses and weight each one by the corresponding element's sensitivity profile. These weighted pulses would then be combined linearly to create the RF signal that the two-dimensional spin system would be exposed to. This RF signal, along with the gradients applied as the RF pulses are transmitted, would be fed into the Bloch equations (see equation 2.16) for every spin in a two-dimensional array, over a period of timesteps. The magnetization at the end of the RF signal should then resemble the desired excitation pattern used to calculate the R RF signals (i.e. Figure 5.3). This process is summarised in Figure 5.5.

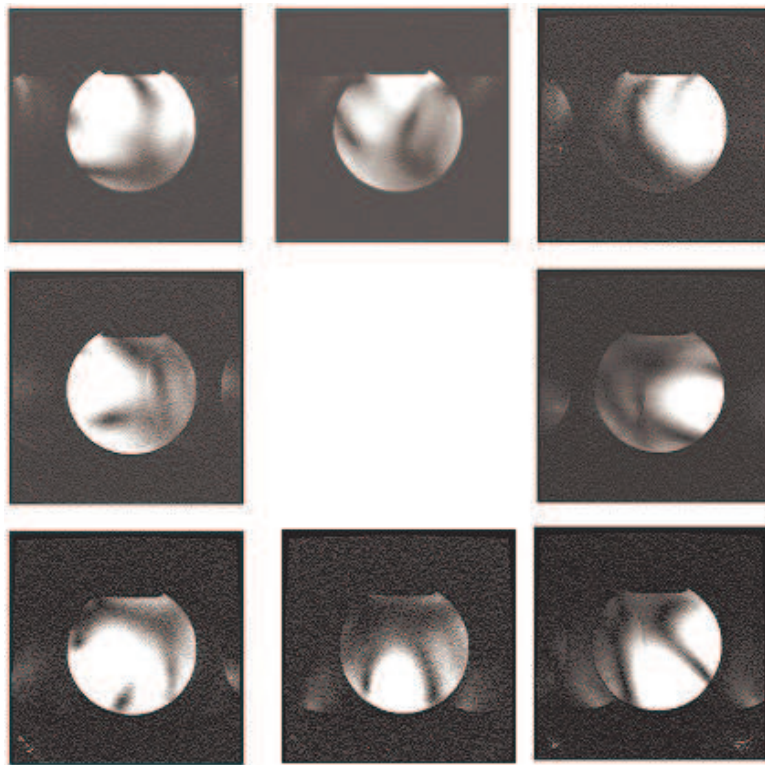


Figure 5.1: Transverse sensitivity maps for each of the eight elements of the dome coil.

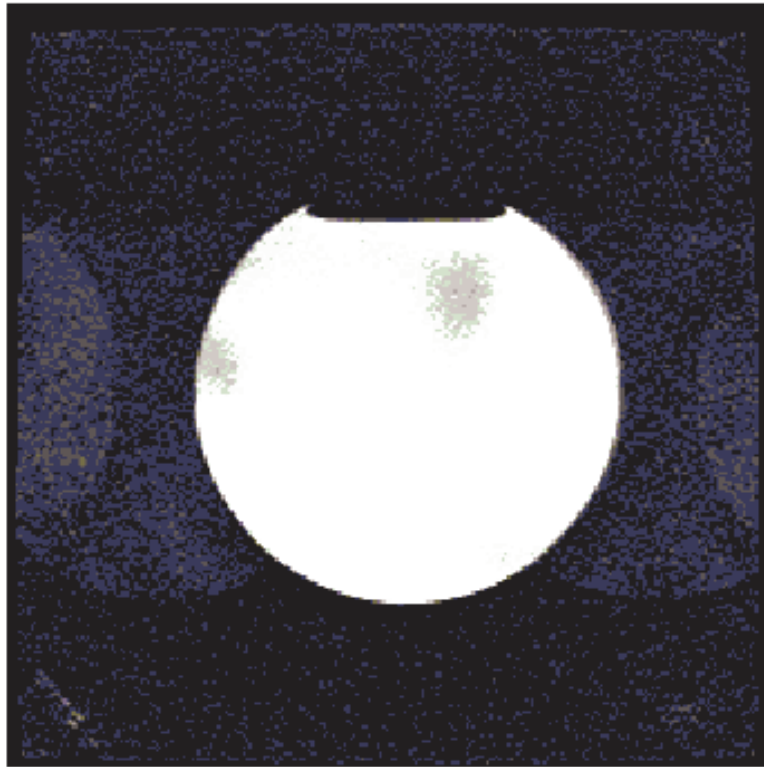


Figure 5.2: The linear summation of the sensitivity maps shown in Figure 5.1.



Figure 5.3: The University of Nottingham castle logo used as a desired excitation pattern.

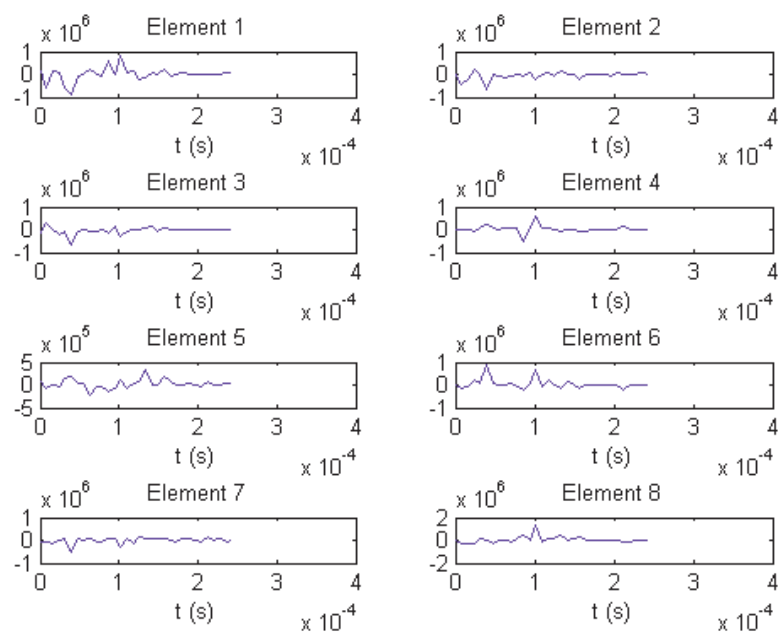


Figure 5.4: The eight RF pulses generated for use with the dome coil. If used together these should produce a transverse excitation in the shape of the University of Nottingham logo.

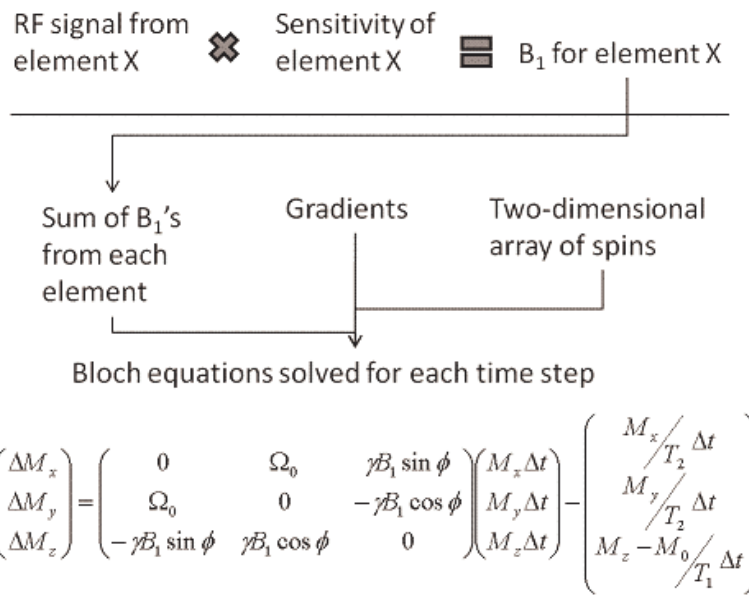


Figure 5.5: A flow diagram to demonstrate how a two-dimensional Bloch simulator would work for R RF signals. Ω_0 is the resonance offset, ϕ is the phase of the RF field and Δt is the size of the timestep used in the program.

5.2 Coil Calibration

The various power calibration parameters used by the scanner for the dome coil are shown in table 5.1.

The 'Max. Avg. Power' value is simply an estimate based on other coil files. It could be replaced with an accurate number based upon the actual maximum power that the coil can handle without breaking down.

The 'Maximum B1 Available' and 'Ref. B1' values were an estimate based upon other coil files.

An initial estimate for 'Ref. Scale' was obtained by taking a series of images with different flip angles, finding the image with the highest SNR, and then scaling 'Ref. Scale' accordingly so that the image with the highest SNR would be the 90° image. This was further refined by taking a series of spectra with different flip angles and looking for the spectra that produced the strongest signal. The final value was settled on when it could be used without the scanner giving a PO (power optimization) failure warning.

It was relatively difficult to calibrate the dome coil due to it producing phase artifacts. A range of 'Ref. Scale' values seemed to almost work. When taking this range into consideration, the error in the calibration is approximately 29%.

Parameter	Value
Max. Avg. Power	20 W
Maximum B1 Available	15 μ T
Ref. B1	15 μ T
Ref. Scale	0.4913

Table 5.1: The power calibration values used by the dome coil.

5.3 Results of Specific Absorption Rate Simulations

The SAR per B_1^2 conversion factors for the dome coil are listed in table 5.2. These values were obtained from XFDTD simulations of a human body within the dome coil (as described in the methods chapter). The B_1 was taken from five locations in a transverse slice of the head and then averaged. A video of the 'MagH' field was also taken of this slice to check that the points being observed were suitable representatives of the magnetic field, and from this it was decided to omit the point in the center of the head where there is a B_1 minimum. The average B_1 was found to be $0.45 \mu\text{T}$.

SAR values were extracted from the simulation. The whole body value uses the maximum SAR from the torso. The head value uses the maximum SAR from the head. The local value uses the maximum local SAR from the entire body model. The extremities value uses the highest maximum SAR from the body's left arm and shoulder (which was higher than the SAR of the right arm and shoulder).

SAR simulations were also performed on an eight-element birdcage coil of comparable size to the dome coil for comparison. The results of these simulations are presented in Figures 5.6 and 5.7. From Figure 5.6 it can be clearly seen that the SAR generated by the dome coil is consistently lower than the SAR generated by the birdcage. It also clearly demonstrates that the SAR generated by the dome coil in the shoulder is much less than the SAR generated by the birdcage, indicating that

Location	Watts/ $\mu\text{T}^2/\text{kg}$
Whole body	1.03
Head	23.8
Local	3.47
Extremities	1.46

Table 5.2: The SAR per B_1^2 conversion factors for the dome coil.

the dome coil has a good SAR performance in the shoulder. Figure 5.7 displays simulated B_1 data on the left and local SAR data on the right. The B_1 generated by the dome coil is restricted to the top half of the head which helps to lower the SAR in the neck and shoulders, as seen in the SAR images.

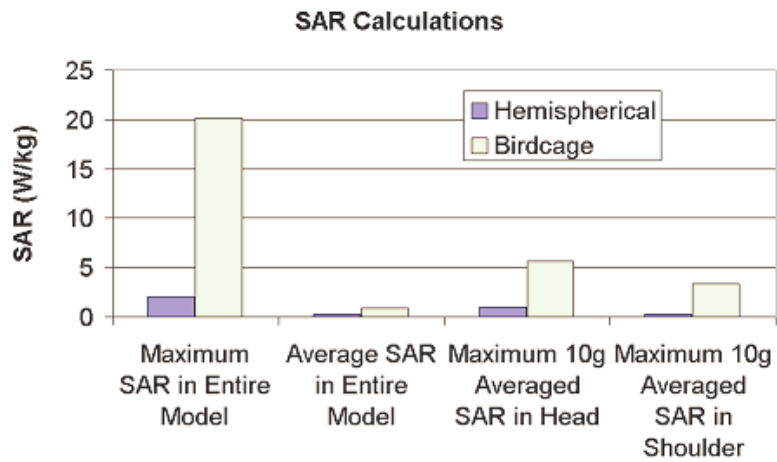


Figure 5.6: A comparison of the SAR generated by the dome coil and a birdcage coil with a B_1 of $0.45 \mu\text{T}$.

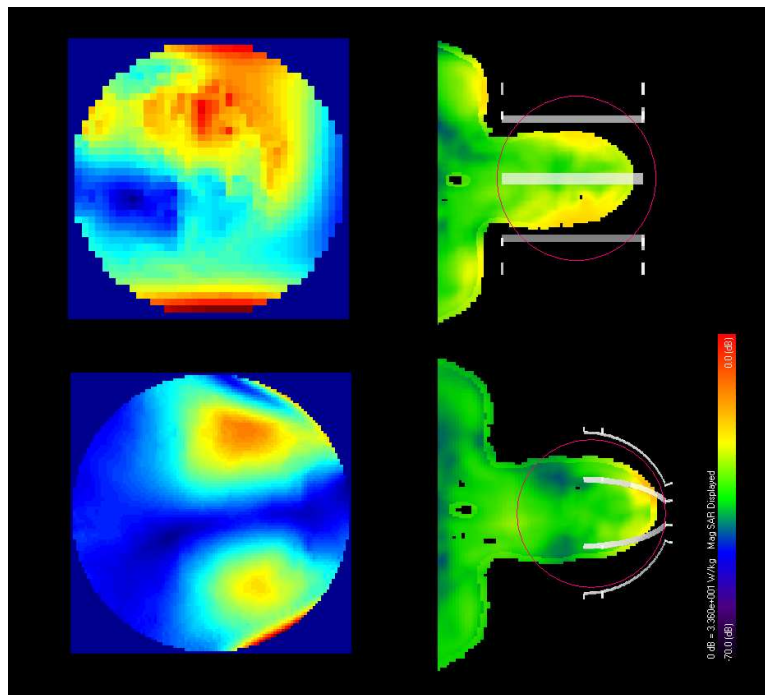


Figure 5.7: The B_1 generated by the birdcage (top left) and the dome (bottom left). The local SAR generated by the birdcage (top right) and the dome (bottom right).

5.4 Imaging

Imaging with the dome coil was performed at the Centre d'Imagerie BioMedicale in Lausanne, Switzerland, using their actively shielded seven T/68 cm MR scanner (Siemens Medical Solutions, Erlangen, Germany) with a head gradient insert (41 cm, 80 mT/m maximum gradient strength). This scanner is capable of transmitting on up to eight channels and so allowed the dome coil to be fully tested.

B_1 maps were obtained for all eight elements using the Sa2RAGE sequence and are presented in Figure 5.8. From these images it is evident that some of the elements were not performing as well as the others. Elements 3, 6, 7 and 8 were all performing well and were generating B_1 into the centre of the coil. Elements 2, 4, and 5 were hardly generating any B_1 at all, and this will have undoubtedly lowered the SNR of the images obtained from the coil. Element 1 appears to show strong coupling between itself and its neighbouring element. As all eight elements were constructed in the same way these differences in performance are believed to be the result of poor tuning and matching. It is clearly possible to tune and match the elements so that they do not couple with their neighbours and generate a strong B_1 . However such fine-tuning is a time consuming process and had to be performed on-site during the final testing of the dome coil. As the final testing was performed in a very limited time period, tuning and matching of all eight elements was not possible.

Un-accelerated images of a pineapple and a squash were also obtained, see Figures 5.9 and 5.10. These images were obtained using a

GRE sequence with a TR of 8.6 ms, a TE of 4 ms and a 1.1 by 1 by 7 mm resolution. The SNR of the pineapple image is 245 while the SNR of the squash image is 88. Using the same scanning parameters to image a phantom with a volume head coil on the Philips Achieva system resulted in SNR values of 103 and 78 respectively. Although the results are not directly comparable due to the difference in imaging system, they do demonstrate that the dome coil achieved SNR values comparable to a conventional coil.

Unfortunately it was not possible to attempt to acquire accelerated images due to time constraints. This means that it is not possible to evaluate the E parameter of the dome coil.

It was noted during the final scanning and testing session that the dome coil is quite load-insensitive, as it required no changes to its tuning or matching if the oil phantom was exchanged for a water phantom or even with no phantom at all.

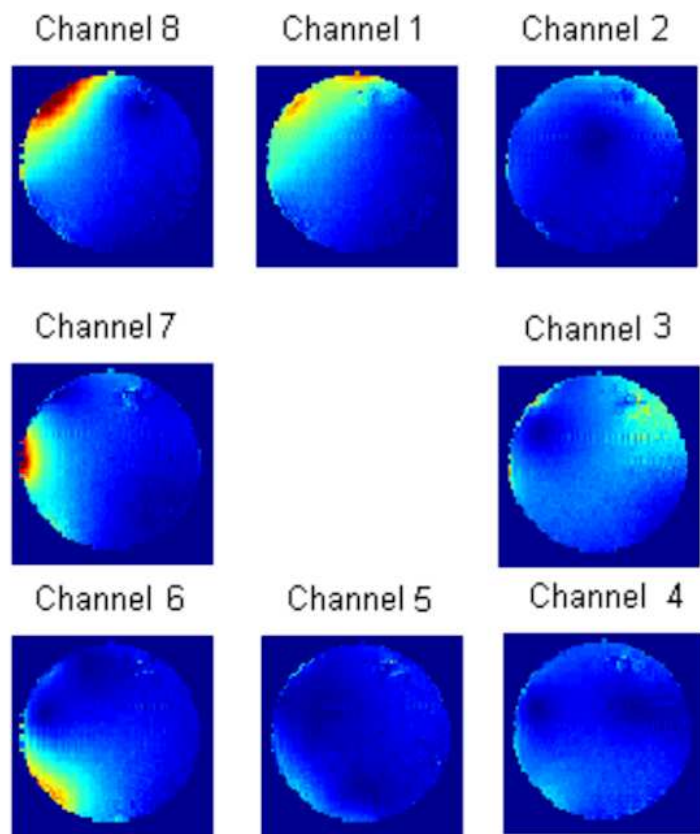


Figure 5.8: B_1 maps of all eight elements of the dome coil.

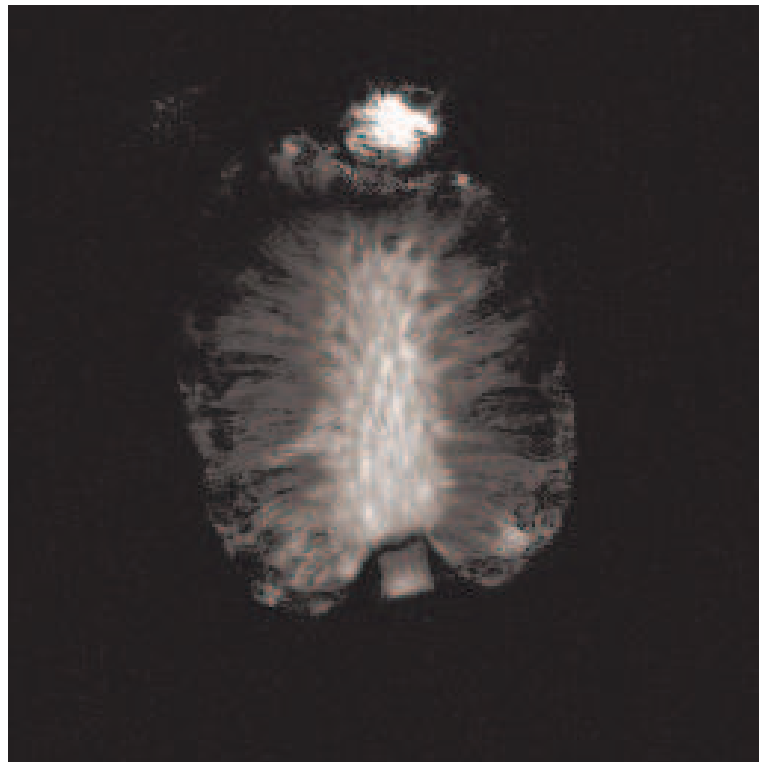


Figure 5.9: Sagittal image of a pineapple. GRE sequence, TR of 8.6 ms, TE of 4 ms, 1.1 by 1 by 7 mm resolution.

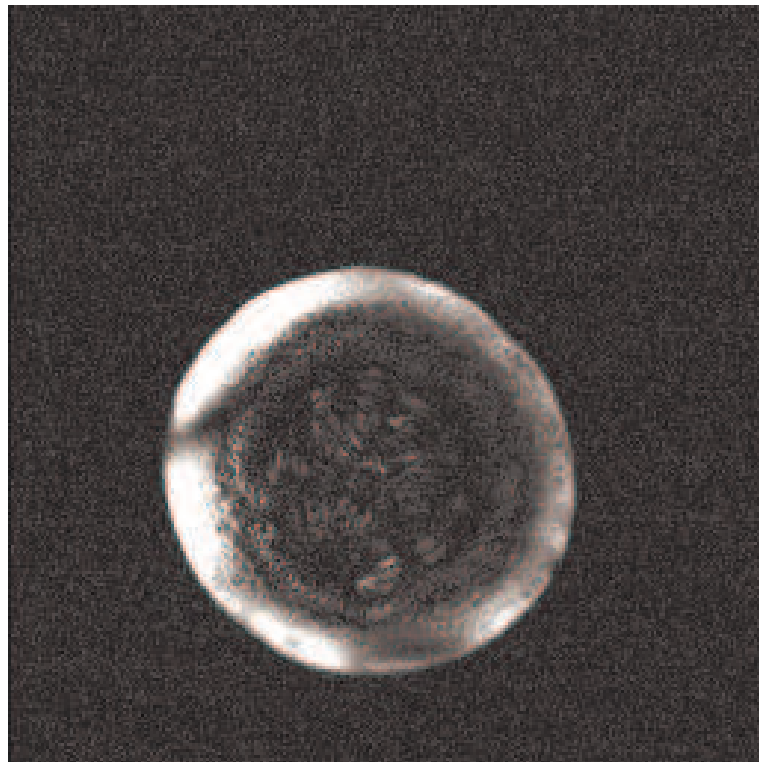


Figure 5.10: Transverse image of a squash. GRE sequence, TR of 8.6 ms, TE of 4 ms, 1.1 by 1 by 7 mm resolution.

Chapter 6

Travelling Wave Results

6.1 Simulation of Travelling Wave Behaviour

Simulations were performed of a patch antenna inside a magnet bore. A snapshot of the $\log(B_1)$ generated by the patch can be seen in Figure 6.1. The dimensions of this image have been distorted as the Yee cells in the simulation were neither isotropic nor homogeneous, but the pixels of the image are. This has no affect upon the interpretation of the image. In the simulation the bore was 2 m long and had a diameter of 60 cm.

The waves propagating outside the bore are actually generated at the back of the patch and then "bend around" the end of the bore. In reality the space outside the bore is occupied by the magnet, therefore these waves do not occur in real travelling wave experiments and so are a simulation artifacts. The space immediately in front of the patch is dominated by a near-field effect, but further away the B_1 begins to increase again indicating a region where the travelling wave effect

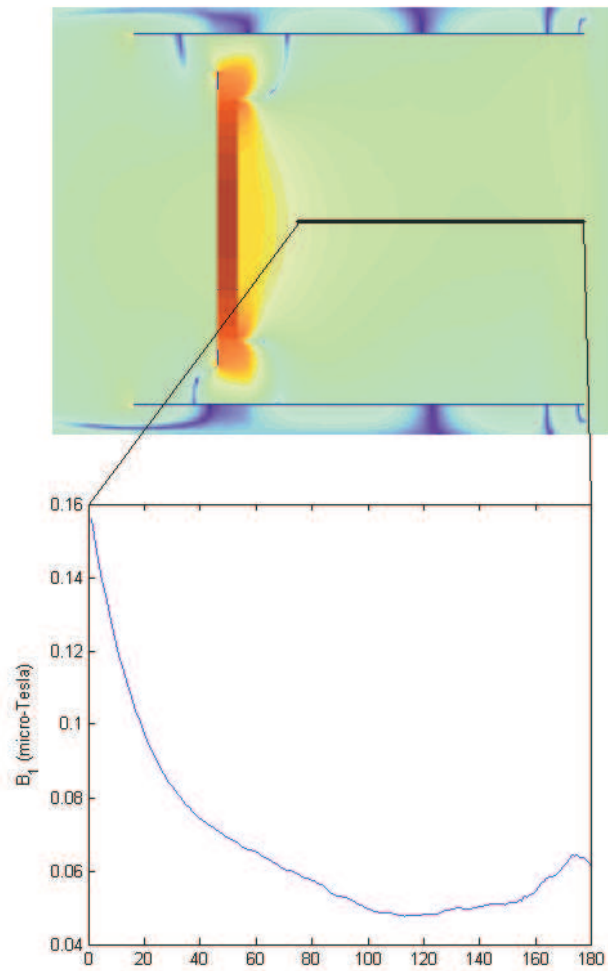


Figure 6.1: An image of $\log(B_1)$ generated by a patch antenna inside a magnet bore. The waves propagating outside the bore are simulation artifacts. The region directly in front of the patch is dominated by near-field effects. From the profile shown in the bottom of the figure it can be seen that beyond the region of near-field effects the B_1 increases, indicating a travelling wave effect.

dominates.

6.2 Specific Absorption Rate

SAR values were obtained from a range of XFDTD simulations of a human body placed in the scanner head-first with the patch antenna. In each simulation the position of the body was changed by a short distance along the z-axis. The B_1 was taken from five to eleven (depending on the cross-section of the body for that simulation) locations in a transverse slice of the body in the centre of the bore and then averaged. A video of the 'MagH' field was also taken of this slice to check that the points being observed were suitable representatives of the magnetic field. The whole body values use the maximum SAR from the torso. The head values use the maximum SAR from the head. The local values use the maximum local SAR from the entire body model. The extremities values use the highest maximum SAR from either the body's left arm and shoulder or the right arm and shoulder, whichever was higher.

See Figure 6.2 for the average B_1 from each simulation, as well as the SAR per B_1^2 conversion factors. From this figure it was evident that the SAR per B_1^2 conversion factors decreased as the body moved away from the patch. It was therefore decided that as long as a minimum safe distance of 50 cm is maintained between the subject being imaged and the patch, the SAR per B_1^2 conversion factors found in table 6.1 can be used.

SAR values were also simulated for scanning foot-first. The simulations were performed in the same way as for head-first scanning, except that extremity SAR values now also incorporated measurements from

the legs, and sometimes head values were not calculated as they had dropped out of the simulated volume (this was not a problem as when head values were simulated they were found to be very close to zero).

See Figure 6.3 for the average B_1 from each simulation, as well as the SAR per B_1^2 conversion factors. From this figure it was evident that the SAR behaved in a similar fashion to the head-first case, though SAR on the whole is much lower for foot-first scanning than head-first. It was therefore decided that as long as a minimum safe distance of 50 cm is maintained between the subject being imaged and the patch, the SAR per B_1^2 conversion factors found in table 6.2 can be used. Note that the values given in table 6.2 correspond to a distance of 40 cm from the patch. The minimum safe distance is set to 50 cm to allow for the fact that a subject may move their feet closer to the patch during scanning.

Comparing Figures 6.2 and 6.3 it can be seen that the average B_1 is much more erratic as a function of position when scanning head-first compared to foot-first scanning. This is believed to be because the human cross-section varies much more in the head-first case, particularly due to the shoulders. However when scanning foot-first the human cross-section is much better behaved as the legs taper off relatively smoothly compared to the upper body.

Location	Watts/ μT^2
Whole body	4.2
Head	9.9
Local	4.5
Extremities	34.7

Table 6.1: The SAR per B_1^2 conversion factors for the patch antenna when scanning head-first. Note that these are only valid when the subject keeps a minimum distance of 50 cm from the patch.

Location	Watts/ μT^2
Whole body	1.2
Head	0.0
Local	3.0
Extremities	12.5

Table 6.2: The SAR per B_1^2 conversion factors for the patch antenna when scanning foot-first. Note that these are only valid when the subject keeps a minimum distance of 50 cm from the patch. The head value is zero to one decimal place.

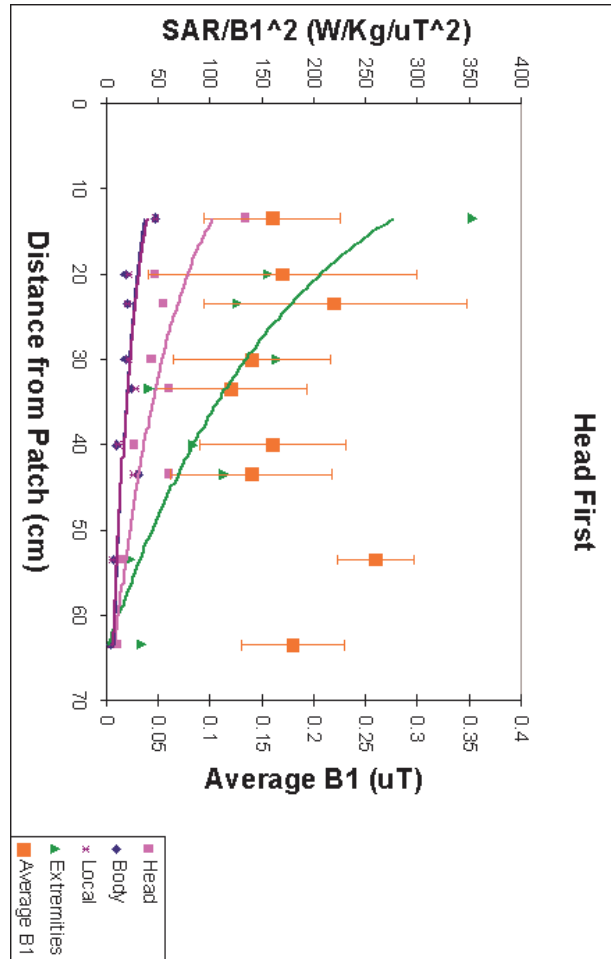


Figure 6.2: Plots of SAR per B_1^2 and B_1 for the patch antenna as a function of body position (measured in displacement along the z-axis away from the patch antenna) when scanning head-first. Error bars on the B_1 values are \pm one standard deviation.

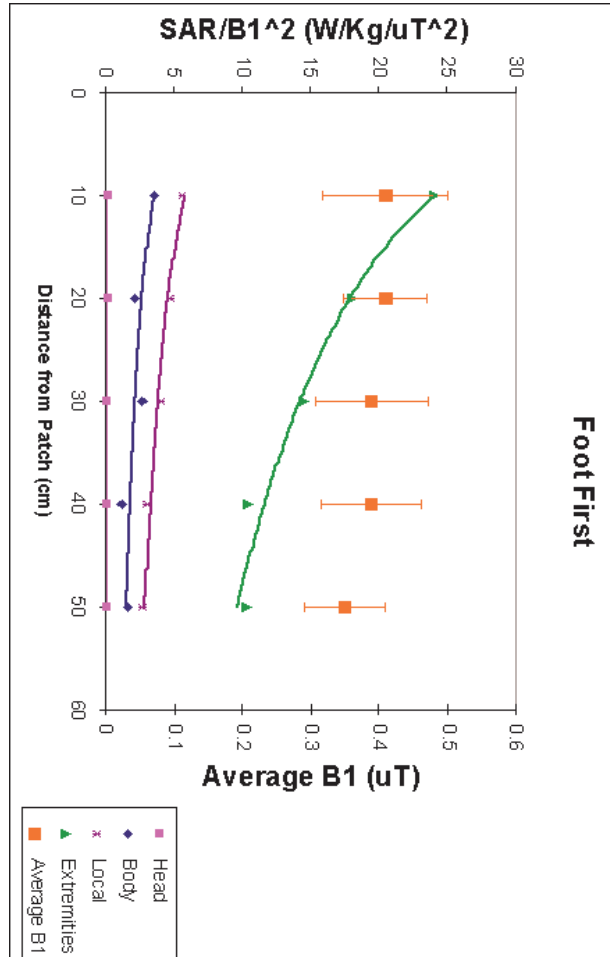


Figure 6.3: Plots of SAR per B_1^2 and B_1 for the patch antenna as a function of body position (measured in displacement along the z-axis away from the patch antenna) when scanning foot-first. Error bars on the B_1 values are \pm one standard deviation.

6.3 Simulated Patch Antenna and End-Fire Helix Comparison

The patch antenna and end-fire helix antenna were compared directly to ascertain if there were any advantages to using one antenna over the other. Simulated SAR maps were produced. After both antennas had been constructed, tuned and matched, they were used to image a 20 cm spherical phantom. The resulting images had their SNR's evaluated so that the performance of the antennas could be compared.

6.3.1 Simulated Specific Absorption Rate

Figure 6.4 shows the simulation geometries used to generate the SAR maps for both antennas. Figure 6.5 shows the results of those simulations. Note that the simulations have been scaled for the same B_1 generated in the centre of the head, to represent the same imaging conditions. The SAR maps are very similar. Both show the same distribution of SAR throughout the body, with the most occurring at the top of the head, and the least occurring between the legs. The patch appears to generate less SAR overall, and the helix produces more SAR in the top of the head, but these differences are not great.

6.3.2 Signal-to-Noise Ratio

Both the patch antenna and end-fire helix were used to image a 20 cm spherical loading phantom in the Philips seven T Achieva system. The antennas were used in both transmit and receive mode for this

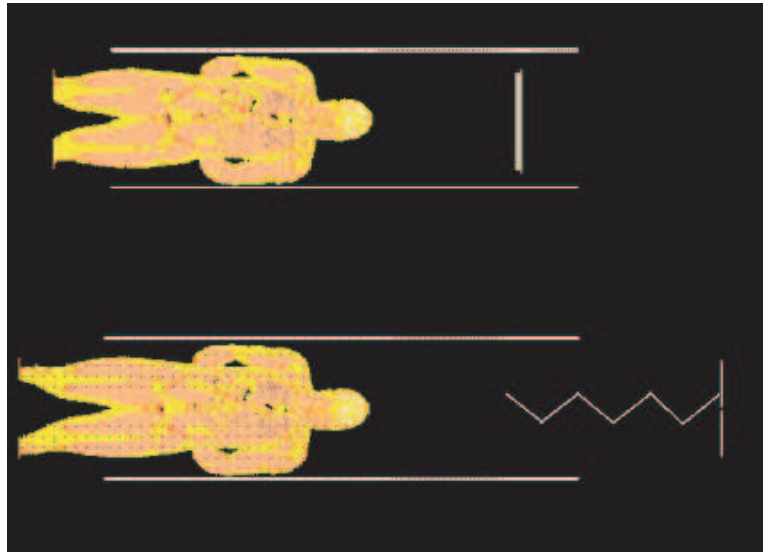


Figure 6.4: The geometries of the simulations used to generate SAR maps of the patch (top) and helix (bottom) antennas. The legs were removed to reduce the computational burden of the simulations.

comparison. The phantom was placed approximately 65 cm from the end of the antenna being used, and both antennas were driven by the same pulse sequence. The system's logs were then checked to ensure that both antennas had used the same power. As neither coil was calibrated at the time, there was no way to be sure what flip angle was being achieved, but by using the same pulse sequence at the same power the same (unknown) flip angle was achieved by each antenna and hence the resulting images were directly comparable.

Figures 6.6 and 6.7 are examples of the sagittal slices achieved using both antennas. In both images the antenna was below the phantom. It can be seen that the half of the phantom facing the antenna produced the strongest signal, while the other side did not. This is a result of

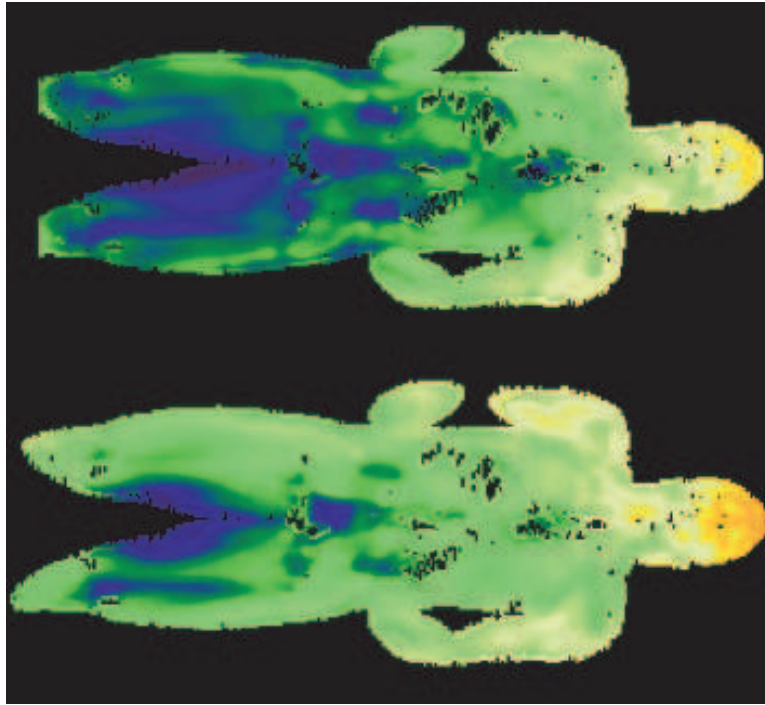


Figure 6.5: The SAR maps produced by the patch (top) and helix (bottom) antennas.

their being no attempt to match the travelling wave at the far side of the phantom. Without such matching the travelling wave reflects off the back of the phantom creating standing wave effects. This also creates the bright spot visible in the top half of each phantom.

The SNR for these images, as well as for images taken in the transverse and coronal planes, were calculated and then normalised by the power used by the antenna. Power-normalised SNR values were also obtained using a head volume coil to allow the travelling wave technique to be compared to conventional MRI imaging. These power-normalised SNR values are given in table 6.3 and shown graphically in Figure 6.8. From these values it can be seen that the helix antenna performs slightly

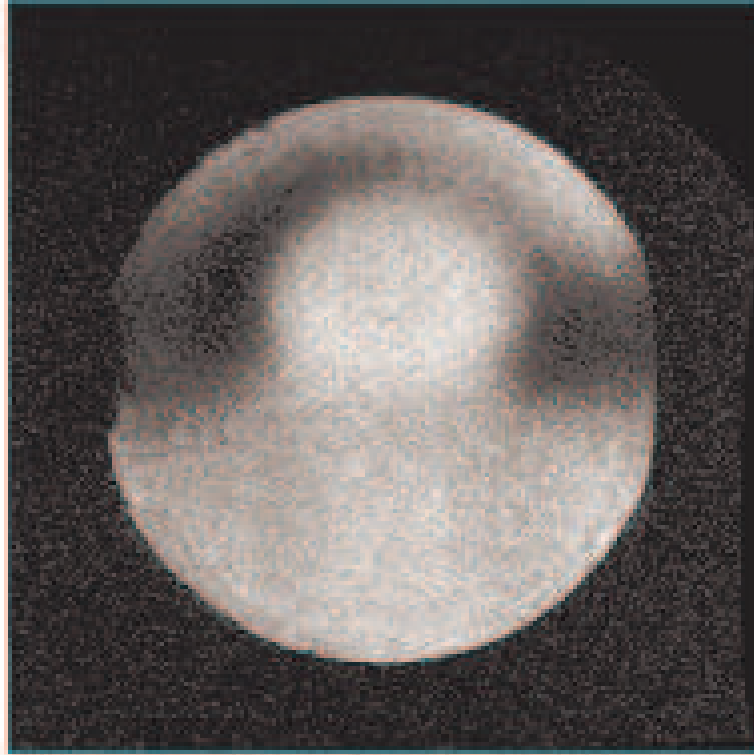


Figure 6.6: A sagittal image of a 20 cm spherical phantom taken using a patch antenna as both transmitter and receiver.

better than the patch antenna, but this difference is not very significant when compared to the SNR achieved by conventional MRI. This reduced SNR for travelling wave MRI can be attributed to the fact that the antennas, which are both transmitting and receiving, are much farther away from the imaging volume compared to conventional coils. This significantly reduces the B_1 that they are able to generate in the imaging volume, as well as attenuating the strength of the signal received. These two factors combine to reduce the SNR by a factor of about ten.

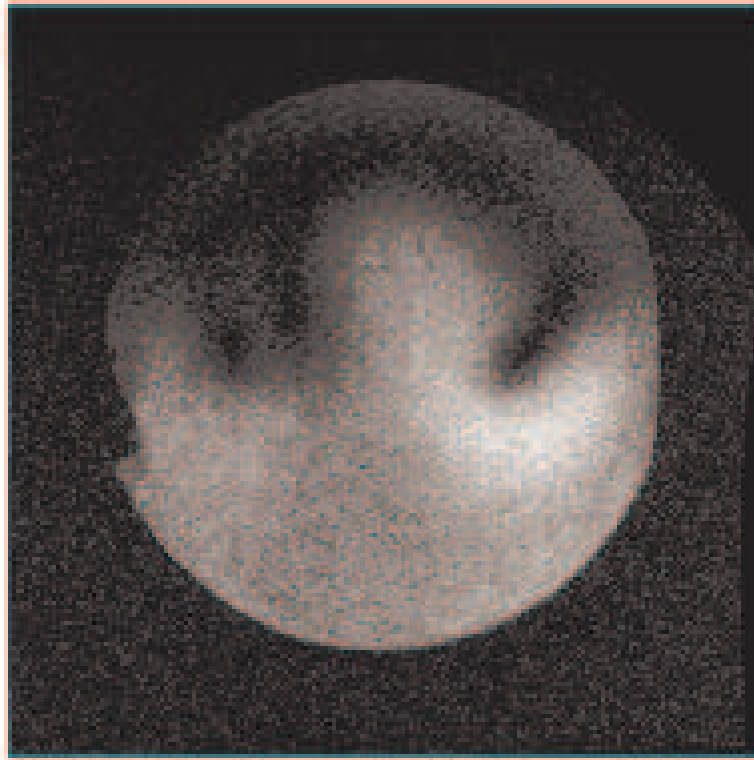


Figure 6.7: A sagittal image of a 20 cm spherical phantom taken using an end-fire helix antenna as both transmitter and receiver.

SNR	Patch	Helix	Volume
Transverse	100	187.5	1254
Sagittal	237.5	312.5	2444
Coronal	206.25	225	1849

Table 6.3: The power-normalised SNR values for the patch and end-fire helix antennas.

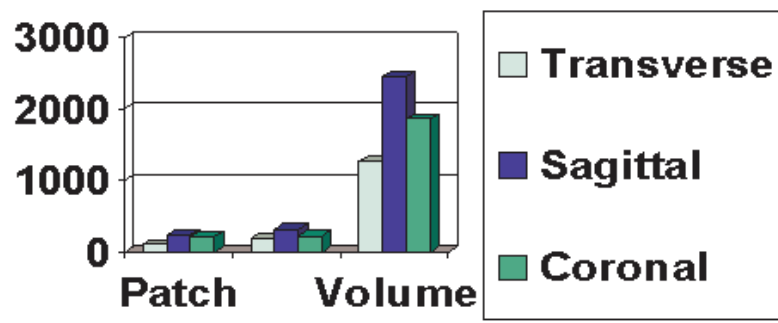


Figure 6.8: The power-normalised SNR for the patch antenna, end-fire helix antenna, and a conventional head volume coil.

6.4 Heating Test

In order to ascertain the energy deposition rates of the travelling wave method compared to conventional imaging a simple heating test was performed using the patch antenna. A one liter phantom was modified to hold a heat sensor probe (Photon Control PalmSENSE Temperature Sensor) in its centre. This phantom was then filled with one liter of water and placed in the scanner room overnight so that it would cool down to room temperature. The next day the phantom was imaged using a FFE sequence with the following scan parameters: flip angle of 90° , 1 mm isotropic resolution, TR of 250 ms, minimum TE. Attempting to change any of these scanner settings in a way that would increase the power, such as by reducing TR or increasing the flip angle, causes the scan to abort.

The scan took 47 minutes and 36 seconds to run. In that time the phantom temperature rose from 15.9°C to 16.2°C (the room temperature was still 15.9°C by the end of the scan). Using equation 2.48, this corresponds to an average heat deposition within the phantom of 0.44 W/kg , which provides an estimate of the SAR values that could be obtained from the patch antenna. Although the temperature rise was reduced by the air conditioning present in the bore room, such cooling would also be present if a subject were to be scanned. The most restrictive SAR limit in place on the seven tesla Achieva system is 3.2 W/kg for the head and therefore from this experiment it can be concluded that the patch SAR should be well below that level.

6.5 Patch Antenna Calibration

The various power calibration parameters used by the scanner for the patch antenna are shown in table 6.4.

The 'Max. Avg. Power' is based on the maximum power that the N-type sockets can handle. It is assumed that these are the weakest link in this particular coil, given that the patch has no electrical components and is essentially a 30 cm wide capacitor.

The 'Maximum B1 Available' is deliberately set low to limit the power used by the coil. This was necessary to compensate for the relatively large 'Ref. Scale'.

'Ref. B1' was an estimate based upon other coil files.

An initial estimate for 'Ref. Scale' was obtained by taking a series of images with different flip angles, finding the image with the highest SNR, and then scaling 'Ref. Scale' accordingly so that the image with the highest SNR would be the 90° image. This was further refined by taking a series of spectra with different flip angles and looking for the spectra that produced the strongest signal. Eventually spectra that were only 4° apart were used. Spectra that were only 1° apart all had a similar amplitude and could not be used for calibration.

As the maximum signal occurred at $90^\circ \pm 4^\circ$, the error in the coils power calibration is just under 4.5%. However it should be noted that this is only true for the 3 cm by 3 cm volume that was used in the calibration. The actual flip angle achieved will differ considerably from the requested flip angle as the region imaged moves away from this calibration location. This is the case for all RF transmit coils.

Parameter	Value
Max. Avg. Power	400 W
Maximum B1 Available	1 μ T
Ref. B1	10.8 μ T
Ref. Scale	3.94

Table 6.4: The power calibration values used by the patch antenna.

6.6 Imaging

In vivo images were obtained using the patch antenna as a transmitter and a local receive coil for signal detection. A FFE sequence was used, with a TR of 100 ms, TE of 1.73 ms, and 1.02 by 1.02 by 6 mm resolution. These images are presented in Figure 6.9. SNR values were calculated taking the noise measurements from just outside of the calf or ankle. The noise on the outside of the images is an artifact resulting from using the SENSE interface box with only a single element coil, and has thus been discounted. The SNR values of these images are approximately two to three times worse than SNR values obtained from a conventional head coil (which are typically around 100). Some of this SNR loss will be due to the nature of travelling wave MRI, but part of it is also due to both the small size of the receive coil and the relatively small volume of anatomy being imaged. The receive coil was a simple loop approximately 5 cm in size, giving it a similarly sized FOV. It is evident in most of the images in Figure 6.9 that image quality drops considerably outside of the receiver's FOV. Comparing the SNR values of the calf and ankle images it can be seen that the ankle had noticeably worse SNR (approximately a factor of two worse). If we assume that this drop in SNR is proportional to the drop in the volume of anatomy being imaged then this also helps to account for the drop in SNR of these images compared to the conventional volume coil; the SNR values from the volume coil were acquired imaging a phantom which had a volume significantly bigger than the calf imaged.

The images themselves, in the region covered by the receive coil,

are good quality. Basic muscle structure is visible in the calf and the bones in the heel are visible in the ankle images. Only two regions of B_1 inhomogeneity are evident (circled in red).

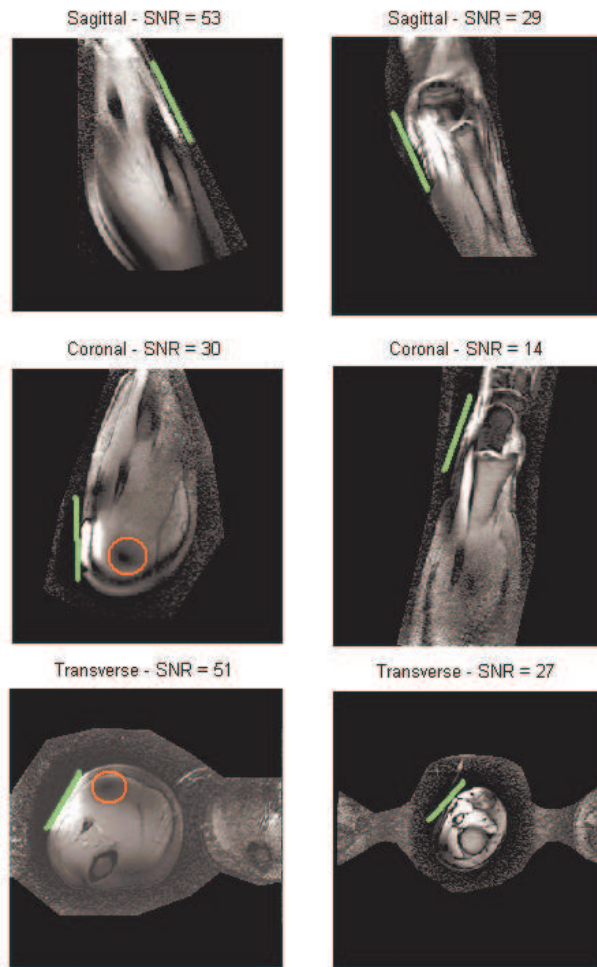


Figure 6.9: Images taken with the patch antenna transmitting and a local receive coil. Images on the left are of a calf and images on the right are of an ankle. The green lines mark the approximate size and location of the receive coil. The red circles highlight potential B_1 inhomogeneities. FFE sequence, TR of 100 ms, TE of 1.73 ms, 1.02 by 1.02 by 6 mm resolution. Note that all of these images have been masked to remove a reconstruction artifact. In the transverse ankle image there is a ghost artifact on the left, while the subject's other ankle is visible on the right.

Chapter 7

Conclusions

The design for the dome coil has been successfully constructed and tested. The dome coil achieves its goal of producing lower SAR in the shoulders, and is also capable of fitting within the dome shaped gradients. The SAR of the dome coil is lower than the SAR produced by a comparable birdcage coil. B_1 maps have been produced and from these it has been shown that it is possible to tune and match each element while decoupling them from their neighbours. Finally, the dome coil has been used to image a pineapple and a squash and has produced images with SNR values comparable to a conventional coil.

A number of problems arose while testing the dome coil which could have been avoided by doing some things differently. To aid tuning and matching it is desirable to ensure all variable capacitors can be accessed and adjusted while the coil is both loaded and in the magnet, which typically means having them aligned along the z-axis of the bore with their adjustable parts outside the coil.

To reduce the coupling between coaxial feed lines and the elements

it is better to have the coaxial cables on the outside of the RF screen as much as possible, only passing through the screen directly above where the elements need to be fed. Attempting to adjust the matching of the elements by moving the feed points is also impractical, as moving the coaxial cables introduces stray inductances and capacitances, as well as requiring new holes to be drilled in the coil if the adjustments are large. See Figure 7.1 for an illustration of this design.

Travelling wave MRI has been used *in vivo*. It does appear to be possible to obtain reasonable quality images if the patch antenna is used to transmit and a local receive coil is used to detect the signal. The main problems with implementing travelling wave MRI at the moment are the small size of the receive coil, the high power which therefore requires long TR times, and the minimum distance of 50 cm between the subject and the patch antenna that is required by the SAR levels. A new receive coil could provide a larger FOV and thus allow the advantages of travelling wave MRI (specifically its mitigation of B_1 inhomogeneities) to be tested. High power is likely to remain an issue and will therefore probably limit the travelling wave approach to where long TR's are either not a problem or the power levels are drastically reduced, such as in short imaging sequences and spectroscopy. The minimum safe distance of 50 cm is currently a problem as the patch antenna has to be mounted on the end of the scanner bed. This then imposes limitations on what regions of the subjects body can be in the scanner gradients and still be 50 cm from the patch antenna. Currently only imaging of the feet and lower calf is practical. This problem can be easily overcome

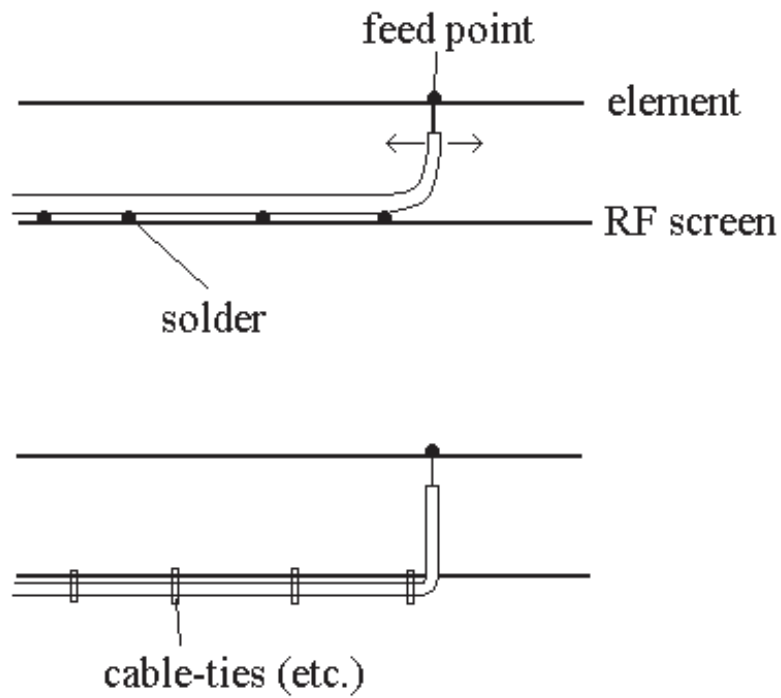


Figure 7.1: Top: the coaxial cables in the dome coil were tac-soldered onto the RF screen and then bent up to reach the feed point. Bottom: a sturdier and more electrically stable design would be to keep the cable outside the RF screen, and then pass it through a hole directly beneath the feed point.

by using longer cables to attach the patch antenna to the scanner: the patch antenna could then be mounted at the very end of the bore or even outside the bore if an extension of the bore's waveguide was available. This is demonstrated in Figure 7.2.

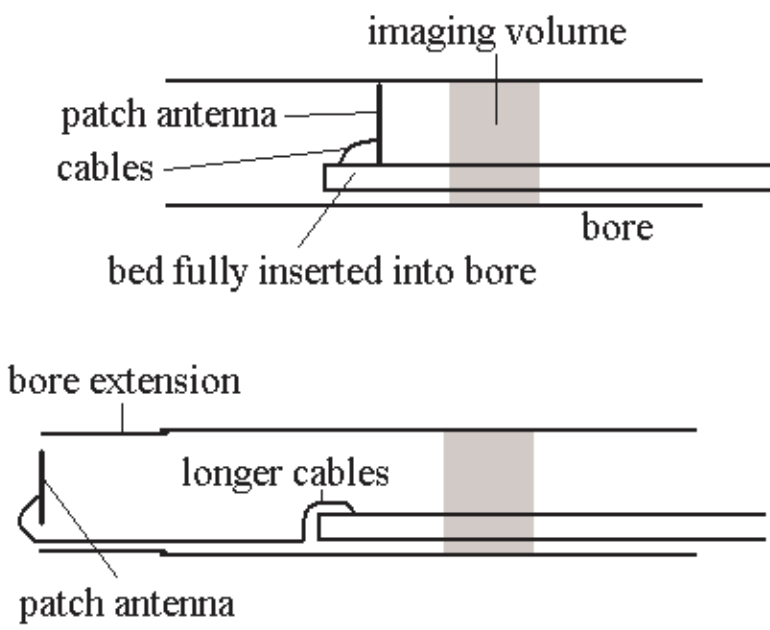


Figure 7.2: Top: the distance between the imaging volume and the patch antenna is very limited due to the short cables and limited bed motion. Bottom: a bore extension and longer cables drastically increase the available space between the patch antenna and imaging volume, making it easier to access different regions of the subjects anatomy.

7.1 Future Work

The geometry of the dome coil has been proven to reduce SAR but still be viable for imaging, so more dome shaped coils should be investigated. A birdcage-style dome coil would be usable on any seven T MRI system. The elements could be made shorter by removing the five to ten centimeters nearest the apex of the dome. This would help to reduce coupling between the elements as well as approximating a normal birdcage design better. The loss of B_1 at the very top of the head would probably not be a problem, based upon the simulations of the dome coil already performed. An initial concept diagram for this coil is shown in Figure 7.3.

The dome coil could also be adapted for only four-element multi-transmit by removing every other element as shown in Figure 7.4. This would help to reduce coupling between the elements and would also allow the coil to be used on a dual-transmit system with each channel being used in quadrature.

Constructing a larger receive array coil, such as the one shown in Figure 7.5, will allow travelling wave MRI to be investigated more thoroughly. It could also make it possible to image new regions of the body using the seven T Achieva system, such as the spine or abdomen. Adapting the patch antenna so that it can be mounted at the very end of the bore is a relatively straight-forward task and would make scanning with the travelling wave approach much easier.

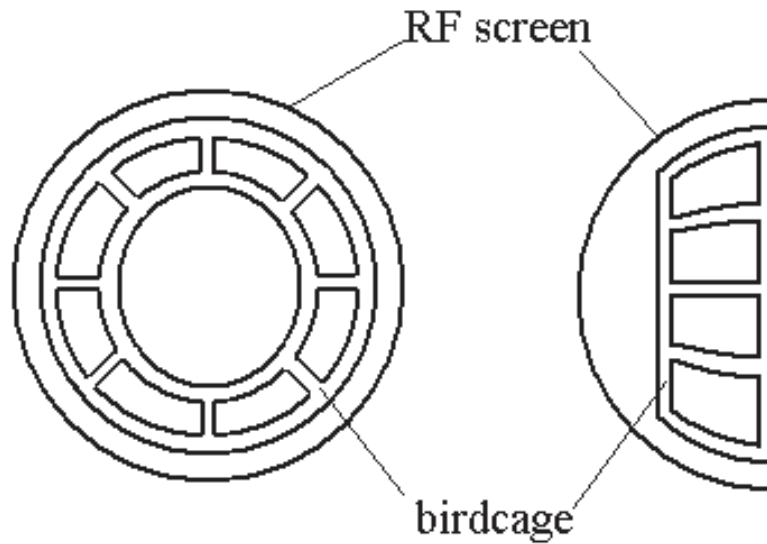


Figure 7.3: Initial concept for a dome birdcage coil. The RF screen is the same as for the dome coil, but the eight elements are shorter and are connected to a ring at both the top and bottom of each element.

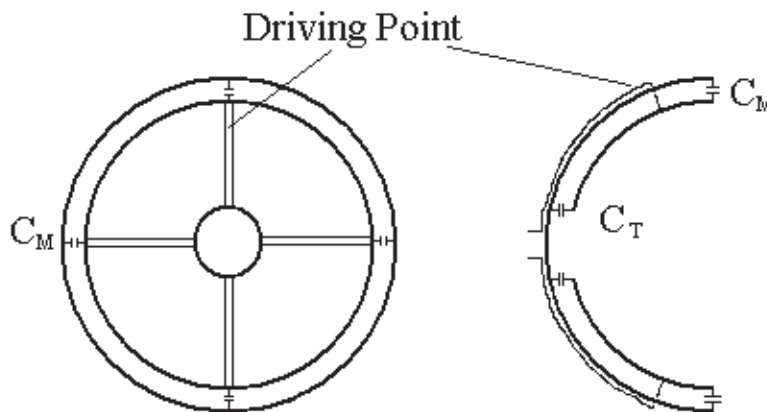


Figure 7.4: Initial concept for a four element dome coil. This design is identical to the eight element dome coil but with every other element removed.

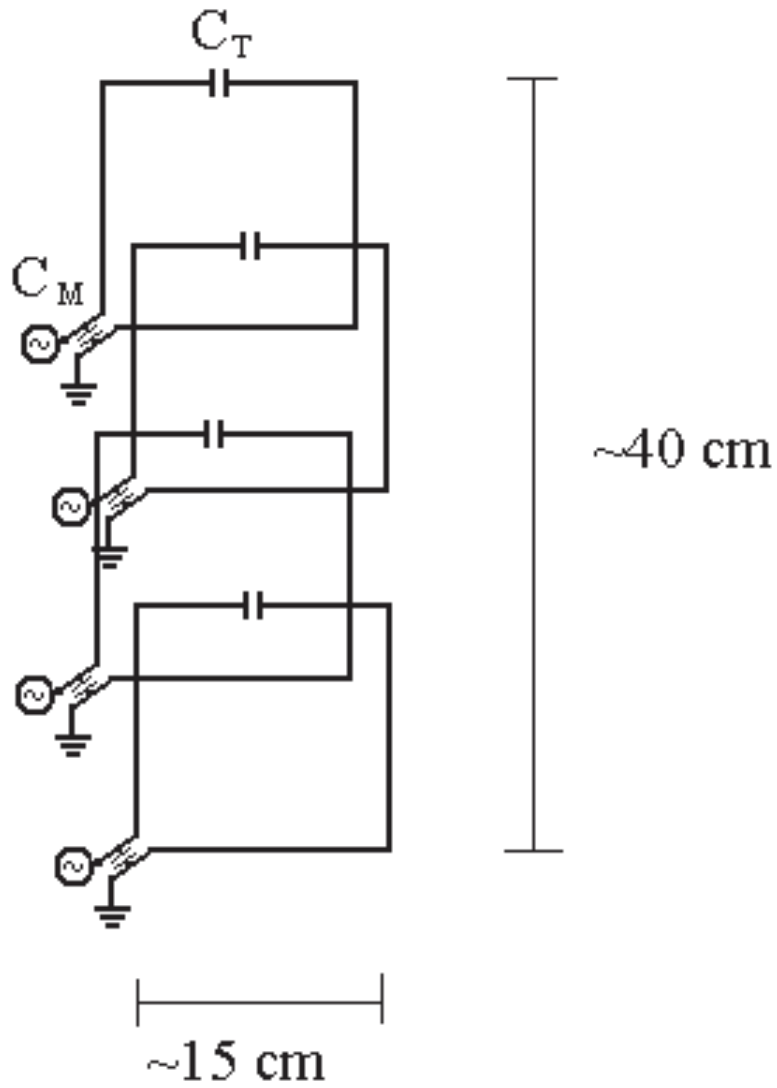


Figure 7.5: Initial concept for a four element spine coil. The four elements would be decoupled through pin-diode decoupling and using low-impedance preamplifiers. Note that in the diagram the elements are offset from each other to make the diagram clearer: in the actual coil all four elements would line up.

Appendix A

MATLAB Code

The following is a copy of the MATLAB program used to generate the R pulse sequences for multiple transmit imaging discussed in chapter 5.

```
% Daniel Lee 15/10/2008
    % A program to generate a pulse for a 2D excitation pattern using
    R coils.

% Input Data
    M0 = 1; % Equilibrium magnetisation
    gamma = 1; % Gyromagnetic ratio
    T = 2e-3; % Pulse duration
    N = 256; % Number of data points
    n = 8; % Cycles of spiral
    a = 50; % Scaling for k-space trajectory
    alpha = 1; % Scaling for the tip angle
    beta = 2; % Determines the spatial resolution of the selective volume
```

```

R = 8; % The number of coils

% Calculate Basics
t = linspace(0,T,N);
x = linspace(-N/2,N/2,N);
y = linspace(-N/2,N/2,N);
{X Y} = meshgrid(x,y);

% Specify the desired excitation pattern, gradients, and sensitivity profiles
Pdes = double(imread('logo.bmp'));
FOX = ones(floor(N/1.5),floor(N/1.5));
Sfull = zeros(N*R,N); % Sensitivity profiles
sens = zeros(N,N);

for r = 1:R
u = double(imread(sprintf('sensitivity profile %1.0f real.bmp',r)));
Sfull(((r-1)*N)+1:r*N,:) = u(:,:,1)/(max(max(u(:,:,1))));
sens = sens + u(:,:,1)/(max(max(u(:,:,1))));
end

Gz = zeros(1,N);
Gx = spiralex(t,a,gamma,T,n);
Gy = spiraly(t,a,gamma,T,n);
Gz = Gz * max(Gy); % Scale Gz to be comparable to Gx and Gy

```

```

G = sqrt(Gx.2 + Gy.2 + Gz.2);

% Reduce Pdes and Sfull to the FOX
{FOXx FOXy} = size(FOX);
firstpointx = floor((N - FOXx)/2+1);
firstpointy = floor((N - FOXy)/2+1);
lastpointx = floor((N - FOXx)/2 + FOXx);
lastpointy = floor((N - FOXy)/2 + FOXy);
sens = sens(firstpointx:lastpointx,firstpointy:lastpointy);
Pdes = Pdes(firstpointx:lastpointx,firstpointy:lastpointy);
temp2 = zeros(FOXx*R,FOXy);

for r = 1:R
temp = Sfull(((r-1)*N)+1:r*N,:);
temp2(((r-1)*FOXy)+1:r*FOXy,:) =
temp(firstpointx:lastpointx,firstpointy:lastpointy);
end

Sfull = temp2;
{XFOX YFOX} = meshgrid(x(firstpointx:lastpointx),
y(firstpointy:lastpointy));

% Calculate k, pdes, and B1
kx = zeros(1,N);
area = zeros(1,N);

```

```
for tau = 1:N
area(tau) = integrate(Gx,t,tau,N);
kx(tau) = - gamma * area(tau);
end
```

```
ky = zeros(1,N);
area = zeros(1,N);
```

```
for tau = 1:N
area(tau) = integrate(Gy,t,tau,N);
ky(tau) = - gamma * area(tau);
end
```

```
pdes = fftshift(fft2(Pdes,N,N));
pdes = diag(pdes);
sfull = fftshift(fft2(Sfull,N*R,N));
% sfullv = zeros(N,N);
Gv = zeros(1,N/R);
pdesv = zeros(1,N/R);
sv = zeros(N,N/R,R);
```

```
for r = 1:R
```

```
for v = 1:N/R
```

```

w = v + (r-1)*N/R;
for n = 1:N
sv(n, v, r) = sfull(n,w);
end
Gv(1,v) = G(1,w);
pdesv(1,v) = pdes(w,1);
end

end

sfullv = reshape(sv,N,N);
Av = abs(Gv) ./ pdesv;
pw = lsqr(sfullv,pdes)';
% A = abs(G) ./ pdes';
p = zeros(R,N/R);
B1 = zeros(R,N/R);

for r = 1:R

for n = 1:N/R
p(r,n) = pw(1,(r-1)*N/R+n);
B1(r,n) = Av(n) .* M0 .* p(r,n);
end

end

```

```
B1out = reshape(B1',1,N);

% Save the data to file
fid = fopen('RF2DRElement.txt','w');
fprintf(fid, '%d \n', B1out);
```

Bibliography

- [1] P. Mansfield. Multi-planar image formation using NMR spin echoes. *J. Phys. C: Solid State Phys.*, 10:L55–58, 1977.
- [2] Katscher et al. Transmit SENSE. *Magnetic Resonance in Medicine*, 49:144–150, 2003.
- [3] David O. Brunner, Nicola De Zanche, Jurg Frohlich, Jan Paska, and Klaas P. Pruessmann. Travelling-wave nuclear magnetic resonance. *Nature*, 457:994–998, 2009.
- [4] G. M. Bydder and I. R. Young. MR Imaging: Clinical use of the inversion recovery sequence. *J. Comput. Assist. Tomogr.*, 9:659–675, 1985.
- [5] G. M. Bydder, R. E. Steiner, and L. H. Blumgart. MR Imaging of the liver using short TI inversion recovery. *J. Comput. Assist. Tomogr.*, 9:1084–1089, 1985.
- [6] T. K. F. Foo, A. M. Sawyer, W. H. Faulkner, and D. G. Mills. Inversion in the steady-state-contrast optimization and reduced imaging time with fast 3-dimensional inversion-recovery-prepared GRE pulse sequences. *Radiology*, 191:85–90, 1994.

- [7] J. V. Hajnal, B. De Coene, P. D. Lewis, C. J. Baudouin, F. M. Cowan, J. M. Pennock, I. R. Young, and G. M. Bydder. High signal regions in normal white matter shown by heavily T2-weighted CSF nulled IR sequences. *J. Comput. Assist. Tomogr.*, 16:506–513, 1992.
- [8] J. V. Hajnal, D. J. Brynat, L. Kasuboski, P. M. Pattany, B. De Coene, P. D. Lewis, J. M. Pennock, A. Outridge, I. R. Young, and G. M. Bydder. Use of fluid attenuated inversion recovery (FLAIR) pulse sequences in MRI of the brain. *J. Comput. Assist. Tomogr.*, 16:841–844, 1992.
- [9] J. H. Mugler III and J. R. Brookeman. Three-dimensional magnetization-prepared rapid gradient-echo imaging (3D MP-RAGE). *Magn. Reson. Med.*, 15:152–157, 1990.
- [10] V. M. Runge, M. L. Wood, D. M. Kaufman, and M. S. Silver. MR imaging section profile optimization: Improved contrast and detection of lesions. *Radiology*, 167:831–834, 1988.
- [11] J.R. MacFall, H. C. Charles, and R. Prost. Truncated SINC slice excitation for ^{31}P spectroscopic imaging. *Magn. Reson. Imaging*, 8:619–624, 1990.
- [12] M. H. Levitt. Composite pulses. *Prog. NMR Spectrosc*, 18:61–122, 1986.
- [13] K. Ugurbil, M. Garwood, A. R. Rath, and M. R. Bendall. Amplitude- and frequency/phase-modulated refocusing pulses that

- induce plane rotations even in the presence of inhomogeneous B1-fields. *J. Magn. Reson.*, 78:472–496, 1988.
- [14] S. Conolly, D. Nishimura, A. Macovski, and G. Glover. Variable-rate selective excitation. *J. Magn. Reson.*, 78:440–458, 1988.
- [15] S. Conolly, G. Glover, D. Nishimura, and A. Macovski. A reduced power elective adiabatic spin echo pulse sequence. *Magn. Res. Med.*, 18:28–38, 1991.
- [16] E. L. Hahn. Spin echoes. *Phys. Rev.*, 80:580–594, 1950.
- [17] J. Hennig, A. Nauerth, and H. Friedburg. RARE imaging: A fast imaging method for clinical MR. *Magn. Reson. Med.*, 3:823–833, 1986.
- [18] J. Hennig. Multiecho sequences with low refocusing flip angles. *J. Magn. Reson.*, 78:397–407, 1988.
- [19] B. A. Hargreaves, G. E. Gold, P. K. Long, S. M. Conolly, J. M. Pauly, G. Bergman, J. Vandevenne, and D. G. Nishimura. MR imaging of articular cartilage using driven equilibrium. *Magn. Reson. Med.*, 42:695–703, 1999.
- [20] R. L. Ehman and J. P. Felmlee. Adaptive technique for high-definition MR imaging of moving structures. *Magn. Reson. Imaging*, 173:255–263, 1989.
- [21] J. Frahm, A. Haase, and D. Matthaei. Rapid NMR imaging of dynamic processes using the FLASH technique. *Magn. Reson. Med.*, 3:321–327, 1986.

- [22] H. W. Park, M. H. Cho, and Z. H. Cho. Real-value representation in inversion-recovery NMR imaging by use of a phase-correction method. *Magn. Reson. Med.*, 3:15–23, 1986.
- [23] Q. S. Xiang. Inversion recovery image reconstruction with multi-seed region-growing spin reversal. *J. Magn. Reson. Imaging*, 6:775–782, 1996.
- [24] R. K. Breger, A. A. Rimm, M. E. Fischer, R. A. Papke, and V. M. Haughton. T1 and T2 measurements on a 1.5-T commercial MR imager. *Radiology*, 171:273–276, 1989.
- [25] F. Eggenschwiler, A. Magill, and R. Greutter and J. P. Marques. Sa2RAGE - A new sequence for rapid 3D B1+-mapping with a wide sensitivity range. *Proc. Intl. Soc. Mag. Reson. Med* 18, 2010.
- [26] Matt A. Bernstein, Kevin F. King, and Xiaohong J. Zhou. *Handbook of MRI Pulse Sequences*. Elsevier Academic Press, 2004.
- [27] J B Ra and C Y Rim. Fast imaging method using multiple receiver coils with subencoding data set. *Proceedings of the ISMRM 6th annual meeting, San Francisco, pages = 1240, year = 1991*.
- [28] International Standard IEC 60601-2-33.
- [29] Klaas P. Pruessmann, Markus Weiger, Markus B. Scheidegger, and Peter Boesiger. SENSE: Sensitivity Encoding for Fast MRI. *Magnetic Resonance in Medicine*, 42:952–962, 1999.
- [30] Philip M. Robson, Aaron K. Grant, Ananth J. Madhurnathakam, Riccardo Lattanzi, Daniel K. Sodickson, and Charles A. McKen-

- zie. Comprehensive Quantification of Signal-to-Noise Ratio and g-Factor for Image-Based and k-Space-Based Parallel Imaging Reconstructions. *Magnetic Resonance in Medicine*, 60:895–907, 2008.
- [31] Ulrich Katscher and Peter Bornert. Parallel Magnetic Resonance Imaging. *Neurotherapeutics: The Journal of the American Society for Experimental NeuroTherapeutics*, 4:499–510, 2007.
- [32] Riccardo Lattanzi, Daniel K. Sodickson, Aaron K. Grant, and Yudong Zhu. Electrodynamics Constraints on Homogeneity and Radiofrequency Power Deposition in Multiple Coil Excitations. *Magnetic Resonance in Medicine*, 61:315–334, 2009.
- [33] Robert G. Pinkerton, Graeme C. McKinnon, and Ravi S. Menon. SENSE Optimization of a Transceive Surface Coil Array for MRI at 4T. *Magnetic Resonance in Medicine*, 56:630–636, 2006.
- [34] S. M. Rao and N. Balakrishnan. Computational electromagnetics - A review. *Current Science*, 77:1343, 1999.
- [35] S Yee. Numerical solution of initial boundary value problems involving Maxwell’s equations in isotropic media. *IEEE Trans Antennas Propagat*, 14:302–307, 1966.
- [36] Christos Christopoulos. *The Transmission-Line Modeling Method TLM*. IEEE Press and Oxford University Press, 1995.
- [37] Reinhold Ludwig and Gene Bogdanov. *RF Circuit Design: Theory and Applications*. Pearson Prentice Hall, 2nd edition, 2009.

- [38] Ray F. Lee, Randy O. Giaquinto, and Christopher J. Hardy. Coupling and Decoupling Theory and Its Application to the MRI Phased Array. *Magnetic Resonance in Medicine*, 48:203–213, 2002.
- [39] Andrew J. Parfitt, Donald W. Griffin, and Peter H. Cole. Mutual Coupling Between Metal Strip Antennas on Finite, Electrically Thick Dielectric Substrates. *IEEE Transactions on Antennas and Propagation*, 41(1), 1993.
- [40] P.B. Roemer, W.A. Edelstein, C.E. Hayes, S.P. Souza, and O.M. Mueller. The NMR Phased Array. *Magnetic Resonance in Medicine*, 16:192–225, 1990.
- [41] C. E. Hayes, W. A. Edelstein, J. F. Schenck, O. M. Mueller, and M. Eash. An efficient, highly homogeneous radiofrequency coil for whole-body nmr imaging at 1.5 T. *J. Magn. Reson.*, 63:622628, 1985.
- [42] T. S. Ibrahim, R. Lee, B. A. Baertlein, A. M. Abduljalil, H. Zhu, and P. M. Robitaille. Effect of RF coil excitation on field inhomogeneity at ultra high fields: a field optimized TEM resonator. *Magnetic Resonance Imaging*, 19:1339–1347, 2001.
- [43] W. Mao, M. B. Smith, and C. M. Collins. Exploring the limits of RF shimming for high field MRI of the human head. *Magnetic Resonance in Medicine*, 56:918–922, 2006.
- [44] T. Vaughan, L. DelaBarre, C. Snyder adn J. Tian, C. Akgun, D. Shrivastava, W. Liu, C. Olson, G. Adriany, J. Strupp, P. An-

- derson, A. Gopinath, P. F. van de Moortele, M. Garwood, and K. Ugurbil. 9.4T human MRI: preliminary results. *Magnetic Resonance in Medicine*, 56:1274–1282, 2006.
- [45] Lin et al. Degenerate Mode Birdcage Volume Coil for Sensitivity-Encoded Imaging. *Magnetic Resonance in Medicine*, 50:1107–1111, 2003.
- [46] Katscher et al. Theoretical and Numerical Aspects of Transmit SENSE. *IEEE Transactions on Medical Imaging*, 23(4):520–525, 2004.
- [47] Adriany et al. Transmit and Recieve Transmission Line Arrays for 7 Tesla Parallel Imaging. *Magnetic Resonance in Medicine*, 53:434–445, 2005.
- [48] Ulrich Katscher and Peter Bornert. Parallel RF Transmission in MRI. *NMR in Biomedicine*, 19:393–400, 2006.
- [49] Alagappan et al. Degenerate Mode Band-Pass Birdcage Coil for Accelerated Parallel Excitation. *Magnetic Resonance in Medicine*, 57:1148–1158, 2007.
- [50] Vernickel et al. Eight-Channel Transmit/Receive Body MRI Coil at 3T. *Magnetic Resonance in Medicine*, 58:381–389, 2007.
- [51] Seifert et al. Patient Safety Concept for Multichannel Transmit Coils. *Journal of Magnetic Resonance Imaging*, 26:1315–1321, 2007.

- [52] Jovan Jevtic. Ladder Networks for Capacitive Decoupling in Phased-Array Coils. In *Proc. Intl. Soc. Mag. Reson. Med 9*, 2001.
- [53] Andrew G. Webb, Christopher M. Collins, Maarten J. Versluis, Hermien E. Kan, and Nadine B. Smith. MRI and localized Proton Spectroscopy in Human Leg Muscle at 7 Tesla Using Longitudinal Traveling Waves. *Magnetic Resonance in Imaging*, 63:297–302, 2010.
- [54] J. Wang. In *Proceedings ISMRM*, 1996.